Catalytic Partial Oxidation in Novel Non-Premixed Counter-Flow Reactor Configurations

A Dissertation
SUBMITTED TO THE FACULTY OF
UNIVERSITY OF MINNESOTA
BY

Ying Lin

IN PARTIAL FULFILLMENT OF THE REQUIREMENTS
FOR THE DEGREE OF
DOCTOR OF PHILOSOPHY

Advisor: William F. Northrop

September. 2020

© Copyright by Ying Lin, 2020

Acknowledgements

This work was only made possible under the help of my advisor, collaborators, colleagues, friends and family members.

I am very grateful for the privilege of joining Murphy Engine Research Laboratory and being advised by Dr. Will Northrop. The education and training I received has defined who I am for my life and career. Dr. Northrop taught me the most important skills and knowledge for being an independent researcher, and his vision and attitude towards work and life will always inspire me. I want to thank him for his patience, trust, persistence and guidance during these years.

Thanks to my collaborators for their generous contribution to this work. Dr. Xuesong Li and Dr. David Kittelson provided insightful directions to my research. Dr. Xuesong Li was also deeply involved in my projects and provided important data. The numerical modeling work was conducted under tremendous help of Dr. Robert Kee, Dr. Gandhali Kogekar and Dr. Canan Karakay.

My doctoral training would not be made possible without the funding resources. Sincere thanks to the Minnesota Corn Growers Association and the National Science Foundation.

I would also like to acknowledge current and former members of our lab. They are all intelligent and supporting people who inspired me a lot by their work and ideas.

To my parents and my wife Yiru Wang, your contained, unconditional love supported me going through the uncertainty and anxiety of these years. You believe in me, celebrate the smallest progress I make, and never stop shaping me into a better person

Abstract

Catalytic partial oxidation (CPOx) is established processes for generating synthesis gas (i.e. the mixtures of hydrogen and carbon oxides). It is used to convert heavier hydrocarbon fuels into lighter ones or synthesis gas for a variety of applications. CPOx systems usually incorporate metal catalysts, such as nickel, platinum, rhodium, etc., impregnated on wash-coated porous media to enhance surface reaction rates. The rapid reforming kinetics and expedient light-off characteristics of CPOx make it suitable not only for large-scale industrial applications, but also for on-board vehicle reforming and other portable applications where compactness and simplicity are advantageous.

There are different CPOx schemes for desired reforming reactions, including plug-flow reactors, wire gauge reactors, and flash volatilization techniques. Most CPOx reactors reported in the literature implement premixed schemes that mix fuel, oxidizer (usually oxygen), and other species (such as steam) prior reaching the catalyst inlet. Such implementations enjoy benefits of simple structures and flow patterns. However, disadvantages of premixed reformers are also exist including autoignition caused by preheating the mixture before reactions and catalyst deactivation through surface carbon formation and coking.

To overcome the disadvantages of premixed CPOx, novel, non-premixed reactor type has been conceived and studied in this body of work. The reactor design is inspired by the canonical counter-flow burner commonly used in flame studies but has a catalyst-coated metal mesh

located between the air and fuel inlets. The counter-flow CPOx reactor has unique temperature gradients and residence times that tend to reduce coking by avoiding thermal and mixture conditions where carbon is formed. This counter-flow configuration has the potential in both fundamental studies like investigating reforming kinetics and practical applications like enabling advanced combustion modes in internal combustion engines.

Table of Contents

Acknowledgements i

Abstract ii

List of Tables vi

List of Figures vii

Chapter 1 Introduction 10

1.1 Motivation 10

1.2 Project Objective Statement 12

1.3 Significance of Work 13

Chapter 2 Background 15

2.1 Catalytic partial oxidation and fuel reforming 15

2.2 Small Scale Reactors 20

2.3 Catalytic Deactivation and Soot Formation 25

2.4 Ethanol Autothermal Reaction and Reaction Pathway 26

2.5 Advanced Laser-based Diagnostics 30

2.6 Applications of Fuel Reforming 34

Chapter 3 Experimental Apparatus 39

3.1 Reactor Setup 39

3.2 Emission Measurement Equipment 43

3.3 Laser Diagnostic System 44

Chapter 4 Characterization of Hydrocarbon CPOx Using Gas Phase Counter-flow Reactor 46

4.1 Experimental Procedure 47

4.2 Results and Discussion 50

4.3 Conclusions 63

Chapter 5 Application of Dual Mesh Counter-flow Reactor 65

5.1 Experimental Procedure 66

5.2 Result and Discussion 68

5.3 Conclusion 74

Chapter 6 Planar Laser-induced Fluorescence (PLIF) for Noncontact Temperature Measurement 75

6.1 Experimental Procedure 76

6.2 Image Processing 78

6.3 Results and Discussion 82

6.4 Conclusion 89

Chapter 7 Hydrocarbon CPO_X with Atomization Reactor 91

7.1 Experimental Procedure 92

7.2 Results and Discussion 96

7.3 Conclusions 114

Chapter 8 Suggested Future Work 116

Bibliography 120

List of Tables

Table 2.1 Summary of pros/cons and industrial developer of popular methane reforming technologies 36

Table 4.1 Experimental conditions to study mesh location effect 54

Table 5.1 Dual mesh configuration ignition study conditions 73

Table 6.1 Filter and Camera Specifications 77

Table 6.2 Experimental Conditions for PLIF Thermometer in the Counter-flow Reactor 86

Table 7.1 Liquid fuel reactor characterization conditions 95

List of Figures

Figure 1.1 Reformer efficiency ($\eta_{reformer}$) versus the ϕ of partial oxidation of n-heptane when exhaust gas recirculation (EGR) from an engine operating at ϕ=0.5 11

Figure 2.1 Spatially resolved species and temperature profiles for syngas stoichiometry (C/O = 1.0) and a total inlet flow of 4.7 slpm 18

Figure 2.2 Schematic of the counter-flow reactive volatilization model 22

Figure 2.3 Counter flow diffusion fames into two types.. 23

Figure 2.4 Carbon region and carbon free region for different ethanol related fuel 27

Figure 2.5 Ethanol catalytic reaction pathway 29

Figure 2.6 Schematic of the molecular energy structure displaying energy states with different vibrational and rotational quantum numbers within two electronic potentials. . 31

Figure 2.7 (a) Toluene fluorescence spectra as a function of temperature at 266 nm excitation. Data courtesy of Koban et al. (b) expected signal ratios as a function of temperature for dual-band thermometry, for a BP280 filter paired with a WG305 (cyan), WG320 (blue), and WG335 (red) filter 33

Figure 2.8 An example of catalytic partial oxidation fuel reforming in engine application using exhaust waste heat recovery to preheat reactants 37

Figure 3.1 Gas phase counter-flow reactor for single mesh configuration 40

Figure 3.2 Gas phase counter-flow reactor for dual mesh configuration..... 41

Figure 3.3 Counter-flow atomizer reactor design 43

Figure 3.4 Nd:YAG laser scheme 45

Figure 4.1 Typical stabilized reaction surface found during the gas experiments. 49

Figure 4.2 Possible reaction models of the gaseous counter flow reactor depending on the resistance of the mesh 51

Figure 4.3 Different flow pattern/reaction model apply to different regions of the reactor

..... 53
Figure 4.4 Syngas production under different equivalence ratios 56
Figure 4.5 Experimental setup of Rh catalytic mesh reaction efficiency characterization 58
Figure 4.6 Non-reacting speciation distribution in the reactor. Fuel inlet is at 0 mm axial location; oxidizer inlet is at 14 mm axial location. 59
Figure 4.7 Speciation (left) and temperature (right) measurement of the reactor characterization study. 60
Figure 4.8 Axial flow velocity simulation with similarity model 60
Figure 4.9 Equilibrium calculation of ethylene suggest less soot/coke formation in a counter-flow reactor than a plug flow reactor 63
Figure 5.1. Diagram of the dual catalytic mesh opposed-flow reactor 65
Figure 5.2. Illustration of where data was taken for dual-mesh experiments 68
Figure 5.3 Axial centerline temperature for dual mode and single platinum mode. 69
Figure 5.4. Dry mole fractions of reforming products as a function of axial distance at the centerline. 71
Figure 5.5. Mole fractions of reforming products as a function of radial distance. 72
Figure 5.6 Ignition delay (50% of total heat release) under decreasing fuel conditions .. 73
Figure 6.1 The flow condition (left) and surface reaction (right) are affected by an intrusive measurement/sampling method. 76
Figure 6.2 Experimetal setup diagram 78
Figure 6.3 Non-contact PLIF thermometer image processing scheme. 78
Figure 6.4 Calibration chess board picture placed at the reactor position. 79
Figure 6.5 Chess board picture calibration. 80
Figure 6.6 ICCD camera noise smoothing function. 81
Figure 6.7 Background subtracting step is taken before the division of the two images. 82
Figure 6.8 Constant temperature cell calibration setup. 83

Figure 6.9 Fluorescence signal ratio-temperature calibration curve 84
Figure 6.10 Signal-error ratio plot shows the percentage of measurement error in the signal ratio. 85
Figure 6.11 Temperature error propagation analysis of the PLIF temperature measurement system 86
Figure 6.12 2-D temperature contour plot of the counter-flow reactor by PLIF thermometer and thermocouple for the three conditions. 88
Figure 7.1 Schematic diagram for atomazation reactor 93
Figure 7.2 Conversion and reforming efficiency under different pressure 99
Figure 7.3 Reaction selectivity of ethanol reactor 100
Figure 7.4 Reaction temperature for different ethanol reltive fuel under vary C/O ratio 102
Figure 7.5 Fuel converson under different C/O ratios 104
Figure 7.6 Major product selectivity and product concentration for different C/O ratios 107
Figure 7.7 Methane and ethylene product concentraiton under different C/O ratio 108
Figure 7.8 Soot formation on catalyst 110
Figure 7.9 Predicted reaction model for non-premixed reactive volatilization reactor ... 112
Figure 7.10 Local C/O ratio at bottom of catalyst Vs. Global C/O ratio 113
Figure 7.11 Reforming efficiency for different C/O ratio 114

Chapter 1 Introduction

1.1 Motivation

Hydrocarbon reforming and partial oxidation (POx) are established processes for generating synthesis gas (mixtures of hydrogen and carbon oxides). They are applied to manufacturing of a wide range of valuable industrial products [1-3]. Moreover, exhaust gas waste heat driven liquid and gaseous fuels reforming has been proposed as a crucial process for producing hydrogen in fuel cells [4-9] and for enhancing internal combustion engines [10-14]. Hydrocarbon POx reformers are principally limited by stoichiometry. POx reactors must operate at a global equivalence ratio (ϕ_g), as defined by the fuel to oxidizer mass ratio divided by the stoichiometric fuel to oxidizer ratio ($\phi = (m_f/m_{ox})\cdot(m_f/m_{ox})_{stoich}^{-1}$), below 3.0 to avoid soot formation [3]. However, lower ϕ is in favor of more complete combustion, converting significant fuel heating value into unusable heat, thus reducing overall reforming efficiency.

To date, industrial large-scale catalytic partial oxidation (CPOx) reactors for chemical feedstock production have been well studied. [15] However, small-scale catalytic partial oxidation reactors designed for engine and fuel cell applications have been proven unreliable, costly, and inefficient. Inefficiencies result from considerable chemical energy losses when the fuel is consumed in the exothermic oxidation process when driven to maximize production of the

traditional reforming products H_2, CO and CH_4. Catalytic and non-catalytic POx reactors are both limited by stoichiometry, as previously mentioned, to avoid soot and coke formation leading to reactor fouling and catalyst deactivation. With increasing ϕ, reformer efficiency, defined by the ratio of the sum of product lower heating value to that of the reactants ($\eta_{reformer} = LHV_{products} \cdot LHV_{reactants}^{-1}$), increases as shown by the simple modeling analysis for n-heptane reforming illustrated in Fig. 1.1.

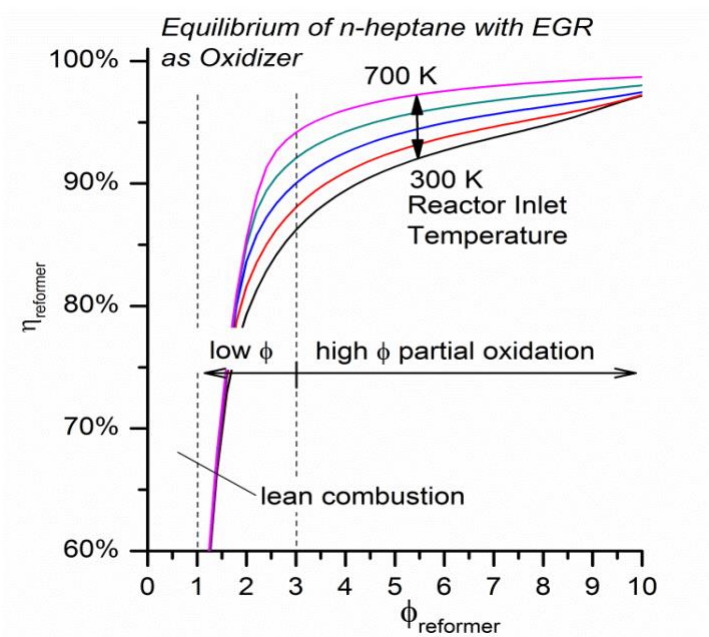

Figure 1.1 Reformer efficiency ($\eta_{reformer}$) versus the ϕ of partial oxidation of n-heptane when exhaust gas recirculation (EGR) from an engine operating at ϕ=0.5 is used as the oxidizer. A range of reactor inlet temperature is shown, and chemical equilibrium was assumed in the calculation at constant pressure and enthalpy. The plot shows that for minimal loss in fuel heating value, it is advantageous to operate with elevated inlet temperature and higher ϕ.

This study focuses on characterization of small-scale reactors that can be applied to on-board reforming in vehicles and that can be used in fundamental kinetic studies. The novel non-premixed

reactor can also help maintain the performance of the catalyst and provide a reactor that could maintain high activity, high selectivity, and high reformer efficiency.

Catalyst deactivation is an important factor that needs to be considered when implementing a new reactor design. Catalyst deactivation is complicated by the reactor size, design and operating conditions. Deactivation mechanisms can be placed into the following five categories: poisoning, fouling, thermal degradation (sintering, evaporation) initiated by high temperature, mechanical damage and corrosion/leaching by the reaction mixture [16]. For different catalyst types, there are a variety of causes of deactivation. One common reason is carbon formation under fuel-rich conditions and carbon deposition on the catalyst surface sites. Further, formation of the carbon fibers could cause the physical loss of the catalytic active metal particles on the surface [17-19]. The novel non-premixed counter-flow reactor studied in this research has unique thermal gradients and its short residence times tend to reduce soot, and therefore limit catalyst deactivation.

1.2 Project Objective Statement

This work explores a new method for studying non-premixed CPOx at high equivalence ratio and short contact time. Two different designs of counter-flow partial oxidation reactor experimentally examined: (1) *the gas phase counter-flow reactor* is inherited from the canonical counter-flow reactor commonly used in flame studies but with a catalyst-coated metal mesh located between the air inlet and fuel inlet. (2) *the counter-flow atomizer reactor with high throughput*

reforming has the gaseous fuel jet replaced by a fuel atomizer, to enhance vaporization and transport through the gas reaction zone to the catalytic mesh. With the reactors, the four objectives that have been achieved as follows:

***Objective 1*:** Characterize a gas phase counter-flow reactor for hydrocarbon partial oxidation with methane as the fuel.

***Objective 2*:** Characterize the dual-mesh configuration in the gas phase counter-flow reactor for hydrocarbon partial oxidation to explore the possibility of vehicle on-board application.

Objective 3: Develop a non-contact temperature measurement technique with PLIF system to apply in the gas phase counter-flow reactor

Objective 4: Characterize the modified liquid phase counter-flow reactor with ethanol-gasoline blends.

1.3 Significance of Work

This work proposed and evaluated a novel counter-flow reactor and derivative reactors. These reactors provide a stable platform to produce syngas from a variety of light hydrocarbons. The counter-flow configuration shows the potential to be used in both fundamental studies, such as reforming kinetics investigations; and practical applications such as enabling advanced combustion modes in internal combustion engines. For engine applications, a scaled-up version of the reactor could efficiently change the reactivity of the original fuel and enhance autoignition in engines.

The unique thermal gradient and short contact time in non-premixed counter-flow reactors significantly reduces coke formation, this preventing catalyst deactivation. In addition, findings that the reaction zone around the catalyst mesh is dominated surface reactions, show that the reactor type could be used for fundamental studies of chemical kinetics.

Moreover, laser diagnostics are introduced to this study as additional tools for studying catalytic reactions. The open configuration of the counter-flow reactor lends itself to in-situ diagnostics better than premixed plug-flow type reactors. Additionally, this work provides a deeper understanding of the utility of counter-flow configurations for studying catalytic reactions and provides recommendations for future studies to further advance the novel concept.

Chapter 2 Background

2.1 Catalytic partial oxidation and fuel reforming

Hydrocarbon reforming and partial oxidation are widely used in syngas generation, chemical preparation, and fuel cell systems [1-9]. The industrial steam reforming and autothermal reforming is the major source of hydrogen production. The large-scale steam reforming reactors provide a high throughput, high reliability and high purity platform to produce hydrogen. The scale up effect is significant in the capital cost. On the fuel cell side, solid oxide fuel cells (SOFCs) are the most conventional type. The advantages of SOFCs are flexibility, compatibility of impurified fuel and tolerance to non-noble metal catalysts. Fuel reforming is a required process to convert hydrocarbon fuels to hydrogen rich fuel to avoid carbon deposition on the anode.

Prior research has also investigated fuel processing for enabling advanced combustion modes and improving efficiency in engines. For example, very recent work by Szybist et al. [20, 21] has shown that a catalytic reactor enabled reformed exhaust gas recirculation, leading to enhanced dilution tolerance of a spark ignition gasoline engine and thereby increased thermal efficiency by 8%. The developed system fed exhaust from a single cylinder engine running at rich equivalence ratio into a catalytic reactor to demonstrate their concept. Previous work has also studied using recouped engine exhaust energy to reform higher molecular weight fuels like diesel to enable

efficient dual fuel combustion modes with one stored fuel [10, 11, 22]. For dual fuel engine operation, full conversion in reforming is not necessary; only partial fuel conversion is needed to sufficiently increase the reformed fuel's ignition delay.

Generally, major chemical processes are considered in fuel reforming—partial oxidation, steam reforming, and dry reforming as given in Equations 2.1-2.5, where CH_4 is used as example fuel. Equation 2.1 shows a stoichiometric combustion reaction. The reaction is highly exothermic, and its heat production is much higher than any reforming reaction. In partial oxidation (Eq. 2.2), the hydrocarbon reacts with air to produce hydrogen and carbon monoxide, a mixture industrially known as syngas. As Eq. 2.3, water gas shift reaction plays an important role in both combustion and reforming processes. This reaction is a reversible reaction produce carbon monoxide and water vapor to /from carbon dioxide and hydrogen. As an exothermic reaction, heat generation increases the surrounding temperature and the reaction is self-sustained. In steam reforming (Eq. 2.4), instead of air, water reacts with hydrocarbon to produce syngas. This process is highly endothermic, and thus requires an external heat source to sustain the reaction. Another reforming process is dry reforming (Eq. 2.5) in which a hydrocarbon reacts with carbon dioxide to produce syngas. Dry reforming is also highly endothermic such that an external heat source is required.

$$\mathrm{CH_4(g) + 2O_2(g) \rightarrow CO_2(g) + 2H_2O(g)} \quad \Delta H_r^\circ(298\ \mathrm{K}) = -803\ \mathrm{kJ\ mol^{-1}} \tag{2.1}$$

$$\mathrm{CH_4(g) + 1/2O_2(g) \rightarrow CO(g) + 2H_2(g)} \quad \Delta H_r^\circ(298\ \mathrm{K}) = -36\ \mathrm{kJ\ mol^{-1}} \tag{2.2}$$

$$\mathrm{CO(g) + H_2O(g) \rightleftarrows CO_2(g) + H_2(g)} \quad \Delta H_r^\circ(298\ \mathrm{K}) = -41\ \mathrm{kJ\ mol^{-1}} \tag{2.3}$$

$$\mathrm{CH_4(g) + H_2O(g) \rightleftarrows CO(g) + 3H_2(g)} \quad \Delta H_r^\circ(298\ \mathrm{K}) = +206\ \mathrm{kJ\ mol^{-1}} \tag{2.4}$$

$$\mathrm{CH_4(g) + CO_2(g) \rightleftarrows 2CO(g) + 2H_2(g)} \quad \Delta H_r^\circ(298\ \mathrm{K}) = +247\ \mathrm{kJ\ mol^{-1}} \tag{2.5}$$

In literature, syngas formation by methane CPOx is often discussed in terms of a direct partial oxidation route (Eq. 2.2) as opposed to a combustion-reforming route (combination of Eqs.2.1, 2.4, and 2.5). However, the syngas formation pathway cannot be specifically determined experiments using just reactor exit composition data, especially where the reaction is often close to thermodynamic equilibrium. Spatial profile measurements along the length of a premixed adiabatic plug flow reactor with Rh and Pt catalysts coated onto Al_2O_3 foam substrates show that H_2 and CO are formed in a short oxidation zone at the entrance of the foam and upon complete O_2 consumption by steam reforming [23]. A plot from that work is given in Figure 2.1. CO_2 reforming (Eq. 2.4) was not observed. The formation of H_2 in the presence of gas-phase O_2 is due to a strong film transport limitation leading to a vanishing O_2 concentration at the catalyst surface [24].

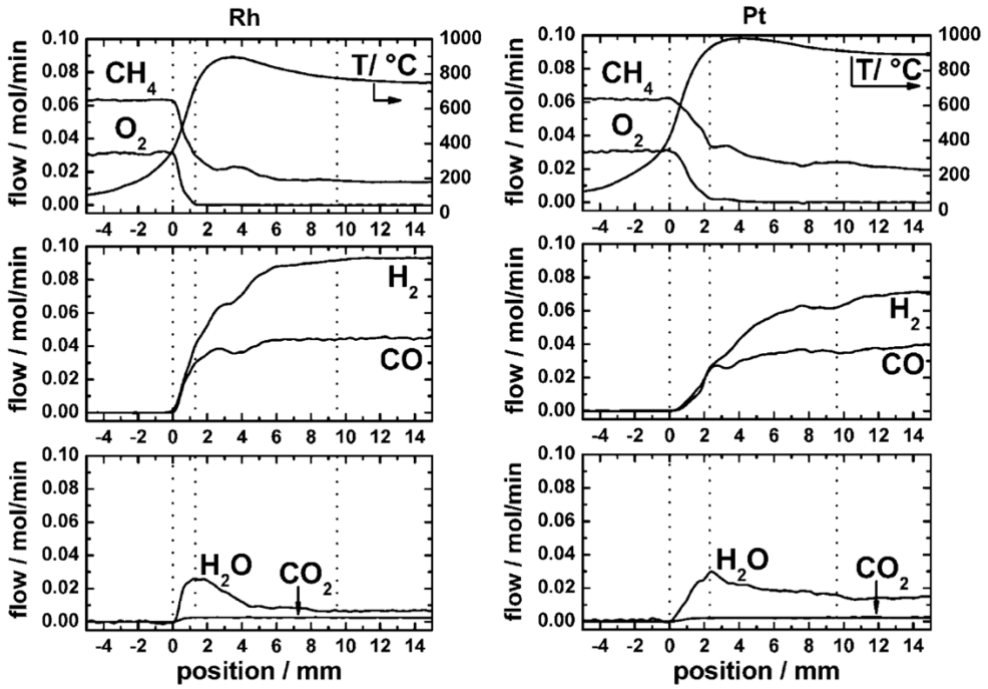

Figure 2.1 Spatially resolved species and temperature profiles for syngas stoichiometry (C/O = 1.0) and a total inlet flow of 4.7 slpm. Rh (left panels), Pt (right panels). 'Oxidation zone' is between the first and the second dotted line. 'Steam-reforming zone' is between the second and the third dotted line from left. Reproduced from [23].

Premixed partial oxidation reforming is usually accomplished catalytically over nickel or precious metal catalysts [25-28] or non-catalytically using unique heat exchange techniques to increase reaction rate [29, 30]. Premixed plug flow bench reactors are the most popular traditional reactor used in reforming reaction research [22, 25].

Non-traditional premixed catalytic oxidation has been comprehensively studied both numerically and experimentally. For example, Ghermay et al. studied catalytic combustion of $H_2/O_2/N_2$ mixtures over platinum in a duct-type rectangular-shaped catalytic reactor with the catalyst coated on the duct surfaces [31]. They applied thermocouples and planar laser induced fluorescence (PLIF) to measure local temperature and investigate 2D OH radical concentration. A

2D numerical model was built for the reaction with both gas phase and surface mechanisms which agreed well with experiments. Kinetic interactions between hydrogen and carbon monoxide catalytic oxidation were also studied with the same reactor [32]. Dilution effects of H_2O and CO_2 were also studied [33]. In their work, the reactor was subjected to a variety of different pressure and preheated temperature conditions. Multiple diagnostics methods were also employed.

In other work, non-traditional premixed reforming has been examined. The Deutschmann group developed and studied non-traditional reforming concepts from the aspects of reaction mechanisms and numerical modeling [34]. For example, in one study they explored heterogeneous methane oxidation using a stagnation flow over resistively heated polycrystalline platinum foil and similar qualitative results were observed between numerical simulations and their experiments. Janardhanan et al. [34] numerically investigated on-board fuel reforming of solid-oxide fuel cells with a catalytic plate reactor design. They built the numerical model by coupling the interactions of mass and heat transport with detailed kinetic schemes of catalytic surface reaction. A number of catalytic reforming related mechanisms has been examined by the same group; however, the research was mostly limited to light hydrocarbon reforming. Fuel conversion kinetics for CPOx of heavier fuels like liquid hydrocarbons in these reactors have yet to be published in the literature.

Alternative concepts for liquid fuel reforming have also been investigated with reactors that incorporate vaporizing and reacting in a very short residence time over a catalyst to avoid soot formation. The Schmidt group for example, studied reactive flash volatilization with gasoline

surrogate compounds and found complete fuel conversion could be achieved by atomizing the fuel and impacting droplets on a hot catalytic surface [35, 36]. This reactor provides fairly robust process to produce syngas and olefins under a high selectivity and conversion. However, this approach is limited to fuel and air are premixed prior to entering the catalyst and it is only possible at high operation temperature.

2.2 Small Scale Reactors

Premixed Reactors

Small-scale integral catalytic reactors are used to study gas and surface phase transport and chemistry over a broad range of thermochemical conditions. Typical reactor types are plug-flow reactors for both supported and unsupported materials [1, 2], wire gauge reactors [3], and stagnation flow reactors [4, 5]. Most small-scale reactors operate with premixed and preheated reactants, which simplifies experimental measurement for kinetic rate models. However, disadvantages of premixed reactors include the potential occurrence of undiagnosed gas phase reactions before the catalyst material by preheating [6] and catalyst deactivation through fouling mechanisms like carbon formation. Some have proposed short contact time catalytic reactors to overcome such disadvantages in traditional integral catalytic reactors. For example, Schmidt et al. studied premixed reactive volatilization for partial oxidation of liquid fuels [7] that avoids carbon formation by co-flowing atomized fuel with air onto a hot catalyst surface. Other work, including ours, have

examined non-premixed configurations for liquid fuels that directly evaporate liquid fuels in a Stefan flow towards a porous catalyst while oxidizer flows from the opposite direction [8, 9].

Non-premixed Reactors

In a non-premixed reactor, fuel vapor and oxidizer are separated by a reaction zone, thus high temperatures are avoided in rich regions where carbon formation is likely. Aicher and Szolak investigated a non-premixed approach for directly evaporating and partially oxidizing diesel fuel in a non-premixed tubular reactor with a concentric catalyst-coated metal mesh located inside the tube [37, 38]. A global ϕ_g up to 7.2 was achieved, but the local equivalence ratio on the catalytic mesh and its effects on catalytic reactions were not attainable due to the reactor's complex geometry. Another non-premixed study performed by Hong *et. al* used a membrane to concentrate oxygen from air and create an counter-flow reaction form [39]. Although non-premixed reactors show promise for high ϕ_g reforming, the impact of local species concentration (i.e., local equivalence ratio) on reaction products and reforming efficiency has not been thoroughly examined [40, 41]. Therefore, there remains a clear need for an alternative reactor to realize more efficient, higher ϕ_g reforming and residue-free vaporization of liquid hydrocarbon fuels.

Non-premixed Reactive Volatilization Reactor

In previous work, our group developed a non-premixed reactive volatilization reactor that the evaporation of liquid fuel from an open pool is driven by the heat from oxidation reaction. A circular catalytic mesh is placed between the diesel pool and the air jet where a laminar flame forms

in combustion studies. With such arrangement, it is possible to adjust local equivalence ratio of the oxidation reaction (ϕ_{mesh}) by changing the position of the mesh and short residence time catalytic reforming can be studied at different local stoichiometry. The ϕ_{mesh} flexibility distinguishes the counter-flow reformer from the typical application of such reactor design in counter flames where the local fuel-air mixture at the flame is approximately stoichiometric as shown in Fig. 2.2. The open counter-flow arrangement provides access of *in-situ* temperature and species measurement for both traditional diagnostics and optical diagnostics (e.g. tracer planer laser-induced fluorescence). Furthermore, a simplified 1-D model is implemented using a flame sheet approximation to simulate the catalytic mesh reactions. Simulation results explain experimental results obtained using n-dodecane fuel in a novel counter flow reactor with different catalyst, airflow and catalytic mesh axial location.

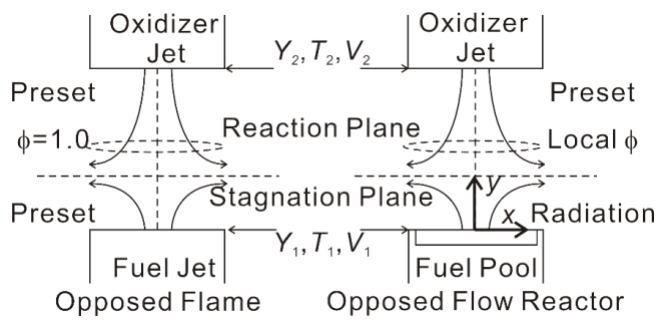

Figure 2.2 Schematic of the counter-flow reactive volatilization model

Counter-flow Flame Burner

Counter flow flames are normally considered to be non-premixed diffusion flames since fuel and oxidizer are separated. The combustion reaction occurs at the interface of the fuel and oxidizer jets. A thin layer space of reaction, usually called 'flame sheet' is generated by diffusion effect of

reactants. Therefore, aerodynamic effects must be included in counter-flow flame studies. Furthermore, the flame velocity of a counter-flow flame is not possible to be defined experimentally. In such a flame, the diffusion velocity is usually not fast enough for high rate chemical reaction, which makes the characteristic chemical time t_c much longer than the characteristic diffusion time t_d. The combustion reaction only occurs in a narrow mixture range around stoichiometric. The chemical reaction rate is considered as infinity so that the flame sheet is considered infinitely thin. This assumption is generally referred to as the flame sheet model. There are two primary types of counter-flow flame reactors as illustrated in Figure 2.3: (1) counter gaseous jet burner, and (2) forward stagnation porous burner. Potter *et al* [42] and Otsuka *et al* [43] focused on the counter gaseous jet burners. Counter-flow diffusion flame is between the counter fuel jet and the oxidation jet in counter gaseous burners. In contrast, forward stagnation porous burner generates counter-flow diffusion flame at the stagnation region between a cylindrical porous tube and coming flows. The fuel is usually supplied through the porous tube and coming flow is applied as oxidizer.

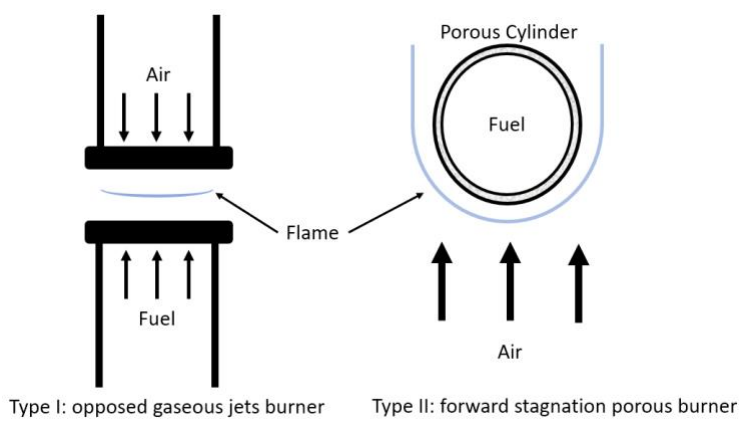

Figure 2.3 Counter flow diffusion fames into two types. Reproduced from [44].

The counter-flow flame is a reliable tool for many combustion problems, such as inhibition effect, dilution limits of diffusion flames, blow-off mechanisms, and *etc*. Tsuji's group was focused on the extinction limit of counter-flow diffusion flame with a forward stagnation porous burner [44]. In the theory by Manton and colleagues, two types of blow off mechanisms affect flame extinction; a low fuel supply rate or temperature lower than the critical value causes the extinction [45]. Inhibition experiments were first done by Friedman *et al* back to 1963. [46]. They were focused on alkali metal vapor and organic inhibition effects in a diffusion flame. Subsequent work, such as that performed by Ibiricu, Milnne, and other groups studied this topic in a variety of ways. [47-49].

More recently, counter-flow flames have become a canonical configuration to study flame stability, soot formation, and other topics. Law's group was focused on the pulsating instability of counter-flow flame and low temperature ignition mechanism with a counter-flow flame burner, among other topics [49, 50]. Ju's group also used counter-flow reactor in experimental study of the low-temperature diffusion flame extinction, non-equilibrium plasma-assisted methane oxidation, dynamics and structure of self-sustained premixed cool flame [51-53]. Chuang's group focused on soot formation process based on experiments with a counter-flow flame reactor, such as A PAH growth mechanism, strain rate effect on soot characteristics, quantification of extinction mechanism, and *etc*. [54-56].

2.3 Catalytic Deactivation and Soot Formation

One of the most important research topics of catalyst is the study of catalytic deactivation. In generally, there are four different types of deactivation: fouling, crushing, thermal degradation and poisoning. [6] Most commonly used catalysts such as Pt, Rh, Pd, Ni based catalyst *etc*. have been reported in studies of deactivation behavior in steam reforming. [57-61] In partial oxidation and reforming reaction, the most significant deactivation is caused by soot and coke formation. In the ethanol reforming process, there are couple ways to form soot. The first way is ethylene polymerization to coke, especially in ethanol and long chain hydrocarbon reforming and CPO. Ethylene, a critical precursor in coke formation, is commonly generated by dehydration and dehydrogenation reactions. There are also other methods, such as the Boudouard reaction, reverse carbon gasification, and hydrocarbon decomposition where carbon deposition is generated instead of coke. The formed coke and carbon then cover the active sites on the catalyst reducing its reactivity.

To solve the coking problem in reforming catalysts, there are two major paths: remove the coke/carbon after its generation or reduce its formation in the first place. A typical way to resolve the coke formation issue is periodically regenerating the catalyst in 2% oxidation environment at 400 ˚C for an hour [62]. There are reported studies of alternative regeneration strategies on various catalysts, fuels, and fuel surrogates [63-66]. However, regeneration will induce addition cost for the operation and cannot recover full catalyst performance which greatly limit the catalyst

application. Alternatively, minimizing the carbon and coke formation during the catalytic reaction is a more efficient and economical to extend catalyst lifetime. A common way to reduce the soot formation is controlling the feed composition. Studies by different groups suggest that a higher water to ethanol ratio could reduce soot formation, especially for ratios over 6. [67-69] A lower carbon to oxygen ratio also extends the catalyst lifetime and delays the deactivation. Such oxygen-rich environments help the coke/carbon gasification on the catalyst surface. In literature, a variety of studies have discussed the benefit of oxygen on soot formation in oxidative steam reforming, partial oxidation and autothermal reforming reactions [70-74]. Other ways to reduce soot formation, such as catalyst modification, have also been examined but are beyond the scope of this work.

2.4 Ethanol Autothermal Reaction and Reaction Pathway

As global warming intensifies due to fuel combustion, while at the same time, market demand for carbon-based fuels increase, the need for an alternative eco-friendly fuel becomes imperative. Hydrogen has become one of the candidates as an alternative fuel and as a carbon-free energy carrier. Steam reforming and autothermal reforming of methane are important processes in hydrogen generation. Ethanol is another potential candidate with greater renewability than natural gas as it is mostly produced by biomass, such as corn, sugar cane etc. Ethanol reforming has also been demonstrated in other fields such as fuel cell and coupled to engines for vehicles [58, 75-77].

Typical catalysts used in ethanol reforming are noble metals (e.g. Pt, Rh, Ru and Pd) or transition metals (e.g. Ni, Co, and Cu). Most catalysts function by lowering the breaking energy of the C-C bond and reforming C1 intermediates to syngas. Due to the complexity of ethanol reforming, the detailed reaction pathways have yet to be fully discovered. However, the pathway is known to be highly dependent on reaction temperature, residence time, catalyst type and feed composition [61, 78].

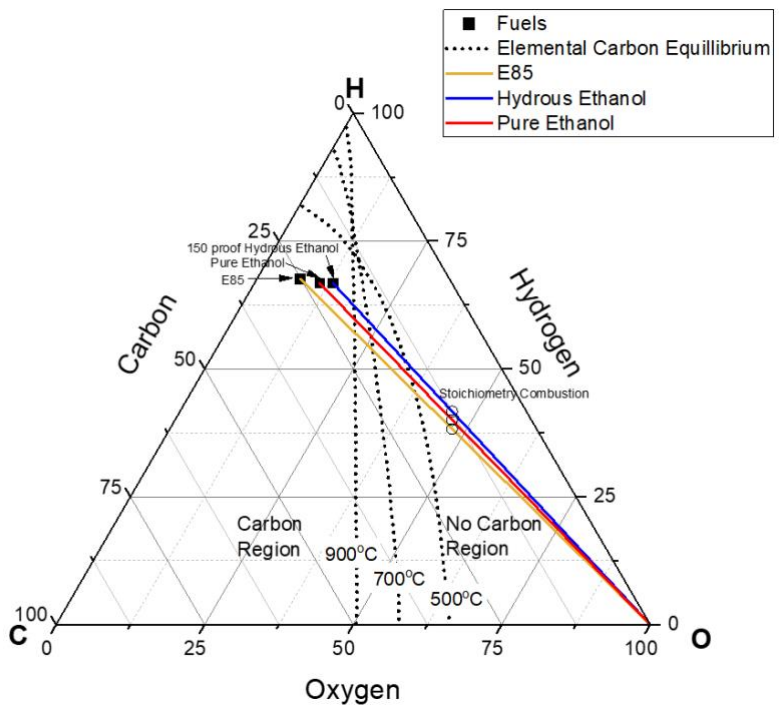

Figure 2.4 Carbon region and carbon free region for different ethanol related fuel

In ternary diagram Fig. 2.4. The dashed lines represent the carbon formation region based on thermodynamic equilibrium [36]. The three colored lines represent partial oxidation reactions of E85 (yellow), pure ethanol (red) and 150 proof hydrous ethanol (blue), respectively. On the three lines, the stoichiometry combustion of fuels is shown with a circle. On the left side of the

stoichiometry combustion point, the feed mixture is considered to be a rich mixture. The right side is the lean mixture region. Lean conditions for all types of fuel are soot free based on thermodynamic limits. There is only a very small region on the rich side that are soot free at 500 ˚C. Autothermal reforming for the three fuels is more interesting in rich conditions. This indicates that soot/coke formation is a critical problem for ethanol autothermal reforming. More importantly, the ternary diagram shows only an equilibrium calculation condition; the surface kinetics and ethanol reforming reaction pathways may be dominant in carbon formation

$$C_2H_5OH + H_2O \rightarrow 2CO + 4H_2 \qquad 2.6$$

$$C_2H_5OH + 0.5O_2 \rightarrow 2CO + 3H_2 \qquad 2.7$$

$$C_2H_5OH + 3O_2 \rightarrow 2CO_2 + 3H_2O \qquad 2.8$$

$$C_2H_5OH + (3-2x)H_2O + xO_2 \rightarrow 2CO_2 + (6-2x)H_2 \quad 0 < x < 0.5 \qquad 2.9$$

Equation 2.6 are the steam reforming (SR) reaction; equation 2.7 are partial oxidation reaction (CPOx) with ethanol as the fuel. Equation 2.9 shows the ethanol combustion; and equation 2.9 states the autothermal reforming (AR). SR reaction has the highest H_2 production, while its endothermic feature requires external heat source. CPOx reaction is exothermic such that it self-sustains easily. However, the H_2 generation of CPOx is much lower than SR reaction. Additionally, the exothermic feature of CPOx lowers the heating value of the fuel, leading to a lower overall efficiency for on board vehicle applications.

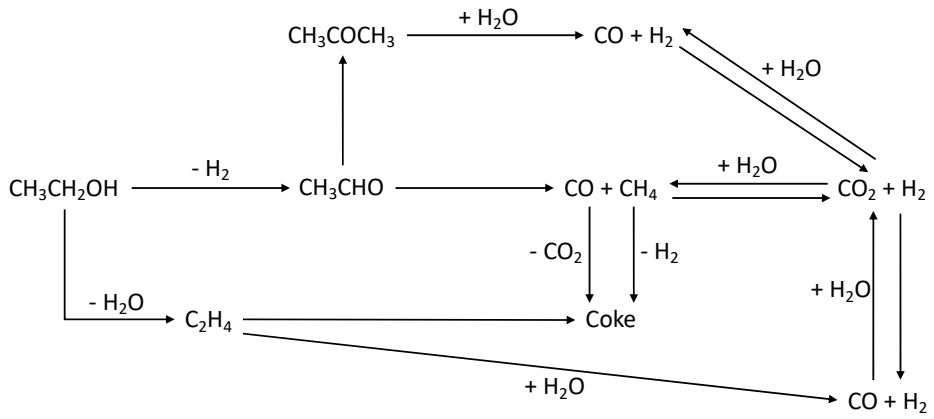

Figure 2.5 Ethanol catalytic reaction pathway. Reproduced from [78].

There are many factors that complicate the ethanol reaction pathway. The general reaction steps are illustrated in Figure 2.5. The major route is ethanol dehydrogenation to acetaldehyde, followed by further decomposition to methane and carbon monoxide, and methane steam reforming to carbon dioxide and hydrogen. The water-gas shift and reverse water-gas shift reactions further affect the concentrations of carbon dioxide, carbon monoxide, water and hydrogen. The minor route is acetaldehyde condensation to form acetone, and acetone decarboxylation to form carbon monoxide and hydrogen. Additionally, ethanol dehydration to ethylene is another minor route. Coke is formed by ethylene polymerization and deactivates the catalyst. Other soot/coke formation pathways are methane cracking, Boudouard reaction, and reverse of carbon gasification which are usually associated with methane reforming and water gas shift [78]. The actual reaction pathway is highly dependent on reaction temperature, residence time, feed composition and type of catalyst as previously discussed.

As a further example of how catalyst type affects the reaction pathway, we can examine the case of Pt/Al_2O_3. Bassagiannis and Panagiotopoulou along with others studied Pt, Al_2O_3 and Pt/Al_2O_3 effects to the reaction [79-82]. They found either Pt or Al_2O_3 alone is inefficient for ethanol reforming. Instead, the combination of Pt/Al_2O_3 improves the conversion of ethanol. This indicates ethanol reforming process is accomplished in a bifunctional manner: ethanol performs dehydration/dehydrogenation on the surface of the support (Al_2O_3 in this case) and metal (Pt) shifts activity to low temperature and lowers the activation energy of C-H bound [83, 84]. The most activity occurs at interface between metal and support, thus illustrating that it is important to examine the metal and support together to determine the reaction pathway for ethanol reforming.

2.5 Advanced Laser-based Diagnostics

Basic Laser Diagnostics Applications

Combined with the development of the laser and detection technology, advanced laser-based diagnostics play an increasingly important role in the combustion research. One typical example of a laser application is remote sensing for combustion and gas dynamic diagnostics. In reacting flows research, laser-based diagnostics systems are widely used in measuring species concentrations, temperature (T), pressure (P), density (ρ), and velocity (u). Specifically, for combustion and other reacting flow research, commonly used laser diagnostics tools are laser induced fluorescence (LIF), planar laser induced fluorescence (PLIF), spontaneous scattering methods based on Raman and Rayleigh scattering, particle image velocimetry (PIV), laser Doppler anemometry (LDA), and other

non-linear diagnostics such as coherent anti-Stokes Raman scattering (CARS) and laser-induced grating scattering (LIGS) [85].

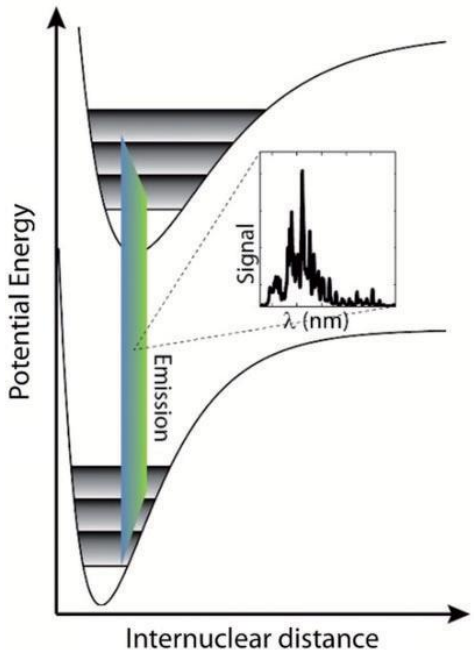

Figure 2.6 Schematic of the molecular energy structure displaying energy states with different vibrational and rotational quantum numbers within two electronic potentials. Fluorescence light with a spectral energy distribution is emitted as the molecule relaxes to its electronic ground state. Reproduced from [85].

Among the laser diagnostic techniques used in the reacting flows field, planer laser induced fluorescence is a popular spectroscopic method for species detection, flow visualization and study of molecular structure. In a typical PLIF system, a laser sheet is used to stimulate the target atoms/molecules to a higher energy state where they would then emit fluorescence (Fig. 2.6). One of the most important application of PLIF system is detecting combustion intermediated species, such as OH, CH, HCO, CH_2O, CN, NO, H atom and O atom [86-93]. In combustion research, the hydroxyl radical (OH) is one of the most important species since it is most likely to be detected in

the post-flame region, due to which OH is frequently used in tracing the flame front. Imaging using OH PLIF shows a distinct gradient of OH in the flame front [94-98]. An alternative way to track the flame front is to visualize the intermediate species CH or HCO. These species are generated and consumed in a thin layer of flame front [99-103]. Also, the PLIF diagnostic can be used to track the preheating chemistry region by detecting the presence of formaldehyde [85].

Toluene PLIF for Temperature Imaging

Image tracer species are commonly applied in gas flow and temperature studies. The most popular tracers are Acetone (C_3H_6O), Toluene (C_7H_8), and 3-pentanone. PLIF can track larger molecules through continuous absorption spectra signal in the ultraviolet region and such larger molecules have more complex energy diagrams than the radicals discussed previously. Detailed characteristics and application of toluene fluorescence are discussed in depth in the literature [104-106].

Two types of toluene PLIF temperature measurement methods are commonly described in the literature, single-camera thermometry and two-camera thermometry. In 2010, Yoo *et al*. demonstrated that single-band toluene could be used for PLIF thermometry and flow visualization in shock tubes. In 2013, Miller *et al*. demonstrated two camera thermometry in the same application. The fluorescence signal of toluene S_f collected is given as Equation 2.10. This equation consists of three parts: the first part $E/(hv)$ shows the incident photon, where E is the energy per pulse of the excitation beam, h is Planck's constant, and v is the frequency of the excitation light; the second

part states the photon absorption condition $n_{tot}\sigma\ (\lambda_{ex}T)$, where n_{tot} is the number density of the fluorescing species and σ is the absorption cross-section; the third part is the fluorescence quantum yield, which also states the fraction of photons reemitted as fluorescence; the last part η is collection efficiency that states the response of the imaging system. In Equation 2.10, the cross-section area and the fluorescence quantum yield are functions of temperature.

$$S_f = \frac{E}{h\nu} n_{tol}\sigma\left(\lambda_{ex,}T\right)\phi\left(\lambda,\lambda_{ex},T,P_{tol},P\right)\eta\left(\lambda\right) \qquad 2.10$$

For single-camera thermometry, temperature can be measured under a steady state condition. The ratio of imaging signal from measurement and calibration are determines the temperature profile. This application is especially easy to use in a shock tube configuration where the calibration imaging signal can be replaced by an upstream and downstream of an oblique shock. The Mach number together with the oblique angle can be used to calculate the upstream image for calibration. More details about this technique is beyond the scope but can be found in literature [107-109].

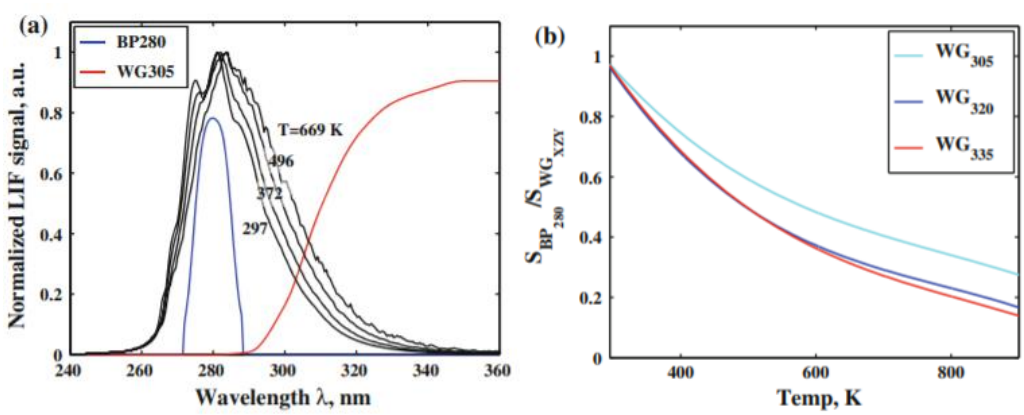

Figure 2.7 (a) Toluene fluorescence spectra as a function of temperature at 266 nm excitation. Data courtesy of Koban et al. (b) expected signal ratios as a function of temperature for dual-band thermometry, for a BP280 filter paired with a WG305 (cyan), WG320 (blue), and WG335 (red) filter; curves correspond to third-order polynomial fits. Reproduced from [110].

In two-camera thermometry, toluene fluorescence exhibits a redshift with temperature increment (Fig. 2.7) [110]. Here, the temperature could be measured by the ratio of the two spectral region (such as 280 nm and 320 nm) image intensity. When considering each camera, and one local pixel response with a selected band filter under constant pressure, Eq. 2.10 could be simplified as Eq. 2.11, with consistent λ_{ex}, and P. Additionally, the energy incidence parameters and number density are the same for each pixel. Then we have the ratio of the two intensity signals as Eq. 2.12 with only two parameters – temperature and the response of camera. By use a single ICCD camera with an image separate system, the difference in responses from the two cameras is also eliminated. The remaining unknown parameter is temperature, which can be calculated from the measurement taken with two different bands.

$$S_{f_i} = \frac{E}{h\nu} n_{tol} \sigma(T) \int F_i(\lambda) \phi(\lambda, T) \eta_i(\lambda) \mathrm{d}\lambda \qquad 2.11$$

$$\frac{S_{f_1}}{S_{f_2}} = \frac{\int F_1(\lambda) \phi(\lambda, T) \eta_1(\lambda) \mathrm{d}\lambda}{\int F_2(\lambda) \phi(\lambda, T) \eta_2(\lambda) \mathrm{d}\lambda} \qquad 2.12$$

2.6 Applications of Fuel Reforming

Catalytic partial oxidation reforming is one of the most promising technologies for converting petroleum fuel to H_2 rich syngas and other hydrocarbon feedstocks. Associated with an increasing supply of the shale gas, natural gas consumption has increased in recent years [111]. As a result, more and more industry-scale catalytic partial oxidation plants have been established. Hydrogen-rich syngas production from methane can be achieved by many reforming reaction pathway

including steam reforming, autothermal reforming (ATR), partial oxidation (POx) and catalytic partial oxidation (CPOx) [112]. Their pros and cons are summarized in Table 2.1.

Table 2.1 Summary of pros/cons and industrial developer of popular methane reforming technologies. Reproduced from [112].

	Pros	Cons	Developer
SMR	▪ No oxygen plant Required ▪ Lowest operating temperature ▪ High H_2 yield ▪ Most extensive industrial development	▪ High CO2 in exit steam ▪ High air emission ▪ Need external heat ▪ Need additional gas separation	Haldor Topsoe AS, Foster Wheeler Corp, Lurgi AG, International BV, Kinetics Technology and Uhde GmbH
ATR	▪ Syngas composition can be adjusted by outlet temperature ▪ Lower processing temperature	▪ Need oxygen plant ▪ Need additional gas separation	Lurgi, Chevron and Nigeria National Petroleum Corporation, Sasol, Haldor Topsoe
POX	▪ Deed stock desulfurization not required ▪ No need for external heat or heat exchange	▪ Need oxygen plant ▪ Very high operating temperature ▪ Excessive heat needs to be removed	Texaco Inc. and Royal Dutch/Shell
CPOx	▪ Compact design allows low capital cost and higher flexibility ▪ Ideal CO/H_2 ratio ▪ No need for external heat or heat exchange ▪ High carbon efficiency	▪ Need oxygen plant ▪ Need Feedstock desulfurization ▪ Limited commercial experience	Exxon Mobile leaded pilot test

For internal combustion engine powered vehicles, engine exhaust waste energy can be used as a heat source for reforming the fuel to create a secondary fuel [11, 113-116]. The secondary fuel provides different ignition reactivity enabling the application of advanced combustion modes such as reactivity-controlled compression ignition (RCCI) [117-119]. Such modes can increase overall engine thermal efficiency and can reduce exhaust emissions of soot and nitrogen oxides (NOx) [118, 120, 121].

One example of an integrated reforming system with an engine is illustrated in Figure 2.7. Here, the primary fuel is separated into two streams: one stream flows through a heat exchanger to recover the heat from high temperature products. The preheated primary fuel 2 flows into the reformer and the products (secondary fuel) leaves the reformer as 3 flow from the other side of the heat exchanger. The secondary fuel combines with primary fuel to supply the engine. The engine exhaust also provides additional heat for endothermic reforming reactions.

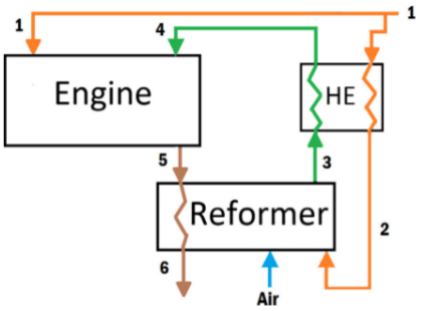

Figure 2.8 An example of catalytic partial oxidation fuel reforming in engine application using exhaust waste heat recovery to preheat reactants. Reproduced from [116].

In conclusion, Catalytic partial oxidation (CPOx) is promising in producing syngas H_2 and CO. It is suitable for compact reactor application such as mobile fuel-processing systems for fuel cell and on-board vehicle reforming. Most currently available small-scale reactors operate with premixed and preheated reactants, enjoying the simplified experimental measurement for data used in kinetic rate models. However, disadvantages of premixed reactors include potentially undiagnosed gas phase reactions occurring prior to the catalyst material caused by preheating and catalyst deactivation through fouling mechanisms like carbon formation. Also, traditional reactors operate under a low equivalence ratio (ϕ<3) to avoid soot formation. The limited operation window leads to a heating value loss that reduces fuel economy. To solve the soot formation problem under high equivalence ratios for liquid and gaseous fuels, a new reactor configuration could be a path forward. Non-premixed short contact time reactors like counter-flow reactors allow higher equivalence ratio operation for catalytic partial oxidation is a promising candidate in solving this problem.

Chapter 3 Experimental Apparatus

3.1 Reactor Setup

Basic Gaseous Counter-flow Reactor

The novel reactor presented in this body of work is inspired by the classical canonical counter-flow flame burner as previously reviewed in Chapter 2. However, the flame sheet position for our reactor is not determined by mixture stoichiometry and stagnation plane, rather, it is determined by the catalytic mesh location between the oxidizer and fuel. This concept was initially proposed as a reactive volatilization reactor for diesel-like fuel reforming where an open pool was used to feed fuel by evaporation at the bottom and the oxidizer flows from the top [122].

The new reactor given in Figure 3.1 has two concentric tube chambers feeding gaseous reactants towards each other. The top chamber delivers heated oxidizer (air & N_2 mixture) to initiate the catalytic reforming process and the bottom chamber is unheated gaseous hydrocarbon fuel inlet. The gaseous oxidizer is preheated to 300 ˚C by an inline electric heater and a band heater before entering the reaction zone. A round catalytic mesh with an outside diameter of 7.62 cm is placed between the two chambers. The catalytic mesh is held by a 1.5 mm thickness ring support that can be moved vertically by a linear translation stage. The space between two chambers, which is defined as the reaction zone, has a height of 15 mm. Ceramic honeycombs are used as flow

straighteners, and are placed in the both chambers to generate a uniform flow to the reaction zone. Nitrogen purge is applied to shield the reaction from ambient air and block the diffusion of fuel into laboratory environment.

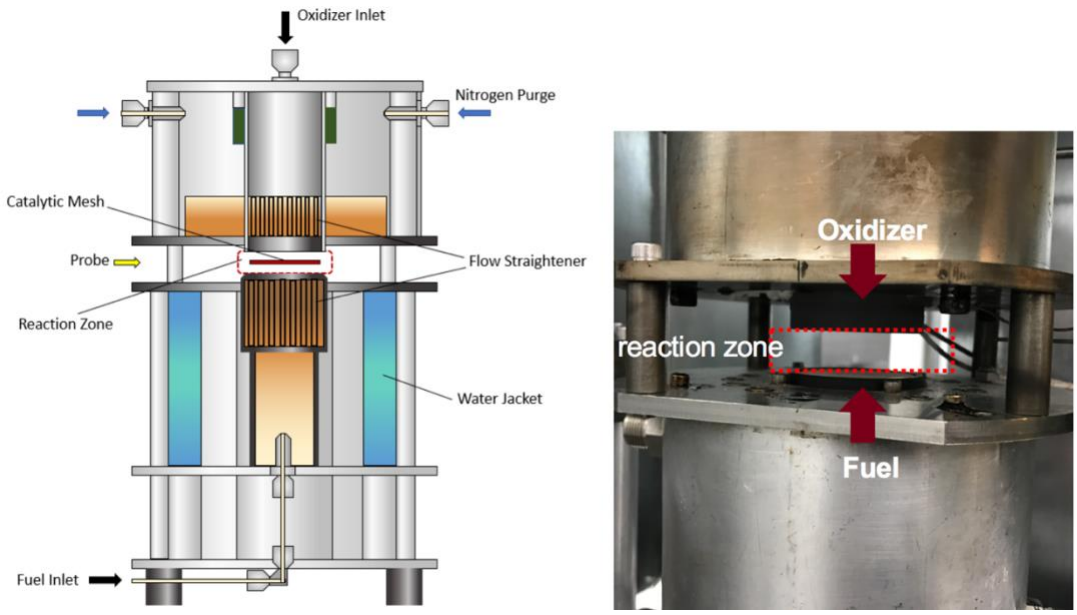

Figure 3.1 Gas phase counter-flow reactor for single mesh configuration

Two-Mesh Configuration Counter-flow Reactor

The counter-flow reactor is designed to conduct staged catalytic reaction experiments and eventually leads to scale-up short-contact time reactors for reforming and other useful reactions. In the two-mesh configuration, the first catalytic mesh supports lean oxidation with platinum as the active material. This mesh is axially adjacent to a second mesh that supports high equivalence ratio CPO using rhodium as the catalytic material. The position of the two meshes is shown in the inset of Figure 3.2. The oxidative catalytic (platinum) mesh is set next to top chamber inlet and reformative catalytic (rhodium) mesh is set between the chambers. The catalyst substrate is made

of wire meshes (50 mm diameter) of 0.3 mm thick Kanthal - D (FeCralloy) wire (18 mesh/inch) with an 61.6% open area. The height (position) of the meshes are controlled by linear stages respectively. The premixed gaseous fuel (research grade methane for this study) and oxidizer (air) is preheated to 450 ˚C by external electric inline heaters before entering the reaction zone. The unheated gaseous fuel (methane) is fed from the bottom chamber into the reaction zone. Ten 200-mesh stainless steel meshes are stacked in the inner chambers to stabilize the flow. In checking the laminar flow uniformity at the exit of the inner chamber, the velocity fluctuation at different inner chamber exit locations is measured by a hot wire anemometer. It was found that the velocity fluctuation was within 4% across the inner chamber exit except very close to the wall under the tested experimental flow conditions.

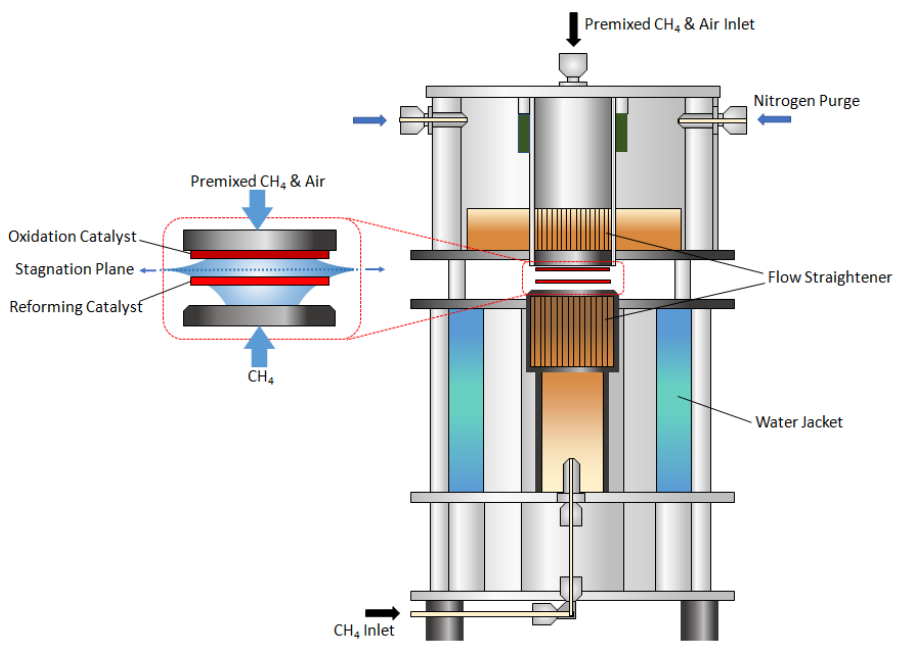

Figure 3.2 Gas phase counter-flow reactor for dual mesh configuration

Liquid Fuel Counter-flow Reactor

The basic configuration of the reactor is modified to accommodate atomized liquid fuel. A diagram of the reactor along with a photo of the experimental setup is shown as Figure 3.3. A 'TI automotive F90000267' high performance in-tank fuel pump designed for ethanol blends fuel up to E99 was used to feed fuel to an injector. This pump is powered by a DC power supply with constant voltage at 13.5 V. The fuel system only needs a small amount of fuel and the extra flow rate were dredge to a reservoir. The fuel is pressurized to 344.7 – 482.6 kPa for different condition. A National Instruments Driver Module is use for controlling a gas fuel atomizer. The driver module includes a Compact RIO module for driving a Port Fuel Injector model that directly controls the atomizer. The control system is initially designed to simulate a two/ four stroke engine. By controlling the rpm of the simulate engine, the spray frequency could be estimate. A flow test is taken to determine the flow rate associated with the spray frequency with each type of fuel. A scale continuously monitors the fuel tank weight during experiment. The weight decreasing rate equals to the fuel consumption rate so that the real time fuel consumption rate is measured for each condition. All flow rates used in experiment are mean flow rate values in 2 min. A pressure gage was used to confirm the fuel spray pressure during the test. The atomizer has been tested in confirming its performance. In this test, a constant pressure vessel has three optical window access for laser-based or light-based diagnostics approaches.

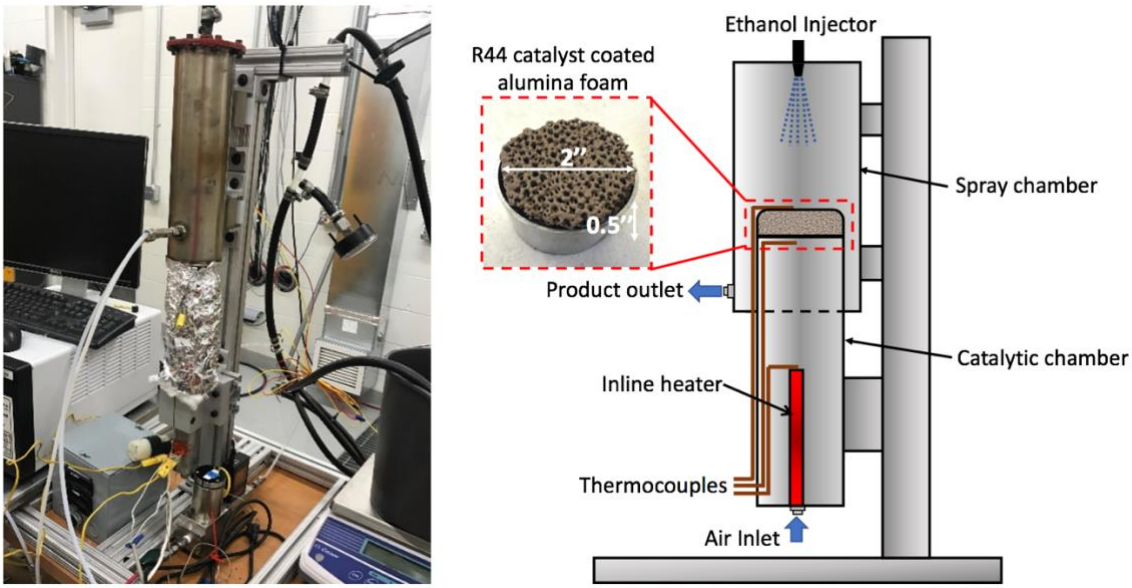

Figure 3.3 Counter-flow atomizer reactor design

3.2 Emission Measurement Equipment

Raman Laser Gas Analyzer (RLGA)

ARI's Laser Gas Analyzer (LGA) was used for gas composition measurement. The equipment is a unique high-speed gas spectrometer that provides continuous measurement for carbon monoxide, oxygen, hydrogen, carbon dioxide, nitrogen and methane. In our system, the sample gas was sent into a chiller to have the water and liquid phase hydrocarbon condensed before entering the gas analyzer. This chilling process provided a safer environment for the laser and detector in the analyzer.

Micro Gas Chromatography (GC)

Two Micro GC Systems were used in the experiments conducted in this work for measuring hydrocarbons: an Agilent Micro Gas Chromatography system and an Inficon Micro Gas

Chromatography Fusion. Due to the limitation of the LGA, any hydrocarbon beyond methane lead to a cross sensitivity by LGA measurement. Both Micro GC's provided an approach for the measurement of the hydrocarbon beyond methane. The Agilent Micro GC 490 has 2 columns (PoraPLOT U and CP-Sil 5 CB) for benzene toluene ethylbenzene and xylene (BTEX) measurement. A preheating sample line and a sampling system were used to main the sample temperature at about 100 ˚C to avoid losing the heavier hydrocarbons. The Inficon Micro-GC system was used for measuring reforming products measurement using two columns (PoraPLOT Q and CP-MolSieve 5 Å). All sample gas for the Inficon GC flowed through a chiller to prevent the water damage the column, thus the concentrations are reported on a dry basis.

3.3 Laser Diagnostic System

System Setup

The laser diagnostic system was used in this work to determine the temperature profile in the reaction zone of the counter-flow reactor. A Neodymium-Doped crystal:Yttrium-Aluminium-Garnet (Nd:YAG) laser was used for this experiment. The laser has a neodymium-doped crystal as the active medium and produces a, near infra-red, 1064 nm pulse. The electrical power supply provides a pulsed power source to the laser system and the optical pumping system produces a population inversion with the flash-lamp to intensify the output signal. Two Second-

harmonic crystals (Harmonic Beamsplitters) were applied to double the frequency of the Nd:YAG laser for 266 nm.

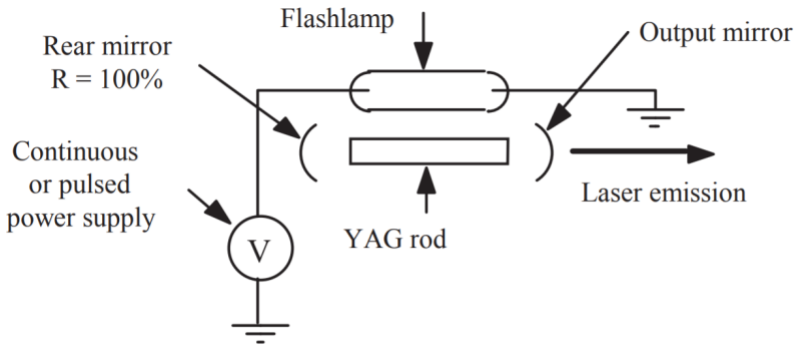

Figure 3.4 Nd:YAG laser scheme. Reproduced from [123].

Planar laser-induced fluorescence (PLIF) is used for instantaneous and non-intrusive diagnostics. Toluene was selected as the tracer since it could be consumed by catalytic reactions so the fuel consumption could be qualitatively inferred [124, 125]. The excitation laser pulse was generated by an Nd:YAG laser with maximum output 120 mJ/pulse at 266 nm. The laser beam is expanded by light-sheet optics into a 10 mm sheet. Toluene fluorescence then propagates through a BG280 band-pass filter (FWHM=10nm) and an intensified CCD camera records the images. The fuel is doped with 5% (volume) toluene allowing for an adequate fluorescence signal level without significantly altering fuel characteristics. The toluene detection limit was estimated to be 600 ppm assuming linear fluorescence regime and a signal-to-noise ratio of 3[126].

Chapter 4 Characterization of Hydrocarbon CPOx Using Gas Phase Counter-flow Reactor

In this chapter, we experimentally evaluate a novel non-premixed counter-flow reactor for reforming gaseous fuels like methane or natural gas. Our reactor is like the canonical opposed-flow reactor commonly used in flame studies but has a catalyst-coated metal mesh located between the air and fuel inlets. The data confirm that the catalytic mesh induces a thin layer reaction region like the flame sheet in a counter-flame burner. Instead of global stoichiometry, local stoichiometry plays an important role in controlling the surface catalytic reaction. The center of the reaction zone follows the similarity model and its unique temperature and stoichiometric gradient with short residence time reduces the potential for soot formation. In summary, this chapter provides the basic understanding of the non-premixed counter-flow configuration. The chapter also provides the important background information to inform how the reactor can be used in on-board reforming applications (Chapter 5), incorporate laser-assisted diagnostics (Chapter 6), and be extended to liquid fuel application (Chapter 7).

4.1 Experimental Procedure

The counter-flow reactor used in the experiments is illustrated in Fig. 3.1. It is similar to the counter-flow reactive volatilization reactor used in previous work but has been modified for gaseous reactants. The top chamber delivers pre-heated oxidizer and the bottom chamber provides unheated gaseous hydrocarbon fuel. The chambers lead to the two concentric planar manifolds that deliver fuel and oxidizer to the reaction zone through honeycomb monoliths for uniform flow distribution. A round catalytic mesh (50 mm diameter Platinum wash-coated 0.3 mm Kanthal-D wire, 18 mesh/inch, 61.6 % open area) was positioned between the two planar manifolds. The axial position of the catalytic mesh was controlled by a linear translation stage. A 1.5 mm thick ring support held the catalytic mesh in desired axial position. Air was preheated to 350˚C using an electrical resistance heater located in the plumbing upstream to the oxidant-side manifold. Unheated gaseous methane (research grade diluted with nitrogen) was fed from the bottom manifold to the reaction zone. The distance between the two gas manifolds was 15 mm. A nitrogen purge system was used to prohibit ambient air from entering the reaction zone. The centerline temperature profile was measured by a 400 µm outside diameter K-type thermocouple and the catalytic surface temperature was measured using an IR temperature sensor. Axial centerline gas samples were collected using a 2.0 mm diameter un-cooled quartz microprobe with a 0.5 mm diameter orifice inlet. The temperature and sample probes were adjusted vertically using a linear stage system. Gas species were analyzed using a Raman laser gas analyzer (RLGA) system

(Atmosphere Recovery Inc., Model RLGA-1800L-BF) that measured dry concentrations of hydrogen, carbon monoxide, carbon dioxide oxygen, nitrogen and methane.

The ignition process relies on the inline heater and band heater installed in the reactor. For the ignition process, the methane inlet is closed at the beginning and only air flows into the reaction zone. The mesh position is adjusted to the highest that gives the best preheating performance of the catalyst. Ignition is only dependent on the catalytic surface temperature, and it is independent of air temperature.

In past experiments, a thermocouple was placed below the catalytic mesh to give a reference of the mesh temperature [122]. However, the catalytic mesh in this case is very thin so it can be assumed that the mesh temperature is very similar to that of the gas flow. The inline heater was set 550-600 ˚C and the band heater was set 500 ˚C for preheating. The temperature discussed here is based on the cases performed using Rh catalyst. The Rh catalyst required higher preheating temperature than Pt catalyst. For Pt ignition, all temperature is set 100 ˚C lower than its Rh counterpart. This preheating process requires maintaining a reasonable air flow rate to avoid overheating that destroys the inline heater. When temperature reaches the set point and is stable, the thermal couple is then removed. The methane and nitrogen purged systems are then turned on. The nitrogen purge system is important not only for isolation, but it also eliminates possible flame ignition in the reactor (methane autoignition temperature 537 ˚C). With the methane flow turned on, the local methane and oxygen stoichiometry distribution is established. The reaction zone has

a locally rich to lean distribution gradient from fuel inlet to oxidizer inlet. The mesh needs to be placed towards the rich side for ignition since the partial oxidation ignition is favored in a rich environment than lean condition. If the ignition fails, the process would be repeated from preheating.

After the catalytic reaction started, all electric pre-heaters were turned off because the rapid heat release of the reaction kept the surface temperature high enough. The catalytic mesh mostly ignited as a hotspot which is not necessary located in the center of the mesh. The hot spot self-sustains the reaction and gradually propagate to the whole catalytic surface. This process takes about 20-30 min before the reaction is fully stable. The heaters could be turned on again at the experiment temperature if needed to stabilize the reaction. The reaction surface should be circular and uniform as Fig. 4.1. Any distorted reaction surface shape could probably be caused by the uneven mesh surface or the unstable flow profile.

Figure 4.1 Typical stabilized reaction surface found during the gas experiments. The center circular region is the ignited mesh.

4.2 Results and Discussion

Flow Pattern/Reaction Model Characterization

The flow pattern of the reactor is critical for understanding the counter-flow reactor, which in turn influences fluid dynamics, gas phase chemistry and surface phase chemistry. The flow pattern also determines the boundary conditions of the reactor. The understanding of flow pattern is also important to decide the mesh location. For example, the boundary condition of the surface reaction is determined not by the mesh location but by the global equivalence ratio. In a traditional diffusion flame reactor, the flow establishes a stagnation plane and equivalence ratio distribution. However, in the counter-flow catalytic reactor, the mesh location determines the reacting equivalence ratio, which directly affects the surface reaction. Therefore, the flow pattern is the headstone for understanding the reactor.

There are three possible flow patterns in the reactor depending on how much the catalytic mesh blocks the gas flow: (1) impingement flow pattern, where the stagnation plane position is wholly determined by the mesh position Fig 4.2(A); (2) diffusion pattern, where the mesh does not affect the stagnation plane position Fig 4.2(B); and (3) the mesh has some effects between the two limited cases. In Fig. 4.2, CHEMKIN simulation was used to demonstrate the possible reaction models. In both cases the chemical mechanism was turned off. In the impingement case (Fig. 4.2(A)), the blocking effect by mesh is very prominent that the flow formed stagnation plane (zero velocity) at the mesh location. The mesh is more like a barrier that blocks the bulk flow but

allows diffusion of the going through speciation. The axial velocity equals to zero at the mesh location. In Figure 4.2(B), the fuel and oxidizer flowed through the mesh easily. The stagnation plane is determined by the flow condition of the fuel and oxidizer. In this case, the reactor follows the similarity model [127] the velocity, temperature, species concentration, and other properties are only a function of axial distance.

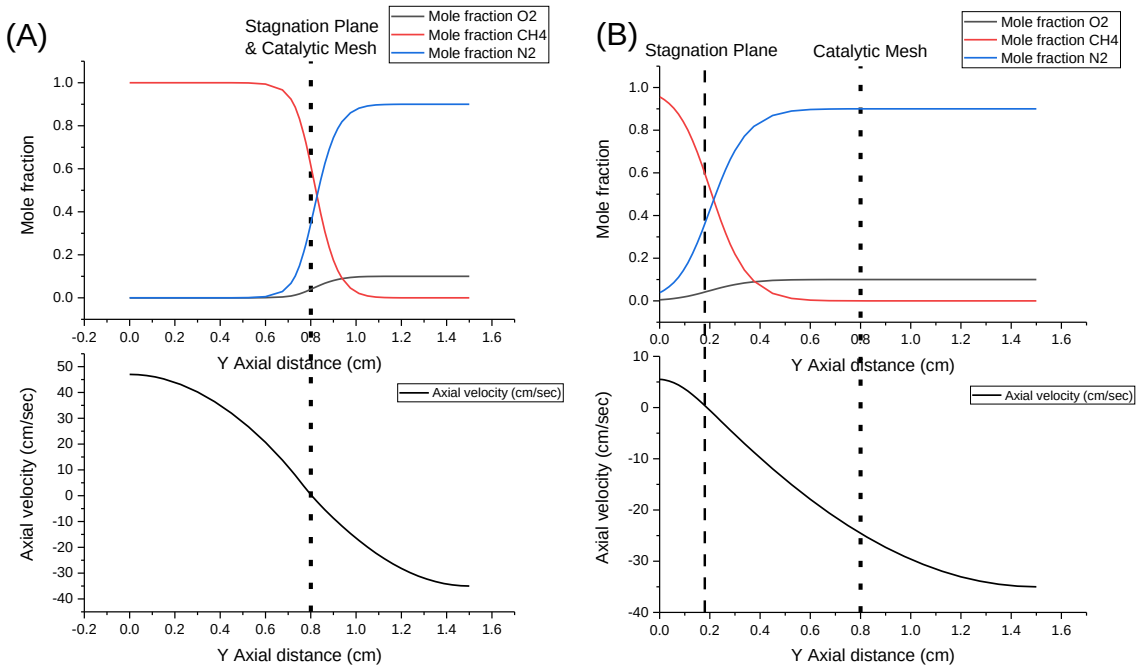

Figure 4.2 Possible reaction models of the gaseous counter flow reactor depending on the resistance of the mesh. (A) Maximum blocking effect (B) Minimum blocking effect by the mesh.

In order to find the actual flow pattern in the experimental reactor, a visualization experiment was conducted. With only the gas flows, oil particles were seeded into the oxidizer stream. A 532 nm laser and highspeed camera were used to perform streak line visualization as shown in Fig 4.2A. By visual evaluation (Fig. 4.2B), it is apparent that the mesh did not affect the flow in the center

region, agreeing with the second possible pattern. Some discrepancies in the flow direction were observed at mesh periphery, which were possibly due to the larger contact angle between the flow and the mesh. In summary, the catalytic mesh did not affect the centerline of the reactor, where the measurements were taken in this work.

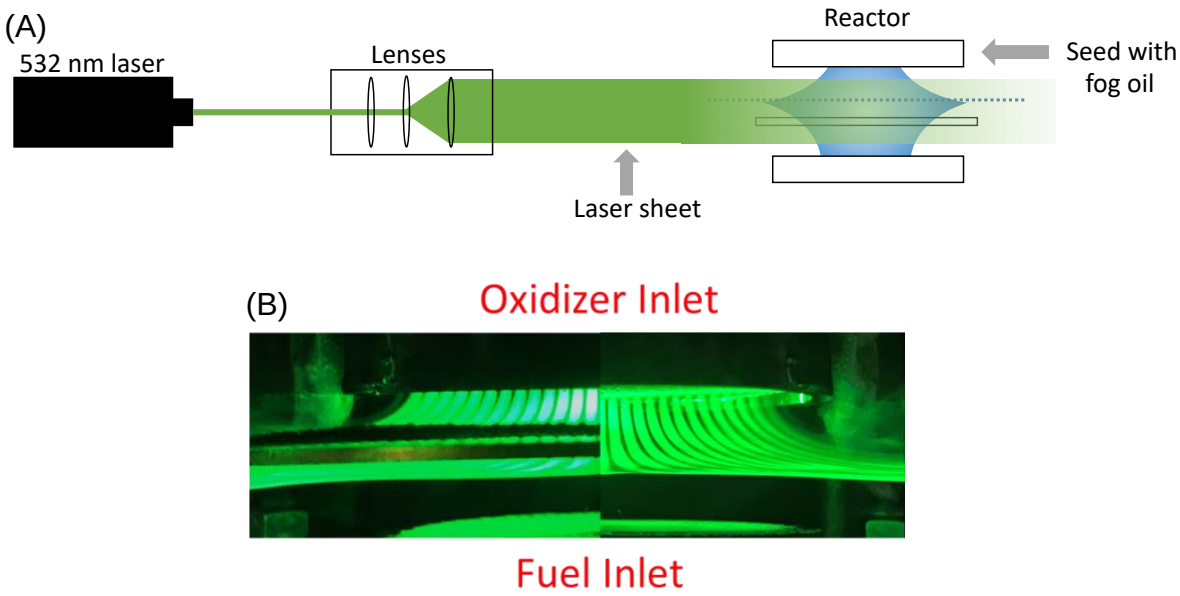

Figure 4.3 Visualization of the flow field in the reactor at a non-reacting condition. (A) Experimental setup. (B) Imaging: Left: with catalytic mesh; Right: without catalytic mesh.

Based on the result of the laser visualization experiment, it can be concluded that the center line region in the reactor followed the similarity model that the stagnation plane is determined only by the flow boundary conditions. With the larger contact angle in the mesh periphery, the flow pattern transits to stagnation model that the stagnation plane is solely determined by the mesh location. In between the centerline and the periphery, there is a transition region that the mesh partially affects the flow (Fig. 4.4). While the contact angle is the major factor, the mesh location

and flow rates also affect the flow pattern. For the centerline where the similarity model always applies, the reaction parameters like temperature, species composition and scale of velocities are only dependent on one direction orthogonal independent variable. It is important to emphasize that such similarity behavior is not the result of any approximation. In this study we are only focused on the centerline of the reactor.

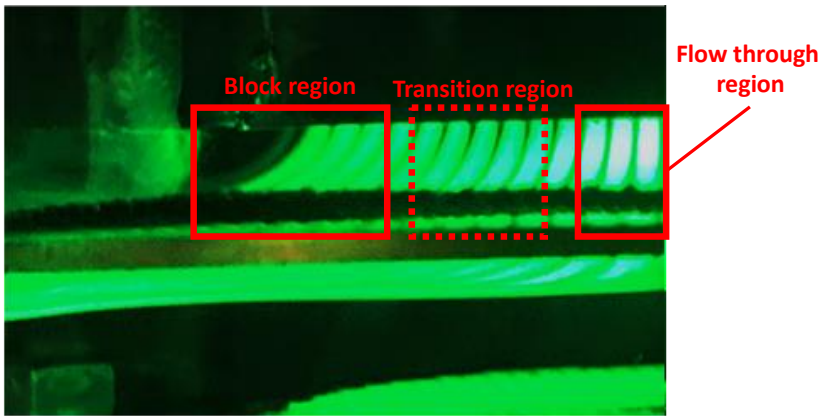

Figure 4.3 Different flow pattern/reaction model apply to different regions of the reactor.

Speciation Spatial Profile

As discussed in earlier sections, in the region of interest for this study the flow pattern for the is unobstructed flow through where the inlet flow rates determine the stagnation plane and local equivalence ratio. It is known that the local equivalence ratio could be chosen by adjusting the mesh location. In this section, the reactor is set to study how the mesh location from the fuel chamber (mesh location = 0 mm) to the oxidizer chamber (mesh location = 15 mm) affects the reforming outcome. 5 different conditions were tested with different local equivalence ratio while keeping the flow condition unchanged (Table 4.1). The local equivalence ratio is estimated by CHEMKIN

simulation. All reported data in this section were run at 300 ˚C oxidizer inlet temperature. The methane fuel flow rate was set to 25 standard liters per minute (SLPM). The oxidizer was a mixture of compressed air diluted with nitrogen (14% oxygen and 86% nitrogen) to lower the mesh temperature, so as to decrease the risk of fuel auto-ignition. The oxidizer overall flow rate was set to 30 SLPM. Global equivalence ratio ϕ_g and local equivalence ϕ_{local} for this experiment calculated for each condition.

Table 4.1 Experimental conditions to study mesh location effect

Condition	Oxidizer flow (SLPM)	Fuel flow (SLPM)	Mesh Pos. (mm)	ϕ_{local} (Pt)	ϕ_g (Pt)
1	30	25	6	58.51	2.33
2	30	25	7	11.45	2.33
3	30	25	8	2.79	2.33
4	30	25	9	0.80	2.33
5	30	25	10	0.26	2.33

In the counter-flow arrangement, the local stoichiometry at the mesh is directly affected by the mesh relative location between the two inlets. And it has been found that the local equivalence ratio is extremely sensitive with axial position as in preliminary experiment. In this work, we chose carbon monoxide and hydrogen mixture (synthesis gas), the key products of catalytic partial oxidization reaction, as the desired reforming products to study the reactor's performance and possible optimization strategies. Product concentrations in each condition was measured and studied. Figure 4.5 depicts the synthesis gas concentration distribution below the catalytic mesh for

different mesh location. Gas samples were taken at the closest available measuring position (about 1 mm) below the mesh for each condition.

For the CHEMKIN model used, a 1D reaction model with detailed gas phase mechanisms and surface catalytic reactions is not readily available and is the focus of our current work. It is desirable to establish a simple model in order to estimate local equivalence ratio. For this purpose, modified GRI 30 mechanism without chemical reaction was used in the simplified model shown here to provide a preliminary guess of ϕ_{local} based on species transportation/diffusion. Consequently, temperature, speciation concentration and flow profile cannot be precisely calculated by this model. Table 1 lists the estimated ϕ_{local} with corresponding mesh location for each tested condition, with boundary conditions set based on experiments.

The synthesis gas production rates of condition 1 (highest ϕ_{local}) and condition 5 (lowest ϕ_{local}) are the lowest among all conditions (Fig.4.5). The synthesis gas concentration is close zero for these two conditions since catalytic mesh location was too far away from the stagnation plane. Fuel or oxidizer could not diffuse to the mesh location so that reaction surface didn't have reactants for these conditions. Furthermore, product concentration dropped rapidly from a rich to a lean condition by comparing condition 3 (ϕ_{local} >1) and condition 4 (ϕ_{local} <1). As mentioned in previous discussions, mesh stoichiometry played an important role in the product concentrations. At the flow rates used in this study, stoichiometric (ϕ_{local} =1) axial position was location between 8 mm and 9 mm above the fuel inlet chamber, so that in a fuel lean conditions such as condition 4 and 5, the

mass fraction of methane was too low to maintain an active reforming process. Thereafter, instead of producing a high concentration of synthesis gas, the fuel was mostly converted to water vapor and carbon dioxide, indicating a catalytic combustion process. In comparison, syngas production rate approximated maximum near ϕ_{local} = 2.0 by the chemistry. From this experiment, condition 3 (ϕ_{local} =2.79) has been found with the highest synthesis gas production (optimized mesh location, 8 mm). We believe at this point ϕ_{local} is close to 2.0 and the mismatch from calculated value could be explained by the error introduced by the model. Nevertheless, the conclusion is that the local equivalence ratio can be utilized to estimate the optimized mesh axial location for synthesis gas production.

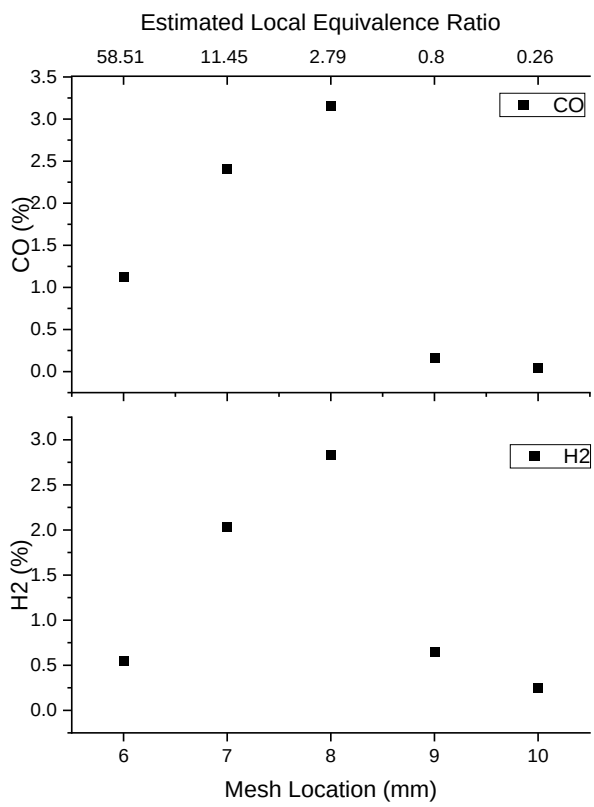

Figure 4.4 Syngas production under different equivalence ratios

In conclusion, the mesh location in this reactor configuration directly affects the local stoichiometry. The local stoichiometry controls the performance of the reactor products, instead of global equivalence ratio for premixed reactor types. In later sections of this chapter, the experimental condition is chosen at where the reaction is the most stable and the syngas catalytic selectivity is the highest.

Characterization of Reaction Efficiency

With the influence of mesh location demonstrated, catalytic efficiency and performance at an optimized reaction condition (i.e. inlet flow rates and mesh location) was examined. In this case, a Rh was taken as the catalytic material as an example (Fig. 4.6) since Rh provides a better syngas generation than Pt catalyst. For the experiment setup, the oxidizer was compressed air set to a flow rate of 20 SLPM; the fuel was a mixture of 50% methane and 50% nitrogen and was maintained at a flow rate of 20 SLPM. The global equivalence ratio (ϕ_g) based on these two flow rates was 4.76. The Rh catalytic mesh was set at an axial position of 8.5 mm above of the fuel inlet. The local equivalence ratio for this setup is calculated to be 3.12.

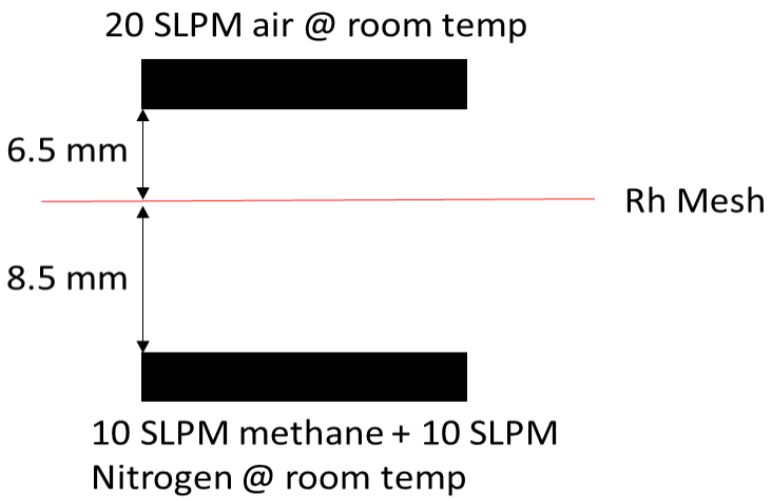

Figure 4.5 Experimental setup of Rh catalytic mesh reaction efficiency characterization.

Species concentrations are useful information to characterize the reactor performance. Importantly, since our reactor is an open system with non-liner, non-uniform chemical reactions, it is not possible to map all the products at every location. Instead, we will apply 'local' conversion at locations of interest, such as the catalyst surface (Fig. 4.7). Also, due to the nature of the open configuration of the reactor, species conservation analysis (e.g. carbon balance) is not possible. So that all the calculations were based on dry concentrations. Lacking the water concentration information, the total speciation is not available. However, the available speciation data analysis still reveals important reactor performance information. Further analysis requires a detailed chemistry model that is beyond the scope of this work. The non-reacting speciation distribution data agrees with our previous analysis that the mesh does not affect the axial flow field (Fig. 4.7).

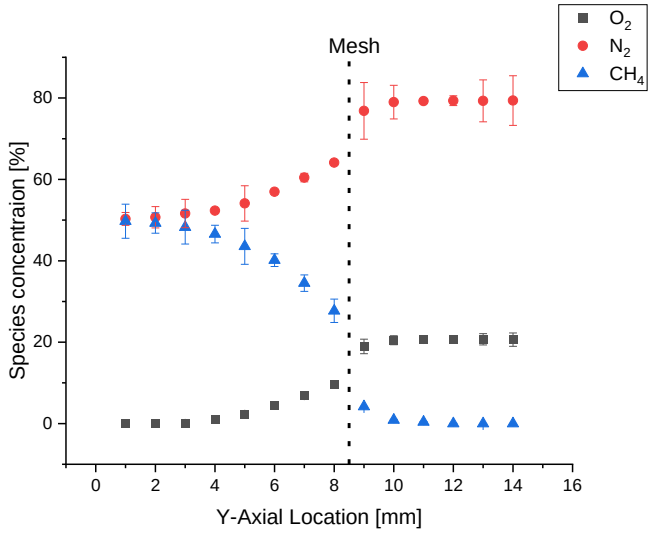

Figure 4.6 Non-reacting speciation distribution in the reactor. Fuel inlet is at 0 mm axial location; oxidizer inlet is at 14 mm axial location.

The species and temperature distribution were measured under the reacting condition (Fig. 4.8). Most reforming products are generated at the fuel side of the mesh (left side in the figure), so as the peak species concentration. Ideally the fuel should be equally distributed on both sides, while in reality the bulk flow will push the products towards the fuel side. To demonstrate, the axial flow velocity with the similarity reaction model in Cantera (Fig. 4.9) was compared. The stagnation plane is located at 5.65 mm from the fuel inlet. In the experiment, the catalytic mesh located closer to the oxidizer side where the bulk flow was towards the fuel side. Such flow behavior agrees with our hypothesis for the product peak shifting. The temperature profile had the same trend of the speciation; the highest temperature was found at the fuel side of the mesh. There is no secondary heat release peak (a second highest temperature peak) or secondary concentration peak. By the speciation and temperature measurement, it is evident that the major reaction in this reactor

happened at the catalytic mesh. The catalytic mesh worked as flame sheet like in a counter flame burner. Traditionally, counter flame burner is a great reactor of study the quenching behavior of the flame. Our reactor could also be applied to study the quenching behavior of the surface reaction in future research.

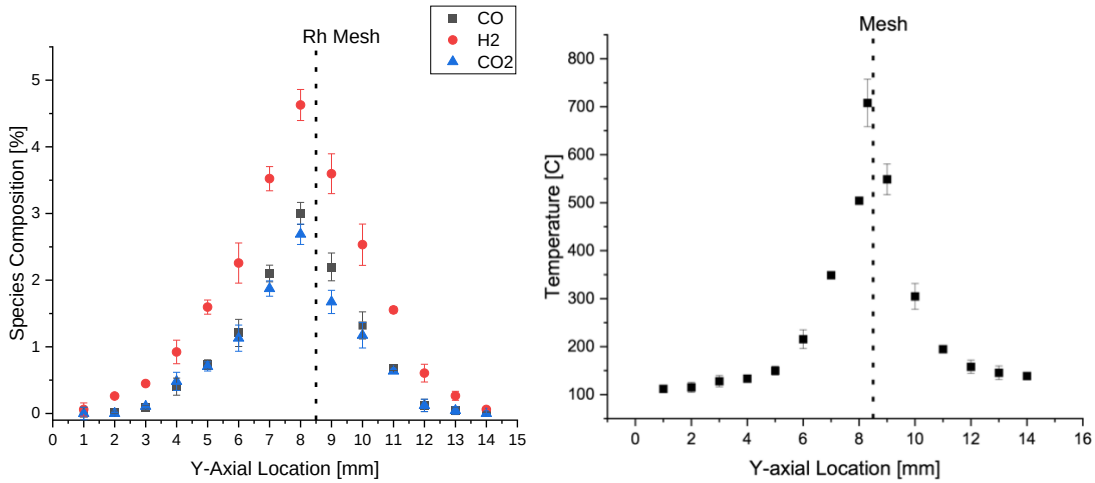

Figure 4.7 Speciation (left) and temperature (right) measurement of the reactor characterization study.

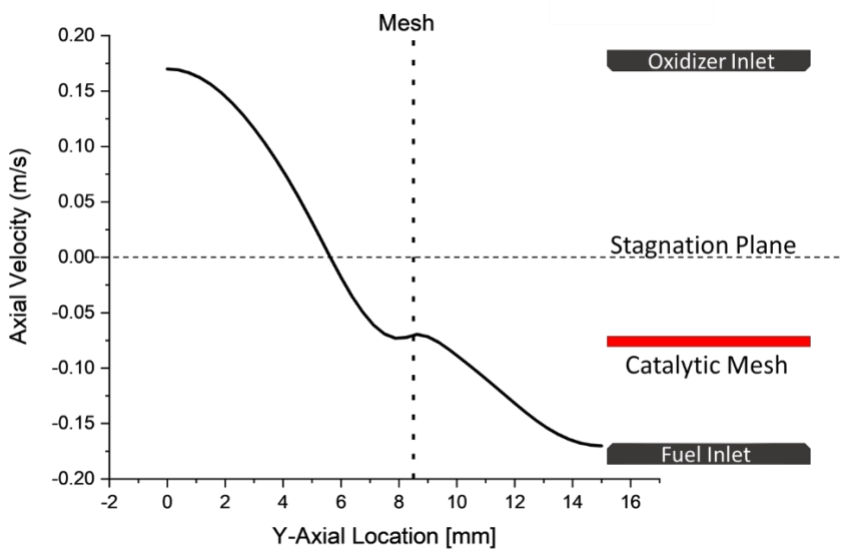

Figure 4.8 Axial flow velocity simulation with similarity model

At the species concentration peak (mesh location, Fig. 4.8), direct partial oxidation reaction model is confirmed by the co-existence of the CO, H_2 and CO_2. Decent amount of CO_2, CO and H_2 was generated in a very short residence time 0.0043 s. CO_2 concentration was found not significantly higher than CO and H_2. If the surface reaction followed the indirect partial oxidation model, CO_2 should be generated first in such case and the overall concentration of the CO_2 would be much higher than other products.

Coking and soot formation could be a major drawback of methane partial oxidation. However, counter-flow reactor enjoys the advantage of not having either of these two effects. Comparing to a traditional premixed reactor, the unique separated fuel and oxidizer inlets design of counter-flow configuration reactor helps adjusting the equivalence ratio dynamically. For example, in a fuel rich condition, the reactor usually consumes all the oxygen at the entrance section. [128-130] The high CH_4 to O_2 ratio under high temperature leads to an ethylene or soot formation. The decoupling of the fuel and oxidizer flow in the counter-flow reactor, makes it possible to better control the reaction temperature and local equivalence ratio with catalytic mesh location.

The lower soot formation in a counter-flow reactor is due to the unique axial distribution of local equivalence ratio and temperature. Generally, soot is formed by Boudouard reaction and coke is formed by ethylene generation. Ethylene is a well-documented precursor for soot formation. As shown in the equilibrium calculation of ethylene (Fig. 4.10), the darker color in the contour shows a higher ethylene formation; the white area indicates an ethylene free zone. The relationship

between local equivalence ratio and temperature is significantly different for a traditional plug flow reactor (blue squares) and our counter-flow reactor (red squares). With their different trend, the example plug flow reactor tends to run into a higher ethylene formation region (red contour) while the counter-flow reactor line barely enters the region. In a traditional plug flow reactor, the reactants are premixed before entering the reaction zone. In a rich condition, the oxidizer is consumed first and the equivalence ratio along the reaction zone becomes richer and richer with the exceed fuel and the temperature increases at the same time. This feature leads to a high equivalence ratio with high temperature condition which tends for more soot/coke formation. In counter-flow reactor, the temperature profile is independent to the species concentration profile due to the non-premix configuration. The reactants from each inlet are fed to the reaction zone separately. The high temperature only happens at the mesh location. This unique temperature profile helps avoid rich conditions at high temperature. This is the theoretical explanation the better performance of our counter-flow reactor regarding less soot/coke formation.

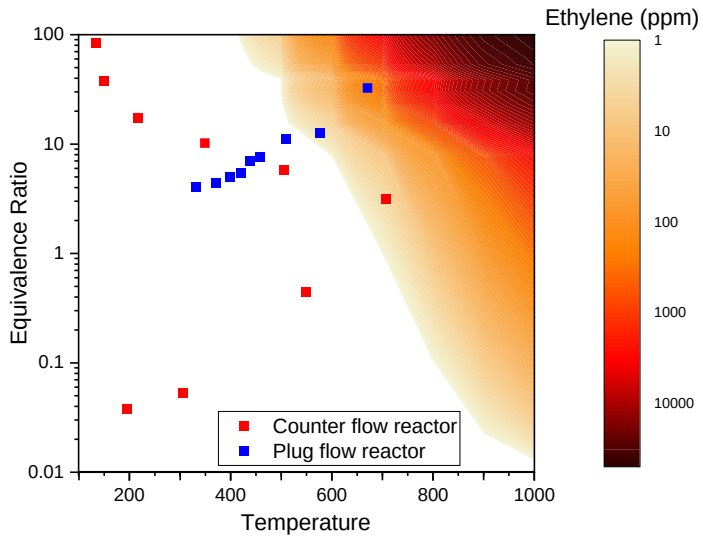

Figure 4.9 Equilibrium calculation of ethylene suggest less soot/coke formation in a counter-flow reactor than a plug flow reactor.

4.3 Conclusions

In this chapter, a counter-flow reactor for gaseous fuel was experiment studied. Our reactor is like the canonical opposed-flow reactor commonly used in flame studies but has a catalyst-coated metal mesh located between the air inlet and the fuel inlet. Experiments were conducted to evaluate both temperature and species profiles of the reactor with methane as fuel with different catalytic mesh location. In the reactor show an ability of produce the syngas without deactivation at high equivalence ratio (ϕ_{local} >3). The unique temperature gradient and local equivalence ratio avoid the reactor run into a local rich condition that generate soot and coke to deactivate the catalyst. Furthermore, the catalytic mesh functions very similar as flame in a counter flame burner. The surface reaction dominates the reaction. Also, in our study the portion of the gas phase reaction is limited due to the very short residence time. In addition, the mesh location directly controls the

local equivalence ratio which controls the reaction stoichiometry instead of the global equivalence in traditional premixed reactors.

Furthermore, the reactor flow pattern and the catalytic mesh's effect on flow were studied. In the center of the reaction zone, the mesh barely affects the flow pattern. The reaction in the center region follows the similarity model. However, in the rim of the reaction zone, the mesh alters the flow direction by a larger contact angle. The mesh works like a stagnation plane at the rim region. There is a transit region between the center and rim that the flow behaviors require further study. For the reactor characterization, due to the open deign, the speciation conservation cannot be assessed for analysis. The open design enables easy access to the reaction temperature and speciation by laser techniques (Chapter 6). It is evident that the partial oxidation reaction in the reactor follows the direct oxidation route, that the CO and H_2 are generated instantaneous with CO_2. Moreover, the decoupling of the feed fuel and oxidizer makes it possible for the reactor running into a high temperature and high equivalence ratio condition that is commonly not available by soot and coke formation. In contrast, our counter-flow design results in less catalyst deactivation for steam or dry reforming. In summary, this reactor is useful in on board application to change the fuel reactivity for gas phase fuel (Chapter 5), liquid fuel (Chapter7) and fundamental research of catalytic surface reactions (Chapter 8 future work).

Chapter 5 Application of Dual Mesh Counter-flow Reactor

This chapter experimentally evaluates our counter-flow reactor for catalytic partial oxidation (CPO) of gaseous fuels using two interstitial catalytic mesh stages. The reactor has a similar configuration as used in previous chapters but uses two catalyst-coated metal meshes located between the nozzles. The dual mesh configuration has the platinum catalytic mesh for catalytic combustion reaction that provides heat to maintain the catalytic reforming reaction with the rhodium catalyst. The idea of using the two-mesh configuration is that catalytic reforming conversion over rhodium may be improved using heat generated from the catalytic combustion over platinum. Also, this configuration could be used to study using engine exhaust-like reactants for reforming in a counter-flow reactor. Such a configuration could be similar to using reformed EGR in an on-board reactor for internal combustion engines.

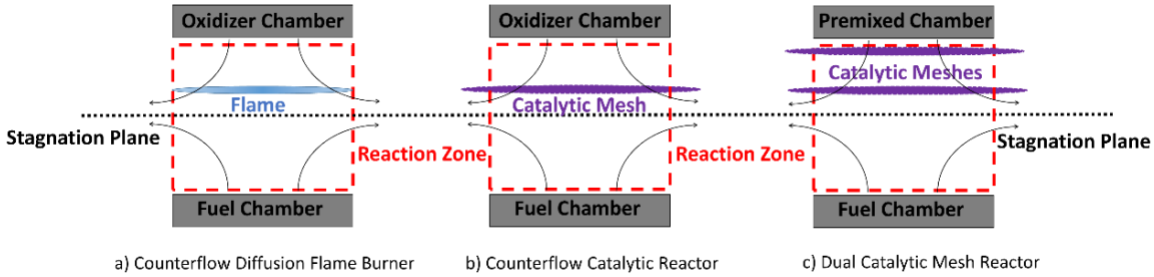

Figure 5.1. Diagram of three types of opposed flow reactor: a) counter-flow diffusion burner; b) counter-flow catalytic reactor with single mesh; and c) dual catalytic mesh opposed-flow reactor.

The reactor configuration used in the experiments is given in Figure 5.1c. In the experiment, the first catalytic mesh was used for lean oxidation with platinum as the active material. The platinum catalyst is known to result in complete combustion and can provide heat through radiation and conduction to the adjacent reforming mesh. The complete combustion products from the oxidation mesh, including mostly CO_2 and H_2O are similar to products from engine combustion and could be used to emulate the reformed-EGR scenario. The combustion products from the first mesh flow axially and adjacent to a second mesh that is meant to accomplish high-equivalence ratio CPO using rhodium as the catalytic material.

In the experiments, species profiles and temperature were measured at different catalytic mesh locations and over varying inlet flow conditions. Results from the two-mesh configuration were also compared to the previous single-mesh configuration. A CHEMKIN model was used to numerically study the products of the dual mesh reactor confirming that this configuration could advance the ignition time of the mixture. Experiments were also done to examine whether the dual mesh counter-flow reactor could convert the methane to a secondary reactivity fuel, indicating an additional potential application for engine applications.

5.1 Experimental Procedure

The dual catalytic mesh counter-flow reactor given was constructed to study non-premixed catalytic reactions and processes [131]. The reactor incorporated two circular ducts at the top and

bottom for gaseous reactants. The premixed gaseous fuel (research grade methane for this study) and oxidizer (air) was preheated to 450 °C by external electric inline heaters before entering the reaction zone. The unheated gaseous fuel (methane) was fed from the bottom chamber to the reaction zone. Two circular catalytic meshes were positioned in the reaction zone. The oxidative catalytic (platinum) mesh was set beneath the top chamber inlet and the reformative catalytic (rhodium) mesh was set between the oxidation mesh and the fuel inlet as illustrated in Figure 5.1.

The reactor was started by heating the premixed inlet to 450 °C using an inline heater and a band heater. After the catalytic mesh was preheated, the band heater was turned off and the inline heater was maintained to 450 °C by a temperature controller. The reaction could be operated at a variety of preheated temperatures after being started; and could operate without preheat when the heat source was completely turned off. However, the reaction could not be started without an elevated inlet temperature. All reported data in this experiment were obtained at 450 °C inlet temperature. Experiments were conducted at the same mesh positions and single flow condition. The bottom chamber fuel flow rate was set to 4 standard liters per minute (SLPM). The bottom chamber was a methane. The premixed flow contained 11.8% of methane, 18.5% oxygen and 69.7% nitrogen with an overall flow rate of 17 SLPM.

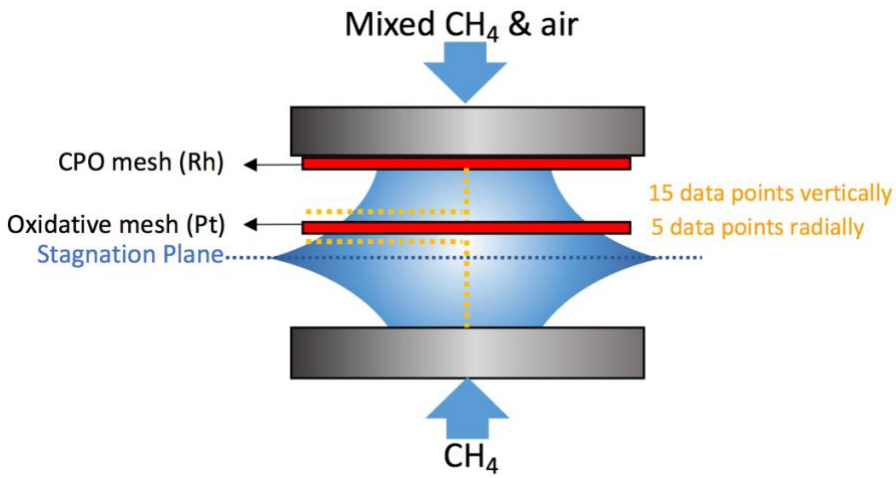

Figure 5.2. Illustration of where data was taken for dual-mesh experiments; yellow dots locate different axial and radial positions of data collection.

5.2 Results and Discussion

Temperature Profile

In the dual-mesh reactor, the catalytic partial oxidation reaction provided the majority of the heat to sustain the steam/dry reforming on the reforming mesh. In addition, an inline electrical heater heated the premixed chamber. This provided a relatively stable environment for the catalytic partial oxidation at platinum surface. In the reaction zone between the two meshes, temperature gradient was steeper than the region below the rhodium mesh (Fig. 5.3). This suggests an additional exothermic reaction occurred in this region producing extra heat. The water gas shift reaction is moderately exothermic and could be partially responsible for this heat. Further evidence for the existence of water gas shift will be discussed in following sections.

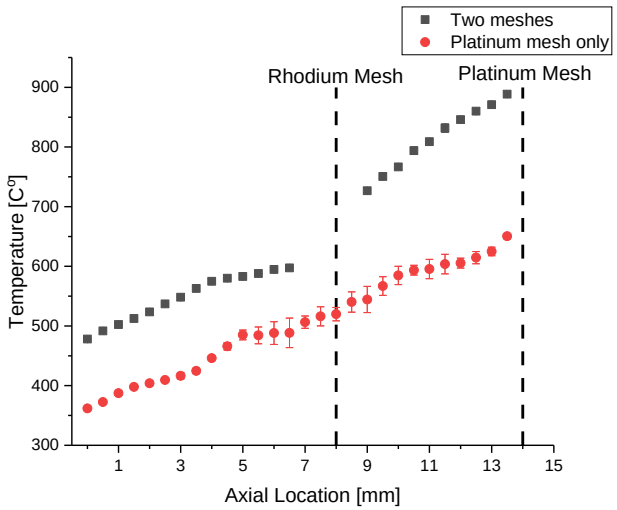

Figure 5.3 Axial centerline temperature for dual mode and single platinum mode.

Dual mesh and single mesh operation modes of this reactor were tested and compared. The single mesh mode ran at the same boundary conditions as the dual mesh mode except the top platinum catalytic mesh was removed. Dual mode showed a better performance than both rhodium or platinum single modes. In the single rhodium mode, high temperature reacting surface directly interacted with premixed fuel and air. The rhodium surface was well above 600 °C, igniting the premixed flow on the catalytic surface (Methane autoignition temperature is 537 °C at atmosphere pressure [132]). For single platinum mode, the reacting temperature was much lower than the dual mesh mode. The reaction on the platinum surface produced a limited amount of heat to sustain the reaction. The peak temperature, 891 °C for dual mesh mode and 654 °C for single platinum mesh mode, appeared at the bottom of the platinum mesh surface for both modes. This demonstrates that further catalytic partial oxidation reaction took place on the rhodium surface. As in our previous

study, a higher temperature tends to produce more synthesis gas during reforming process. This result agrees with literature for platinum short contact time reactions [133].

Axial Species Profile

The CPOx process in the counter-flow reactor resulted in similar products to those found from traditional plug flow reactors. A plug flow reactor usually proceeds through an exothermic oxidation section followed by an endothermic reforming section. The fuel converted to CO_2 and H_2O first that further reacted with steam to generate CO and H_2 [134]. The dual mesh arrangement simulates that duality but realized by two discrete, short-contact time, steps. In this study, our fuel initially converted to CO_2 and H_2O accompanied by low concentrations of CO and H_2 at the platinum mesh. These products further converted to H_2 at rhodium mesh surface by dry reforming and steam reforming. The axial speciation concentrations were measured and reported in Figure 5.4. Regions near the catalytic mesh were blocked by the ring support and thus were not accessible for sampling. The peak concentration of CO_2 was 8.6% at the closest location below the platinum mesh. At the same axial location, 2.9% of H_2 and 2.4% of CO were measured. Platinum was the short contact time oxidation catalytic that converted premixed methane and air to a mixture of carbon dioxide, water, and syngas. Limited by the speciation analysis system, water vapor measurement was impossible. However, condensed water was observed in the sample line. Between the meshes, CO_2 concentration slightly decreased towards rhodium mesh while, H_2 concentration rapidly increased. The reason is when reactants approach the rhodium mesh, dry

reforming becomes dominant. CO_2 reacts with methane at the rhodium surface that significantly consumes CO_2 and produces the hydrogen. However, CO concentration maintains constant at both sides of the rhodium mesh. This behavior may be caused by the water gas shift reaction such that the CO produced by dry reforming is consumed. Both platinum and rhodium are known to promote the water gas shift reaction converting CO and H_2O to H_2 and CO_2 [135]

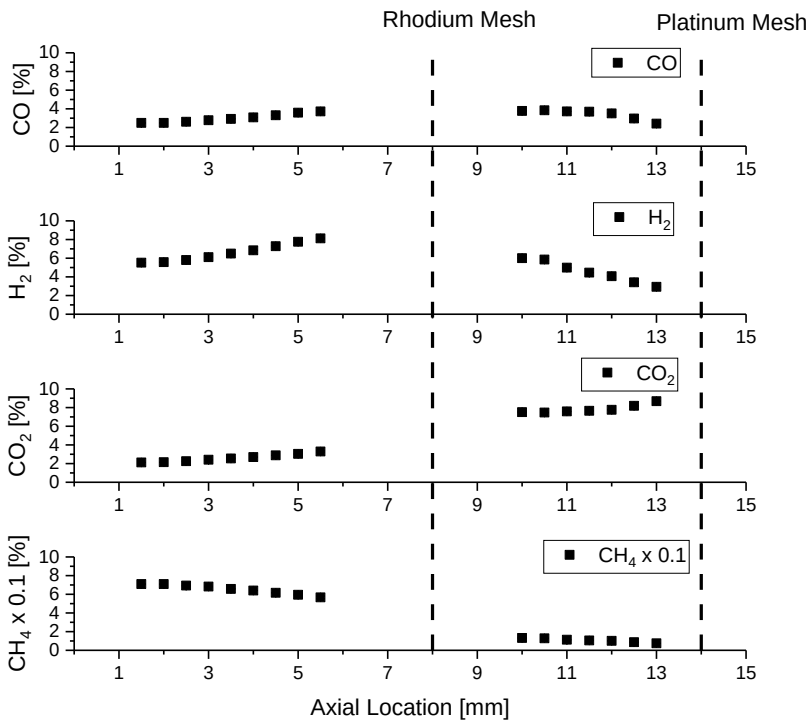

Figure 5.4. Dry mole fractions of reforming products as a function of axial distance at the centerline.

Radial Species Profile

Based on our observations, most of flow passed through the catalytic mesh while some reactants diverged from bulk flow at mesh surface and flowed radially due to the pressure drop at

the mesh surface. Radial flow across the catalyst could increase the residence time and influence product concentrations. To examine potential radial effects, the product concentrations were measured from center towards the rim of the rhodium mesh with 5 mm spacing between each measurement spot as shown in Fig. 5.5. CO concentration increased along the radius and H_2 concentration remained essentially constant. These concentration changes indicate a longer residence time for the reactant near the mesh. They also confirm that most of flow passes through the mesh; however, some of the flow diverged from bulk axial flow to the radial direction.

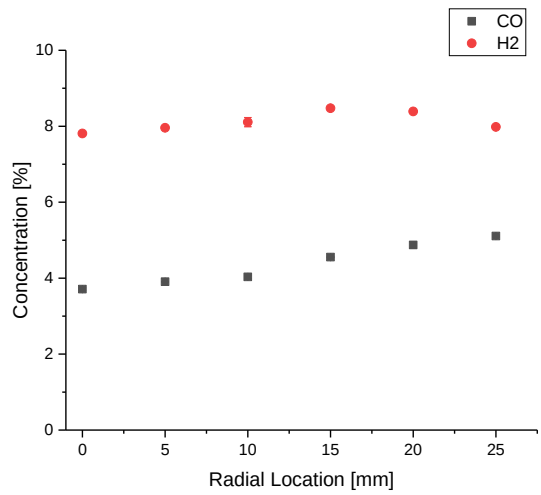

Figure 5.5. Mole fractions of reforming products as a function of radial distance.

Ignition Study of the Products

A CHEMKIN model was used to numerically study ignition delay in engine applications for the products experimentally measured in the experiments. The homogenous reactor module was used to evaluate the reactivity of a mixture of reactant by comparing ignition delay, the time from the start of the model, when the mixture ignites. The ignition delay is defined as the point at which

50% of the total heat is released from the mixture fuel. The initial condition of the model was set at 600 ˚C temperature and 1 atm pressure. The earlier the ignition, the more active the fuel. In this study, methane was set as a constant of 40% and other fuels were chosen based on the peak products generated from the dual mesh counter-flow reactor. As shown in Table 5.1, Condition 1 refers to the reactant with methane only, providing a reference reactivity. Conditions 2-5 refer to the products mixture with a proportional percentage change.

Table 5.1 Dual mesh configuration ignition study conditions

Condition	H_2 (%)	CO (%)	CO_2 (%)	CH_4 (%)	N_2 (%)
1	0	0	0	40	60
2	2	1	1	40	56
3	4	2	2	40	52
4	6	3	3	40	48
5	8	4	4	40	44

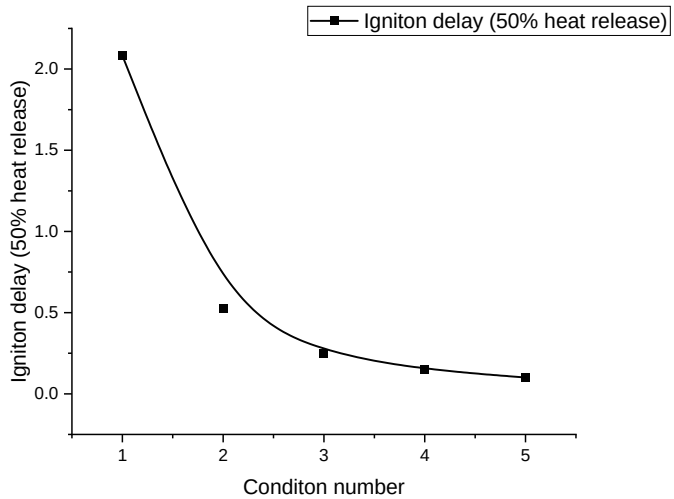

Figure 5.6 Ignition delay (50% of total heat release) under decreasing fuel conditions

Simulation results are shown in Fig. 5.6. Condition 1 has a significantly longer ignition delay than the other conditions. Comparing Conditions 2-5, the higher the syngas percentage introduced, the shorter the ignition time required. The results of this short modeling study prove that the products from the dual-mesh reactor could significant increase the ignition time in engine applications operating using autoignition.

5.3 Conclusion

In this chapter, we investigated a dual-mesh configuration for the non-premixed counter-flow reactor for gaseous fuel. This work experimentally proved the possibility of the counter-flow reactor for an on-board vehicle application. The reactor was constructed between two gas nozzles containing premixed air/fuel and pure fuel respectively. Two catalytic meshes were placed in the reaction zone, one performing oxidation and the other for reforming. Temperature and speciation data were collected and analyzed. Results show that the reactor is capable of producing similar species to a fixed bed plug flow reactor, but our reactor has a shorter contact time, specific temperature and equivalence pattern, lower probability of catalyst coking. The CHEMKIN model numerically proved that the products of the dual mesh reactor could provide products significantly advance the ignition time of the fuel. The improvement of the ignition could provide a secondary reactivity fuel for methane engines to enable high efficiency advanced combustion modes.

Chapter 6 Planar Laser-induced Fluorescence (PLIF) for Non-Contact Temperature Measurement

This chapter is focused on the laser-assisted temperature measurement method development for use in the counter-flow gas phase reactor. This non-contact technique provides a more accurate thermometer free from disturbances that plague commonly used intrusive sampling methods. As shown in Fig. 6.1 (left), when inserting a thermocouple or a sampling probe in the reaction zone of the counter-flow reactor, the flow condition is affected. In this way, the unpredictable change of local equivalence ratio change directly affects the surface reaction (Fig. 6.1 (right)) and the reported data are incorrect. In meeting the need to measure the temperature without disturbing the reaction conditions, an innovative laser-assisted thermometer is developed and calibrated for the reactor in this chapter. This system is based on the dual-band toluene planar laser-induced fluorescence (PLIF). The 2-D temperature mapping acquired by the new system is validated and compared to thermocouple measurement. This work confirms the feasibility of the non-contact thermometer idea and shows its distinct advantage over traditional thermocouple method.

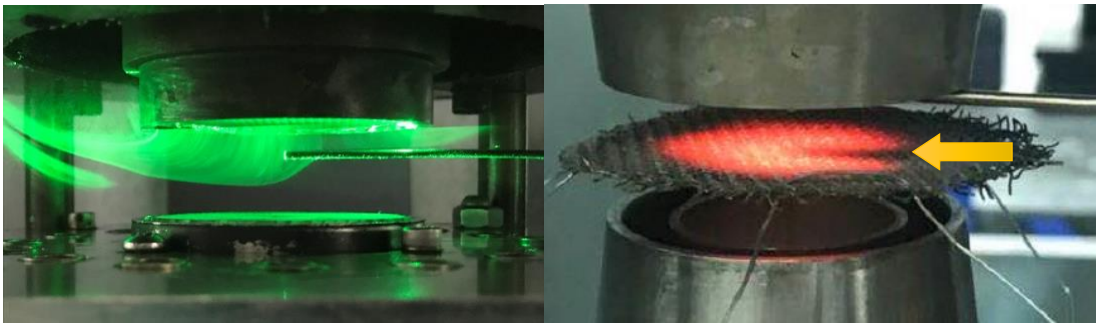

Figure 6.1 The flow condition (left) and surface reaction (right) are affected by an intrusive measurement/sampling method.

6.1 Experimental Procedure

The single catalytic mesh counter-flow reactor introduced in Chapter 4 was selected for the laser-assisted thermometer development (Fig.6.2). Air was chosen as the oxidizer and methane was the fuel in this study. The distance between the two gas manifolds was 12 mm. The flow rate was set 9 standard liters per minute (SLPM) for air and 6 SLPM for methane. Platinum catalytic mesh was used. Three different mesh locations were tested: 4.5, 5.5 and 6.5 mm form the fuel outlet. The temperature profiles were measured axially in 4 different locations: reactor center, and 2, 5, 10 mm from the center. Since the gas phase temperature in the reaction zone was very high, the inserted thermocouple underwent thermal radiation heat loss to the environment. Such heat loss is highly dependent on the thermocouple surface area. The true temperature (i.e. infinitesimally thick thermocouple measurement) was calculated with the 2 measured temperatures by thermocouples in two different diameters: 1 mm and 1.5 mm. Planar laser-induced fluorescence (PLIF) was used for instantaneous and non-intrusive temperature measurement. Toluene was selected as the tracer since it meets the temperature region of this study. A Nd:YAG laser with a maximum output 120

mJ/pulse at 266 nm generated the excitation laser pulse. The laser beam was expanded by light-sheet optics into a 12 mm sheet. The excited fluorescence signal was recorded by an intensified CCD camera through a BG280 band-pass filter (FWHM=10nm) and a 305 long pass filter respectively (Table 6.1). The oxidizer and fuel flow were doped with 5% (volume) toluene allowing for an adequate fluorescence signal level without significantly altering fuel characteristics. Toluene is delivered using a syringe pump into the reactor from both top and bottom inlets. An ICCD camera was used to record the image. To minimize the effect by response of camera, both images were taken simultaneously with the same camera with an image splitter. The toluene detection limit of the system is estimated to be 600 ppm. The image splitter would induce distortion and registration to the image; however, this is not complicated to eliminate by image processing comparing to the error caused by camera response.

Table 6.1 Filter and Camera Specifications

Filter	Filter	“Red”	“Blue”
	Filter Type	305 nm long pass	280 nm band pass
ICCD Camera	Manufacturer	Andor	
	Model	Istar DH334T	
	Resolution	1024 x 1024 pixel	
	Pixel Size	13 x 13 μm	

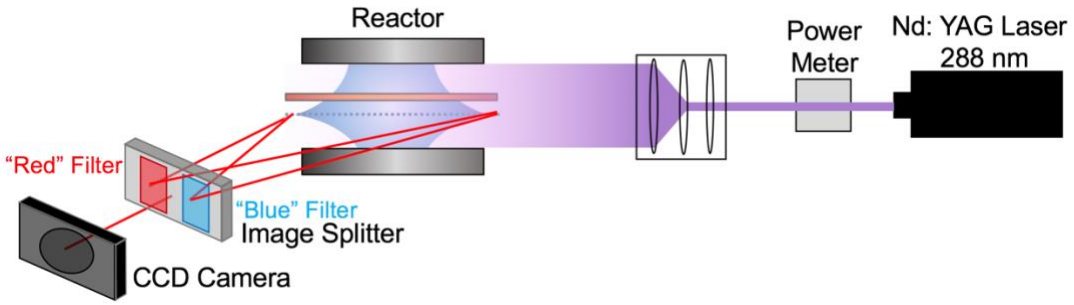

Figure 6.2 Experimetal setup diagram

6.2 Image Processing

The two-band PLIF thermometer requires taking the ratio with the two images. The difficulties include very low signal intensity and the interference from environment lighting. The main task of image processing is to remove noise. The image process scheme is shown in Figure 6.3. All the images were processed with MATLAB. The process functions were from MATLAB's basic library and Mathworks file exchange which is a share community [136].

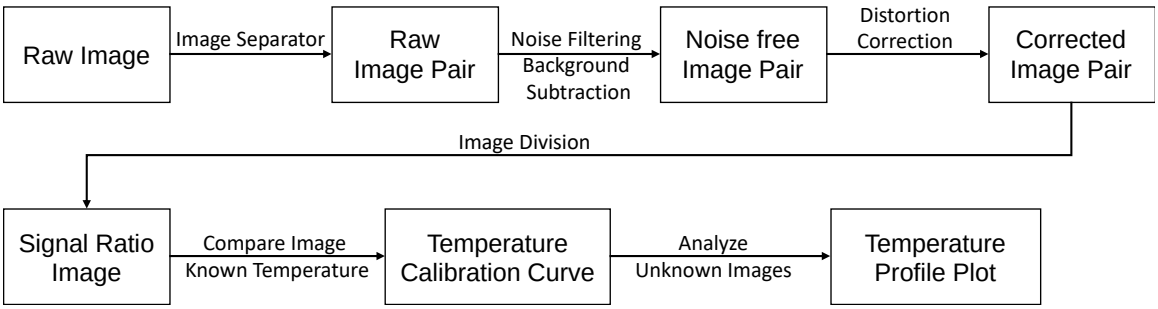

Figure 6.3 Non-contact PLIF thermometer image processing scheme.

Image Separation and Distortion Correction

Typically, in the two-band toluene PLIF experiment, two images are taken by separate ICCD cameras. Such setup would induce two issues: first, the two images would be slightly misaligned

by the different positioning of the two cameras; and the differences in ICCD camera sensors and setup would bring in equipment error. The first issue usually requires after-processing to align the two images on the same optical axis. The second problem requires an image restoration process. With the one-camera setup in our system, the two issues were avoided. Still, there was image misalignment caused by the image splitter, but its effect was limited by a carefully chosen camera location and facing direction. Moreover, since all images were taken by the same ICCD sensor, the registration process was not necessary. Instead, the raw image was processed through a separation process based on the chess board calibration. The custom-made chess board picture has 8 × 8 write-black rectangles, each sized 2 × 2 cm (Fig. 6.4).

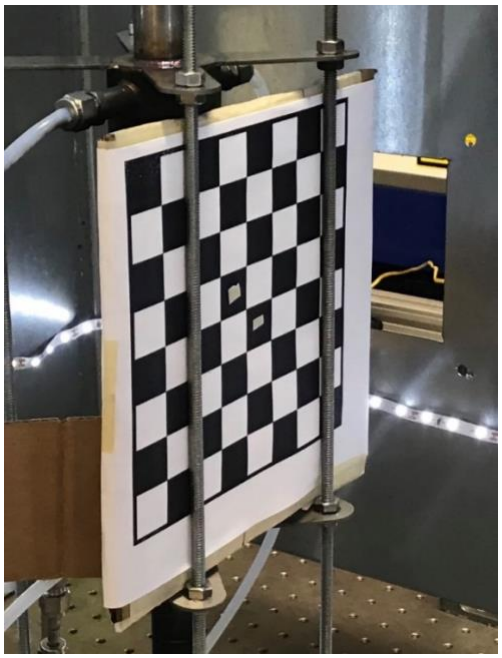

Figure 6.4 Calibration chess board picture placed at the reactor position.

The picture was place at the reactor position with two marks for the reaction zone. A series of images were taken (Fig.6.5). In the raw image (Fig. 6.5(A)), the two images were overlapped and stretched. After correction the “red” and “blue” filtered images were captured (Fig. 6.5 (B)(C)). The deformation in the images was adjusted by process function and manually in MATLAB, including Matlab calibration toolbox(http://www.vision.caltech.edu/bouguetj/calib_doc/) for distortion correction and MATLAB basic function for image separation. These processing steps were recorded and reproduced to correct the temperature measurement images.

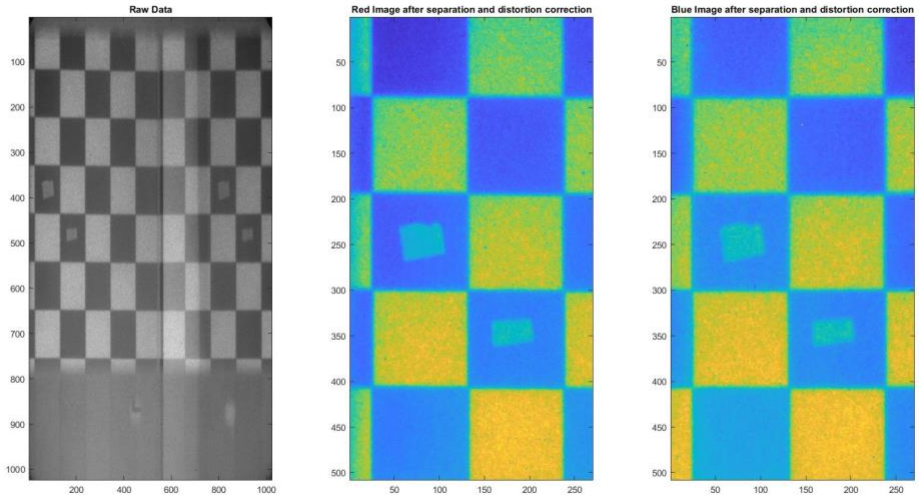

(A) (B) (C)

Figure 6.5 Chess board picture calibration.
(A) Raw image and separated images for (B) the “red” filter and (C) the “blue” filter.

Noise Filtering

Beyond the image correction procedure, it is important to filter the noise caused by multiple sources. First, the ICCD camera noise should be removed (Fig. 6.6). This noise is not uniform and

could cause large errors upon image processing. The process function to smooth the ICCD camera noise was found from MATLAB file exchange [137]. Comparing to weight average filtering and Gaussian filtering, this function keeps the most details of the image, does not change the intensity of the signal, and performs better in eliminating the noise's effect to the following processing steps. All the images, including the background were processed by this filter before other steps.

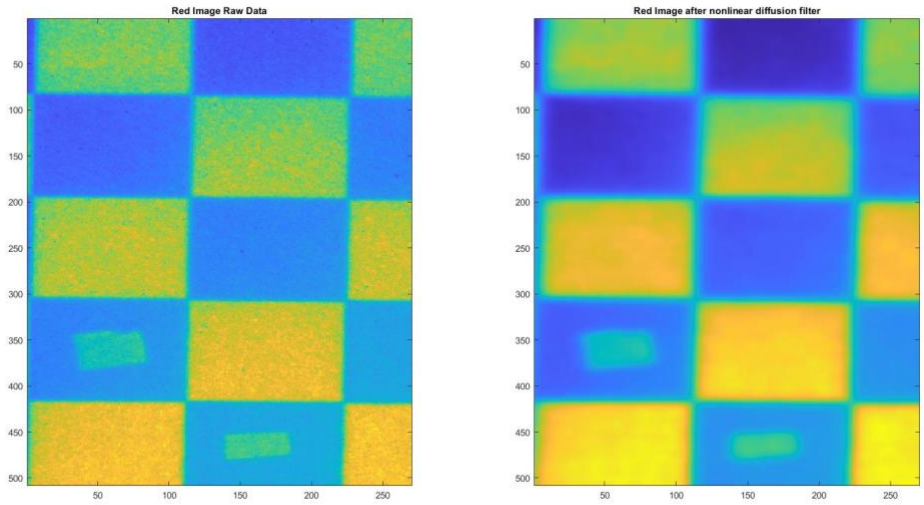

Before After

Figure 6.6 ICCD camera noise smoothing function.

Since the toluene PLIF signals were weak in this system, the background signal generated by the environment light could also affect the temperature measurement. Therefore, the second step is to subtract the background images from the measurement images. The background images were taken after the PLIF measurement but had no toluene doped in the flow. This step greatly reduces the influence by the environment and laser scattering (Fig. 6.7). It can be seen that scattered light by the reactor and exhaust, and the light generated by the catalytic mesh are the sources of

background signal. After subtracting the background, the division of the two images was taken as the thermometer signal.

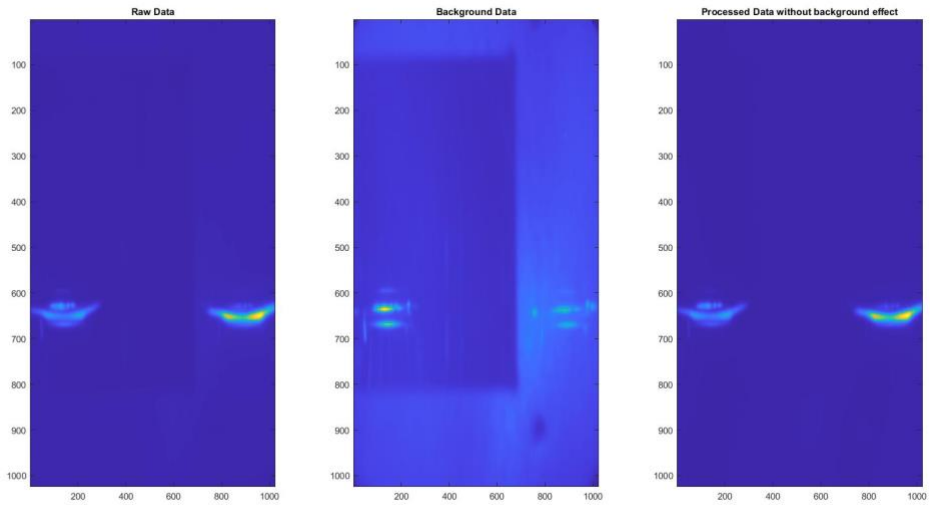

(A) (B) (C)

Figure 6.7 Background subtracting step is taken before the division of the two images. (A) Raw images, (B) Background images and (C) Final images.

6.3 Results and Discussion

Temperature Calibration

As introduced in Chapter 2, the signal of the PLIF thermometer is only dependent on temperature but is not possible to convert to temperature directly (Eq. 2.12). Before applying the thermometer for any measurement, it requires to calibrated by a constant temperature cell (Fig. 6.8). To perform the calibration, the constant temperature cell was fed with pure N_2 and heated by an in-line heater. The temperature measured by the PLIF thermometer was validated by thermocouple measurement. The thickness of the thermocouple introduces error to temperature measurement due

to radiation heat loss. To minimize this effect, two thermocouples of different diameters were used to calculate the true temperature by an infinitesimal diameter thermocouple.

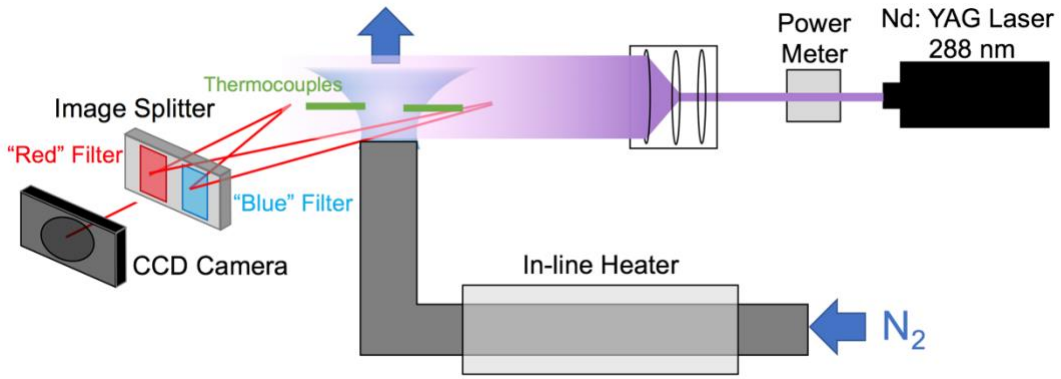

Figure 6.8 Constant temperature cell calibration setup.

By fixing the temperature in the calibration system, a whole range fluorescence signal ratio-temperature calibration curve was generated. The signal ratio by dividing the two images exponentially decreases with the temperature as Fig. 6.9. In our experiment, the signal ratio is trending to 1 at approximate 525 ˚C, the maximum measurable temperature by our thermometer system since anything higher would result in non-distinguishable images by the two filters (signal ratio = 1). The fitting equation of this calibration curve will be used to generate the contour temperature plot for the counter-flow reactor.

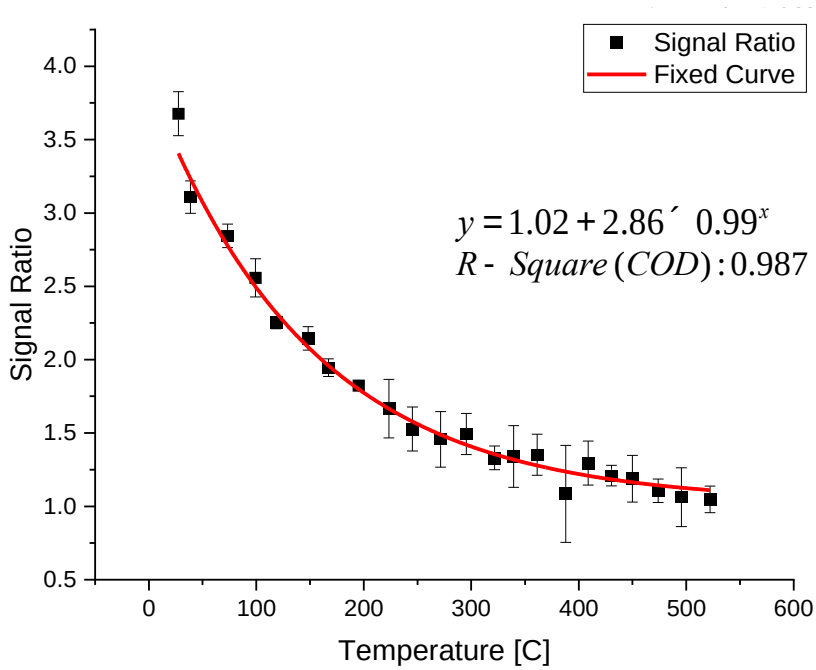

Figure 6.9 Fluorescence signal ratio-temperature calibration curve

A rising trend of the signal-error ratio is observed with rising temperature (Fig. 6.10). Below 200 ˚C, the signal-to-error ratio is about 5%. Between 200 ˚C and 525 ˚C, the ratio rises to 10% ±5%. In Fig. 6.9, we can see the signal ratio has an almost consistent error 0.1 – 0.2 in the whole measurable temperature range. Such error is likely caused by the camera itself. When the temperature gets higher, the signal ratio value decreases, which rises the share of the error resulting in a higher signal-error ratio. For example, at the maximum measurable temperature, 525 ˚C, a 0.1 signal ratio error would cause 66 ˚C error. The average signal ratio obtained through ten measurements was used to establish the desired calibration curve.

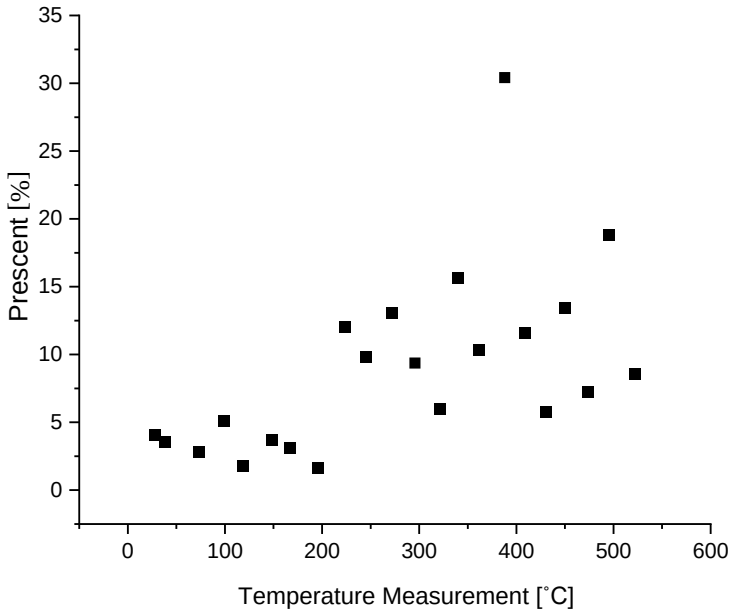

Figure 6.10 Signal-error ratio plot shows the percentage of measurement error in the signal ratio.

Using the upper and lower measured value in the experiment, it was found that the maximum error was 41 ˚C at 525 ˚C using the PLIF system. If errors of reference thermocouples, which also rises with temperature due to thermal radiation, are taken into account, this maximum error increases to 71 ˚C by standard error propagation analysis. The error propagation analysis of the whole measurable range is plotted in Fig. 6.11. Between 100 – 450 ˚C, the mostly used range in this experiment, the propagated error is less than 50˚C.

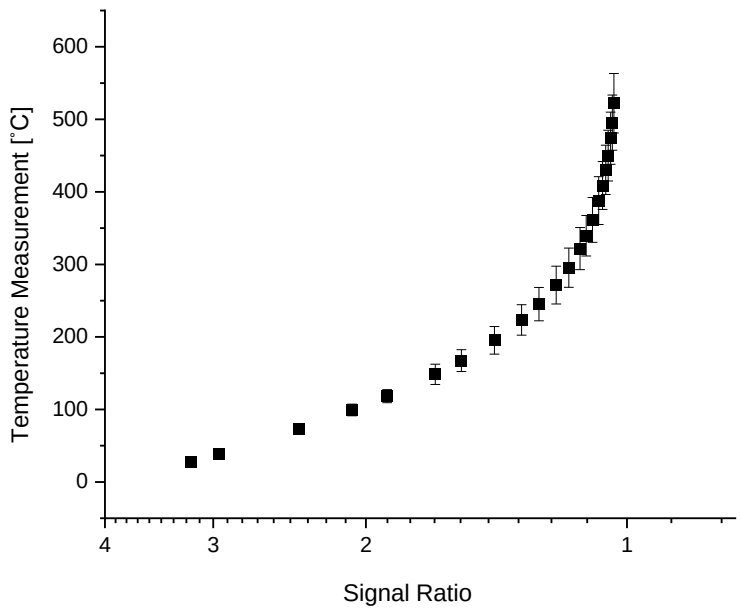

Figure 6.11 Temperature error propagation analysis with the PLIF thermometer signal

Temperature Measurement Results in the Counter-flow Reactor

With the calibration curve, we are able to map the temperature field in the counter-flow reactor using the PLIF thermometer. Three different conditions were tested with low, medium and high catalytic mesh positions (Table 6.2). Among them, the reaction in Condition 1 is the weakest self-sustained condition. This condition demonstrates the lowest interference by the catalytic mesh to the temperature measurement.

Table 6.2 Experimental Conditions for PLIF Thermometer in the Counter-flow Reactor

Condition	Mesh Position above Fuel Outlet (mm)	Fuel Flow Rate	Oxidizer Flow Rate	Catalyst
1	4.5	6	9	Pt
2	5.5	6	9	Pt
3	6.5	6	9	Pt

The temperature field in the reactor is measured by the PLIF thermometer and compared with thermocouple results for the three conditions (Fig. 6.12). As expected, the thermocouple measurement in the reactor showed larger error in both high and low temperature regions, indicating that the thermocouple thickness correction for thermal radiation is insufficient. In Condition 3, with higher surface reaction at the catalytic mesh, the thermocouple-measured temperature is lower than the PLIF thermometer measurement because the thickness correction for thermal radiation is not sufficient. All of the thermocouple measured outlet temperatures are lower than those taken by the PLIF thermometer. Although the thermal radiation at outlets is lower than the catalytic mesh, the higher flow rate there would induce more convection heat transfer from the thermocouple, which contributes to the error for the temperature measurement at this region. This temperature deviation at outlet was observed even in the lowest reaction and temperature condition (Condition 1).

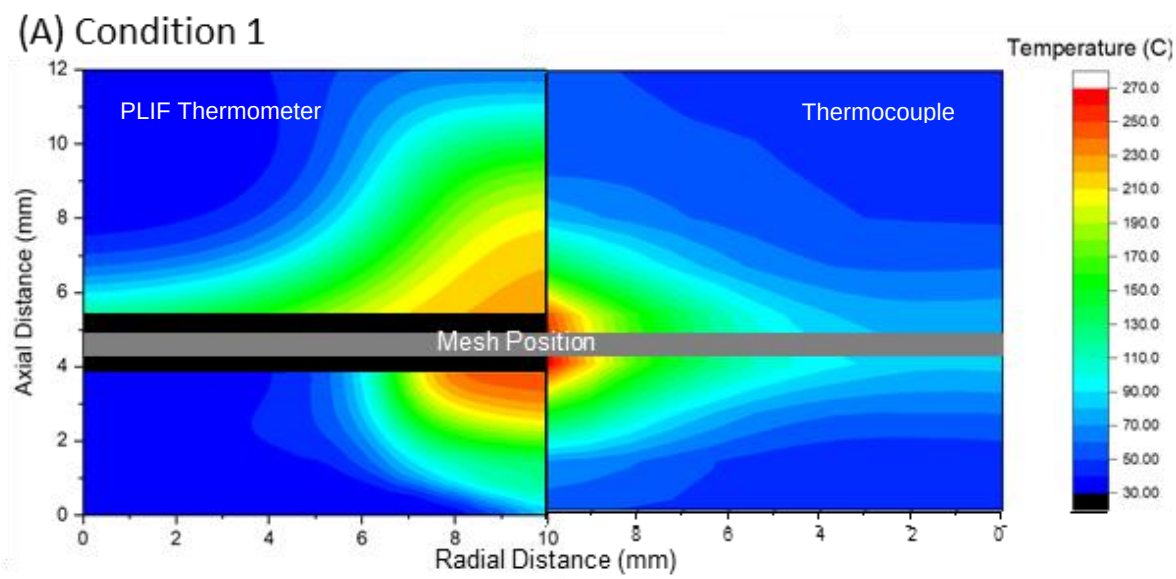

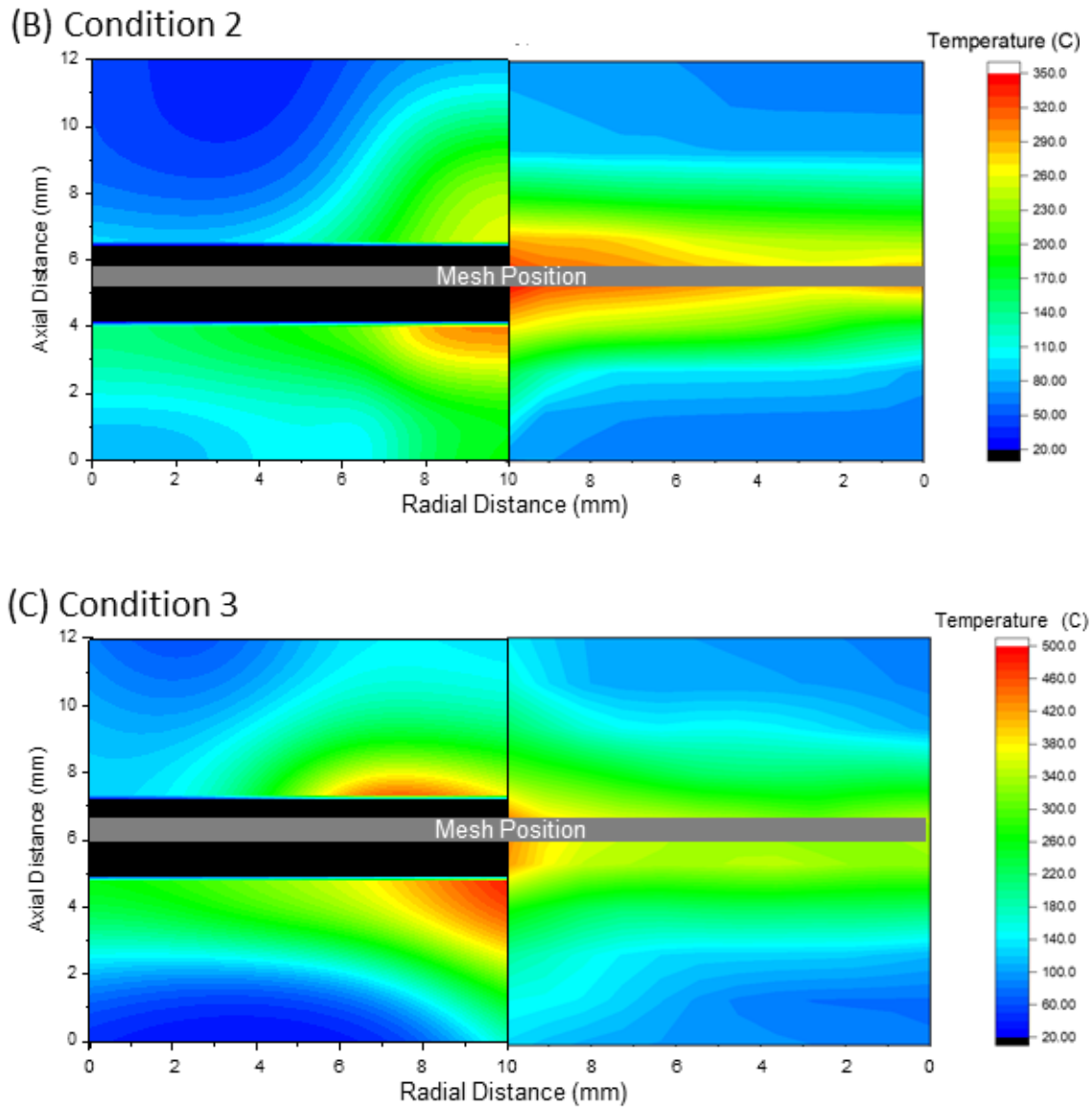

Figure 6.12 2-D temperature contour plot of the counter-flow reactor by PLIF thermometer and thermocouple for the three conditions.

In Figure 6.12, three conditions of PLIF thermometer shows the same trend but more clearly as the thermocouple that the temperature at the catalytic mesh lower surface is slightly higher than its upper surface based on the gas flow. However, it is intuitive that a stronger reaction should result in a larger high temperature region near the mesh. For example, Condition 3 should show a larger

high temperature region than Condition 1, which is obvious in PLIF thermometer contour plot but vague for thermocouple plot.

The top part of the plot in Condition 3 is slightly left-shifted from the reactor axis, mainly because the reaction temperature in this condition (up to 500 ˚C) gets very close to our maximum measurable temperature (525 ˚C), such that the error is the largest compared to other parts of the plot and other conditions. Moreover, since the surface reaction in Condition 3 is the strongest, the mesh glow also interfered with the measurement more prominently than in the other two conditions. By contrast, the contour plots of Condition 1 and 2 are more symmetric. The catalytic mesh glow also conceals the temperature signal, together with the toluene autoignition (at 480 ˚C) glowing near the mesh, resulting a non-measurable region. The range of the non-measurable region is smallest (1.8 mm thickness include mesh) for Condition 1 where the surface reaction is the weakest. In contrast, the non-measurable regions in Condition 2 and 3 are 2.3 mm.

6.4 Conclusion

In this chapter, a toluene PLIF thermometer is developed, calibrated and demonstrated for the counter-flow reactor. We compared the 2-D temperature field in the reactor measured by the thermometer with thermocouple measurements. Compare to thermocouples, our PLIF thermometer enjoys the advantages of non-intrusive measurement, higher spatial resolution, and more precise results. Moreover, the radiation and convection heat loss induce prominent errors in thermocouple

temperature measurement of counter-flow catalytic reaction which is very difficult to correct. The thickness correction for thermocouple thermal radiation applied in our study turned out to be insufficient. The impact of intrusive sampling should not be overlooked, given the importance of local reaction conditions (e.g. local equivalence ratio). Limited by the equipment availability in our lab, our laser is not strong enough to access the measurement close to the reaction surface. The temperature measurement range of the thermometer is also constrained by the consumption of toluene. However, this toluene PLIF thermometer provides a new possibility for non-intrusive measurement that leading to the potential application of this counter-flow reactor in fundamental studies.

Chapter 7 Hydrocarbon CPO_X with Atomization Reactor

As an extension of the counter-flow reactor in Chapter 4, this section discusses a special design for liquid fuel catalytic partial oxidation. Liquid fuels have better portability than gaseous fuels and higher energy density but are more difficult for th counter-flow configuration due to the requirement for vaporization. In this chapter, ethanol is chosen as the example fuel for a novel reactive volatilization reactor. In the reactor fuel atomizer is used in place of the gaseous fuel jet. The atomizer could enhance fuel evaporation and transport through the porous catalyst. The fuel is directly sprayed onto the hot catalytic material surface and undergoes evaporation and surface reaction. Though its design is inherited from the gas phase reactor in Chapter 4, the reactor used in this chapter was a separate apparatus. It is expected that this reactor configuration could be used for various liquid fuel application with minimal necessary modification. In this part, the reactor shows stable generation of syngas by ethanol autothermal reforming. The reaction pathway in the reactor is also discussed. Furthermore, the reactor model is also proposed at the end of this chapter.

We also investigate the principle of the counter-flow configuration to reduce the soot formation on catalyst. Ethylene as a precursor of coke formation that coke the catalyst is well documented in other studies.[138] The counter-flow configuration has a benefit of avoiding locally high C/O ratios running into the high ethylene generation region to reduce the possibility of catalyst

poisoning. The main objective of this work is to characterize the ethanol reactor and its performance in reducing soot formation.

7.1 Experimental Procedure

To study liquid fuel catalytic partial oxidation, a new atomization counter-flow reactor was built. This reactor is designed similar as the previous gas phase reactor with only the gaseous fuel jet replaced by a fuel atomizer for liquid fuel vaporization and mass transfer into the porous catalyst. With the two counter-flow reactors, we would be able to study the differences between gas and liquid phase reactions in future studies. Droplet evaporation occurs in the gas reaction zone as well as on the catalytic mesh akin to a reactive flash volatilization. To fit this liquid fuel, a fuel atomizer is set as fuel outlet. The fuel was directly injected onto the hot surface of the catalytic material where it was vaporized and converted catalytically to products. With the atomizer, the fuel flow rate through the reaction zone could be accurately controlled by using a negative feedback loop (Fig.7.1).

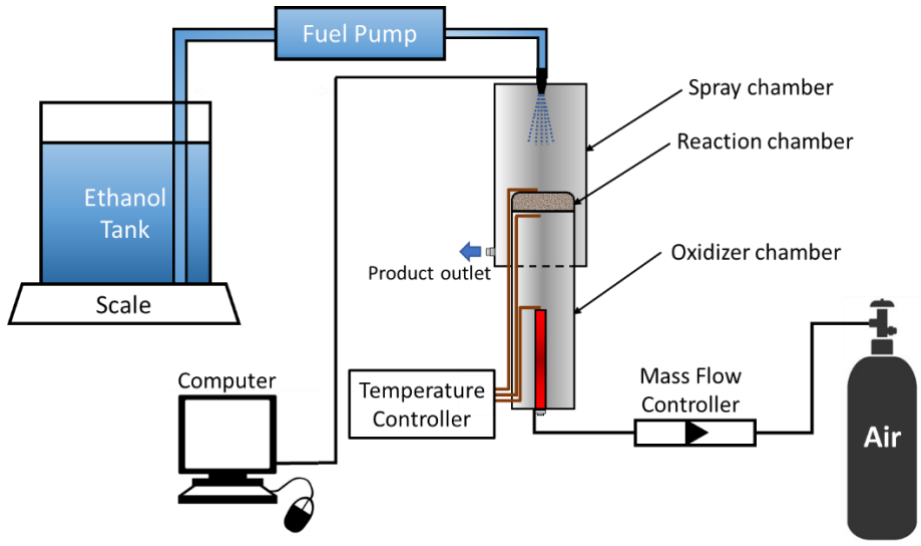

Figure 7.1 Schematic diagram for atomazation reactor

Experiments were conducted for three types of liquid fuel: pure ethanol, hydrated ethanol (150 prof) and E85. The fuels were pressurized to 50-70 PSI prior to injection. A National Instruments Driver Module was used to control the fuel atomizer. The driver module included a Compact RIO module for driving a Port Fuel Injectors model that directly controls the atomizer. A flow test was taken to determine the fuel flow rate associated with the injection frequency with each fuel type. A scale was used to monitor the real-time fuel tank weight during experiment by monitoring the change in weight of the tank throughout the experiments. All the flow rates reported in the experimental results are mean flow rates averaged over 2 min. A pressure gage was used to confirm the fuel atomization pressure during test.

As shown in Fig. 7.1 the reactor consists three parts: fuel system, oxidizer system and sampling system. The flow rate of the fuel system was controlled by measuring the fuel tank weight with a LabVIEW program. The oxidizer flow came from the bottom of the reactor. Air was used

as oxidizer and an Alicat mass flow controller was used to control the flow rate. An inline heater in the flow system was designed for the ignition. The reactor could was self-sustained after ignition and run into steady state condition in about 20 min, but a low heating rate was applied to ensure reaction stability. For the sampling system, a K-type thermocouple was inserted into the top surface of the catalyst to monitor the reaction temperature. Errors in temperature measurement were not believed to be significant because the reactor operated at a relatively low temperature with low radiation heat transfer. Since the reactant concentrations near the rear of the catalytic mesh were sufficiently low, it was expected the catalytic reactions at the thermocouple position could be neglected. Radial temperature change in the thermocouples was also negligible due to its small diameter. Heat transfer balance for the thermocouples was calculated based on a previously published study [139]. It shows that the maximum T error was within 10 °C assuming 0.14 emissivity (ε) of the K-type thermocouple (non-oxidized nickel). This emissivity estimation would normally introduce an uncertainty to flame temperature measurement. Gas sample was taken from the exhaust of the reactor. For some conditions, additional gas sample was taken from the top and the bottom surfaces of the catalyst for further analysis. A Raman laser gas analyzer (RLGA) system (Atmosphere Recovery Inc., Model RLGA-1800L-BF) was used to measure lighter reaction products (e.g. hydrogen, carbon monoxide *etc*.). The RLGA only measured total hydrocarbon concentration and could not provide detailed speciation of individual hydrocarbons. Therefore, a micro-GC system (Inficon Micro GC) with two columns (Plot Q and Molsieve) was used to

measure reaction products concentration. A customized gas sampling system was implemented for products measurement and storage in a stainless reservoir for future RLGA and micro GC analysis. The injection rate was 200 mL/min for RLGA and about 50 mL per run for micro GC. The samples were chilled to condense water vapor before the RLGA and Micro GC systems. A N_2 balance calculation was done to correct dry concentrations to wet concentrations in this study.

Experimental Conditions

A full range of experiments using the three fuels were completed. Concepts explored include comparing the effect of equivalence ratio, atomization pressure and fuel type. Catalytic conversion and selectivity chosen as the characteristic parameters of the reactor. The atomization distance was the only factor on the wet region surface area on the catalyst which defines the best performance of the reactor. All the experiments were conducted with the front surface of the catalyst in full contact with the atomization spray, and air flow was kept same at 30 SLPM and were thus not included in any parametric experiments. All experimental conditions are listed in Table 7.1 below. Condition 1 is used in studying the effect of atomization pressure; Conditions 2-4 were used for exploring how different fuels behave in the reactor under various C/O ratios.

Table 7.1 Liquid fuel reactor characterization conditions

Condition	Fuel	C/O Ratio	Atomization Pressure
1	Hydrous Ethanol	1.20-1.24	50, 55, 60, 65, 70
2	E85	0.68, 0.78, 0.97, 1.12, 1.27	60
3	Pure Ethanol	0.59, 0.83, 0.89, 0.97, 1.07	60
4	Hydrous Ethanol	0.59, 0.82, 1.06, 1.11, 1.22	60

To start the experiment, airflow was set to 30 SPLM and the heater was set at 300 ˚C. After the heater reached the preset temperature, the fuel atomizer system started to atomize the fuel and impinge it onto the catalyst surface. After ignition, the heater was turned off and reset to 100 ˚C. The system reached steady state in approximately 15-20 min. Then three gas samples were taken from the exhaust of the reactor and three more were taken from the top and bottom surfaces of the catalyst for each configuration. All samples were analyzed by RLGA and micro GC. Temperature data and fuel tank weight were measured continuously during the experiments.

7.2 Results and Discussion

Definitions for Calculation

C/O Ratio and Equivalence Ratio – The C/O ratio and equivalence ratio are the different expressions describing the fuel and oxidizer ratio. Molar C/O ratio (Eq. 7.1) is preferred by the chemical engineering community while equivalence ratio (Eq. 7.2) is widely used in combustion and engine field. In this case, ethanol (A/F)s is chosen as the complete combustion air to fuel ratio 8.95. In this section, the C/O ratio is applied in analysis instead of equivalence ratio because three different fuels were used and needed to be compared, including complex mixtures like E85. Equivalence ratio varies with fuel type, causing complications in making comparisons. For example, the iso-octane in E85 fuel has a different A/F_{stoic} than the other two ethanol fuels, making the rich and lean conditions of E85 differ from the other two fuels.

$$\frac{\mathrm{C}}{\mathrm{O}} = \frac{2n\left(\mathrm{Ethanol}\right)}{n\left(\mathrm{Ethanol}\right) + 2n\left(\mathrm{O_2}\right)} \tag{7.1}$$

$$f = \frac{\left(A/F\right)_{\mathrm{stoic}}}{\left(A/F\right)} = \frac{\left(F/A\right)}{\left(F/A\right)_{\mathrm{stoic}}} \tag{7.2}$$

Conversion and Selectivity – Conversion rate describes the rate of reactant converted (Eq. 7.3). Selectivity describes the ratio of desired product to unwanted products generated (Eq. 7.4). Conversion and selectivity are commonly used to evaluate a reactor used for creating a desired product. Reforming efficiency (Eq. 7.6) gives a thermodynamic view of the energy consumption of the reactor. It represents how much energy is used to maintain the reaction versus how much chemical energy remains in the products.

$$\text{Ethanol Conversion (\%)} = \frac{\text{mole of Ethanol input} - \text{mole of Ethanol output}}{\text{mole of Ethanol input}} \times 100\% \tag{7.3}$$

$$\text{CO selectivity (\%)} = \frac{\text{mole of CO produced}}{2 \times \text{mole of Ethanol converted}} \times 100\% \tag{7.4}$$

$$\mathrm{H_2}\text{ selectivity (\%)} = \frac{\text{mole of } \mathrm{H_2} \text{ produced}}{3 \times \text{mole of Ethanol converted}} \times 100\% \tag{7.5}$$

$$\text{Reforming Efficiency (\%)} = \frac{(\mathrm{LHV_{CO}} + \mathrm{LHV_{H_2}} + \mathrm{LHV_{CH_4}} + \mathrm{LHV_{C_2H_4}} + \mathrm{LHV_{Ethanol}})_{\mathrm{out}}}{(\mathrm{LHV_{Ethanol}})_{\mathrm{in}}} \times 100\% \tag{7.6}$$

Effect of Atomization Pressure to the Atomizer

Different atomization pressures were tested to investigate the effect of the pressure on the catalytic reaction (Table 7.1 Condition 1). A higher pressure will provide a larger atomization field angle and smaller droplets. When the pressure is lower than 50 PSI, it is not possible to ignite under

the current temperature settings. Five different pressures were tested with adjusted atomization frequency for each case to ensure a consistent fuel flow rate.

Fig. 7.2 shows the conversion and reforming efficiencies. It is apparent that no condition ran at complete conversion (converts all oxidizer/ fuel). Ethanol conversion increased from 20% to 30% by increasing the atomization pressure. Due to the pump limit and safety, the highest pressure was set to 70 PSI. Higher pressure gives a finer droplet size that has a better chance to flow through the catalyst to the other side. On the other hand, the reforming efficiency (presented by the red dots in Fig. 7.2) decreases as pressure increases. This is primarily due to the tradeoff between conversion and reforming efficiency. A higher fuel conversion leads to more fuel consumption during the reaction. Due to the nature of the exothermic CPOx reaction, a higher conversion would decrease the total heating value of the products and reduce the fuel reforming efficiency. The higher conversion through increasing the pressure also lead to a more complete reaction so that more CO_2 was produced than CO in higher-pressure cases. Consequently, reforming efficiencies became lower for such cases. Another observation is the H_2 selectivity increasement plateaued at high atomization pressure. This could be caused by the faster evaporation of smaller droplets that reduces the residence time. CO selectivity and H_2 selectivity are shown in Fig. 7.3. Considering carbon-based selectivity, the CO selectivity is between 7% to 15%, indicating most carbon species converted to CO_2 releasing heat to maintain the reaction. The rest of carbon species mainly converted to methane. Moreover, more carbon loss was observed for higher atomization pressure.

There are two possible reasons: unburned ethanol condensed during the sampling process; acetaldehyde (CH_3CHO) products were not measured. This hypothesis could be answered by considering the steam reforming pathway of ethanol over Rh/Al_2O_3 catalyst [140]. One ethanol molecule undergoes dehydrogenation reaction to generate one acetaldehyde which further converts to methane through decarboxylation. The high portion of methane could be an evidence of acetaldehyde.

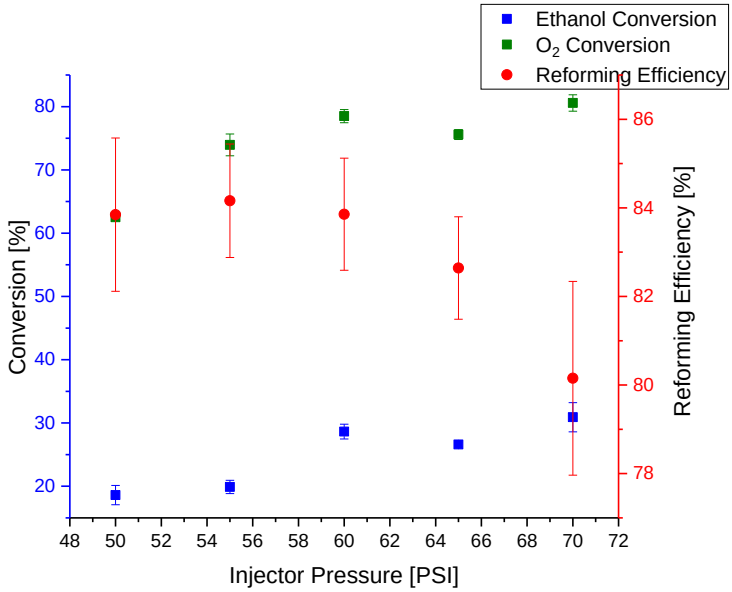

Figure 7.2 Conversion and reforming efficiency under different pressure

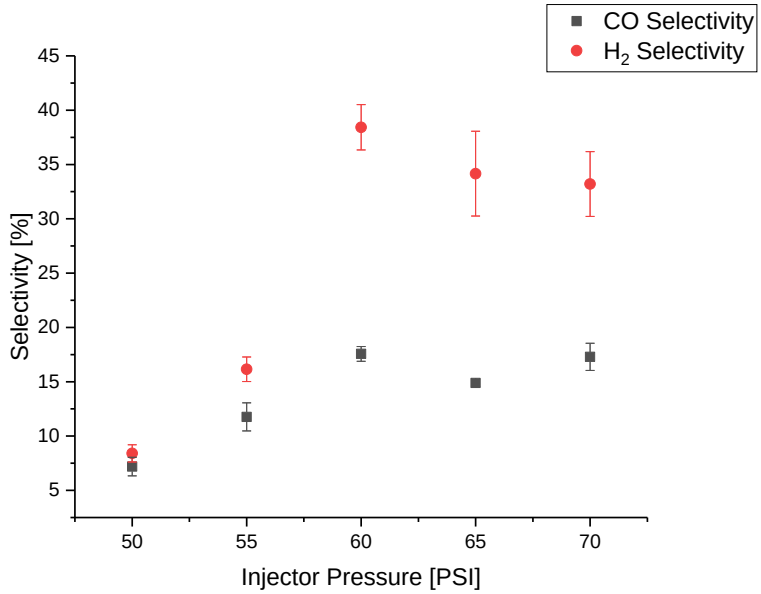

Figure 7.3 Reaction selectivity of ethanol reactor

Effect of fuel Type and C/O Ratio

In this section, the atomization pressure was fixed at 60 PSI. E85, pure ethanol and 150 proof ethanol are compared with different C/O ratios. The reactor showed stable syngas generation by ethanol autothermal reforming. The reaction pathway in the reactor is also discussed. Furthermore, the reactor model is proposed at the end of this chapter. Due to atomization controlled by spray frequency, the fuel flow rate was unable to be controlled precisely. The C/O ratios were set as close to the target C/O ratio as possible.

Temperature Effect – The reaction temperature of E85 was found to be overall higher than the other two fuels. Its highest reaction temperature is 479 ˚C at C/O ratio about 1. Ideally, the peak temperature tends to be observed in lean condition, where catalytic combustion is more preferred with more heat released by complete oxidation than partial oxidation. However, in this reactor, the

lean condition showed a very low reaction rate. The global C/O ratio also affects the fuel diffusion that further impact the residence time.

Multiple factors together determined the peak temperature for E85. Ethanol showed 50-100 ˚C lower temperature than E85. This is due to the higher heating value of the E85 than ethanol. The iso-octane contained in the E85 increases its heating value to 29.34 MJ/kg than 26.7 MJ/kg of pure ethanol. Over the tested range, hydrous ethanol showed the lowest reaction temperature, 213 ˚C. This is due to the higher water content in hydrous ethanol that requires more heat for fuel evaporation. Also, the higher water content yields more steam reforming which changes the reaction model and further lowers the reaction temperature by its endothermic nature. The low reaction temperature also has a risk to form coke to deactivate the catalyst. More detail discussed in later section. Furthermore, the hydrous ethanol reaction temperature trends shifted to the higher C/O ratio comparing to the other two fuels. For the C/O range measured, the hydrous ethanol had not reached the best performance.

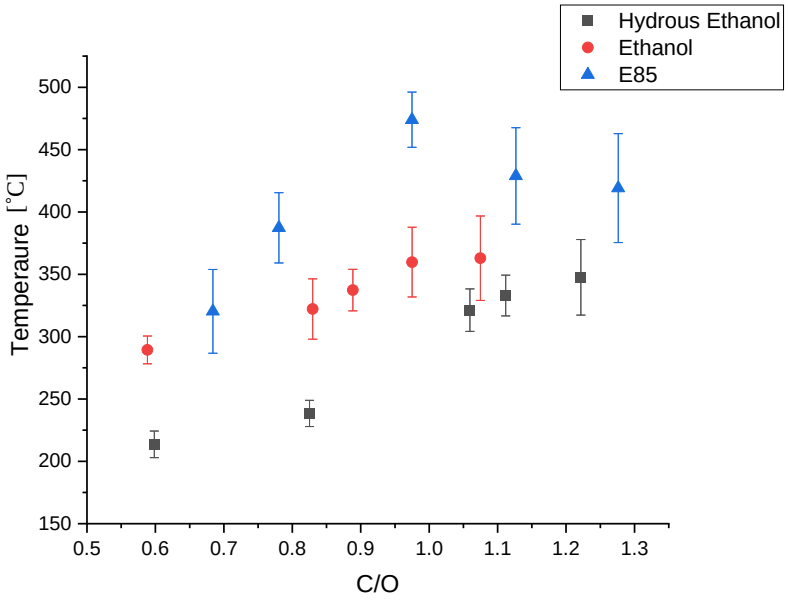

Figure 7.4 Reaction temperature for different ethanol reltive fuel under vary C/O ratio

Conversion – Ethanol fuel showed the highest conversion among all types of fuels. Its conversion maintained at about 45% and the started to decrease above C/O ratio approximately equal to 1. Similarly, E85 had a peak ethanol conversion of about 35% and its ethanol conversion decreased when C/O ratio raised above 1. This higher ethanol conversion was due to higher heat demand to maintain higher fuel evaporation rate that induce a more complete autothermal reforming reaction.

Since the heating value of ethanol is lower, more fuel is required to maintain the reaction. However, the low heating value alone cannot explain the lower conversion of E85. The reaction model of mixture fuels is quite different from, and much more complicated than, that for single component fuels. For E85, its ethanol portion evaporates faster and leaves an iso-octane core flowing in the catalyst foam. This unique feature results in dual stoichiometric planes. More amount

of light hydrocarbon and radicals are formed during the iso-octane reforming process that competes with the ethanol dissociation in the catalytic surface. For all C/O ratios, ethanol conversion was always higher than iso-octane (Fig. 7.5 (C)). This agrees with the results of Diehm *et al*. where ethanol and iso-octane was combined in different ratios and ethanol always showed a higher conversion than the iso-octane [141].

There are three major reasons for higher conversion for the ethanol experiments. First, ethanol initially forms an ethoxy species by adsorbing through a lone pair of oxygen atom [142], while the iso-octane starts by physiosorbed on the catalytic surface and decomposition the weakest C-H bound. [143]. This case the ethanol has a better molar flux due to its better diffusion. Second, there is evidence from other studies [79-82] that Al_2O_3 plays an important role in the ethanol reforming process but has a more limited effect on iso-octane reforming. The third reason is that the differences in the branched structure of iso-octane and ethanol might also play a role.

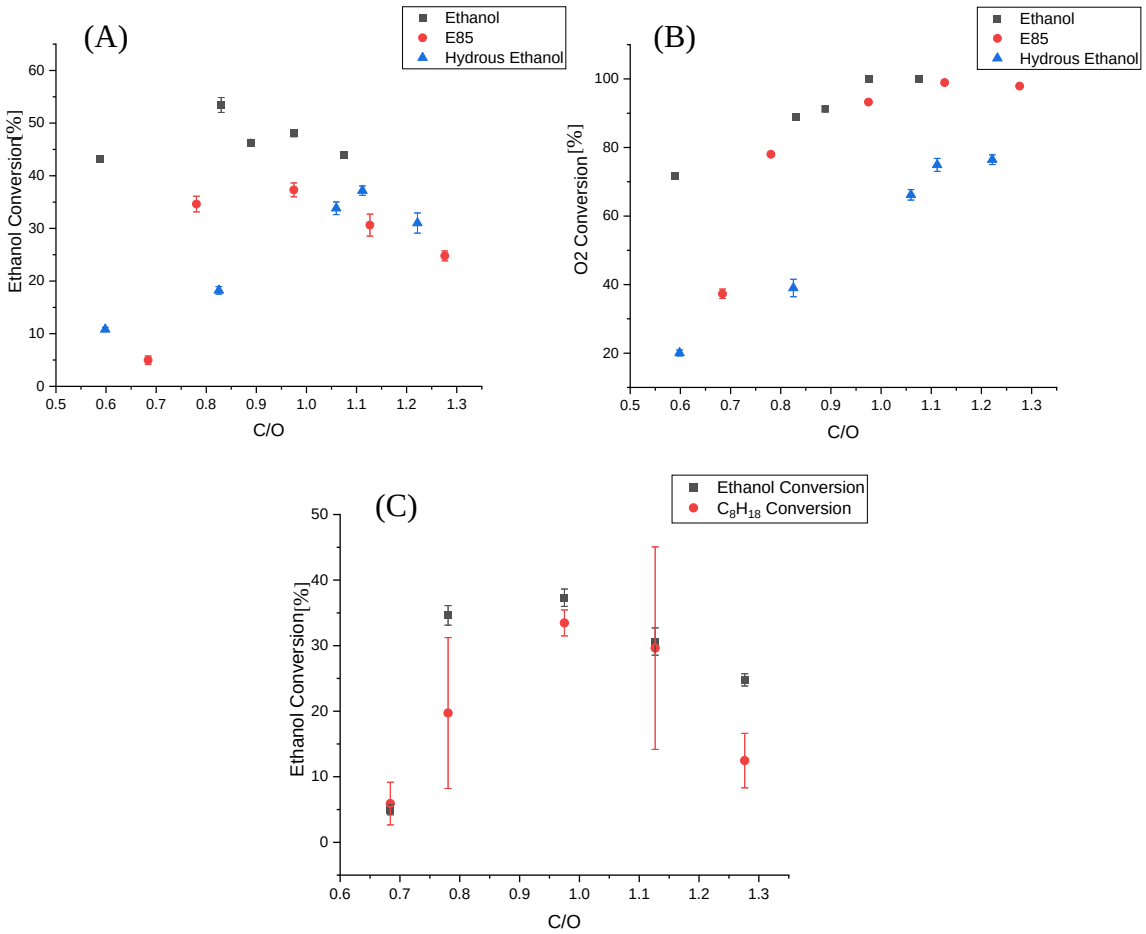

Figure 7.5 Fuel converson under different C/O ratios

As mentioned before, the water content in the hydrous ethanol makes the whole reaction more yield to steam reforming. This is also confirmed by the lower oxygen conversion in the reaction. As shown in Fig. 7.5(B), oxygen conversion of pure ethanol and E85 reached 100% around C/O=0.95, while the hydrous ethanol did not. Another observation is the difference in the lower ignition limit between ethanol and E85 (0.58 vs 0.68). With this reactor, E85 required a higher C/O ratio to self-sustain the reaction. One reason is the atomization property that the evaporation temperature of iso-octane (99 ˚C) is higher than ethanol (78.4 ˚C). This makes the droplet size

larger when reaching the catalytic surface which further helps the fuel's diffusion into the reaction zone. Furthermore, the mixture of iso-octane and ethanol for E85 induces a multilayer of the stoichiometry or the micro explosion of the droplet, an idea that will be discussed later.

In general, premixed reactors, like plug flow reactors, [144] have a higher ethanol conversion in most lean conditions and lower ethanol conversion at a higher C/O ratio. However, the counter-flow configuration works differently. The conversion increases to a peak value and decreases as the C/O ratio further increases. The reason for this is, for a traditional plug flow reactor, the residence time is fixed. The major parameter is C/O ratio alone. Other studies show that a short residence time will decrease ethanol conversion. [145] In our case, the change in the C/O ratio changes the residence time, too. There is no way to fix the residence time in our reactor. The air and the fuel flow rates will control the evaporation rate and the diffusion depth of fuel into the catalyst. Therefore, the residence time and the C/O ratio are coupled in this case. A lower fuel flow rate will result in faster evaporation of fuel, which gives a short residence time. A peak conversion condition is found that is determined by the combination of the residence time and C/O ratio. For this reactor, the optimal point is manipulated to be C/O=1 since it is ideal for partial oxidation. A more delicate adjustment of the catalytic structure might further improve the reaction performance, but this is beyond the propose of this study. More importantly, the local equivalence ratio may provide a chance to explore the reaction model for this reactor. This will be discussed in the later section.

Syngas and CO_2 Speciation – In Fig. 7.6, comparing between the different fuels, the ethanol has higher hydrogen production for all C/O ratio. This is because of the existence of the iso-octane in E85 that lowers the overall H_2 selectivity. Also, the H_2 selectivity decreases with increasing C/O ratio. Due to the longer carbon branched structure, more carbon-related products are produced by E85 than for pure ethanol. Comparing the results of pure ethanol and hydrous ethanol, the trend of hydrogen concentration is similar. The H_2 concentration increases with the C/O ratio. The peak hydrogen production is at C/O=1.22 for hydrous ethanol. The higher water content in hydrous ethanol leads to a steam reforming dominated reaction, that gives a higher hydrogen production. On the other side, all data fall into a linear region, the ethanol has a slightly higher selectivity at low C/O ratio, however, as mentioned before, the hydrous ethanol reaction region shifts to the higher C/O ratio by the reaction model. Overall, our H_2 production is lower than most plug flow reactors, which is not only due to the low conversion of the fuel but also the reaction temperature. In a plug flow reactor, the peak H_2 production is around C/O = 0.73, but in this reactor the peak concentration is right shifted to C/O ~ 1.15.

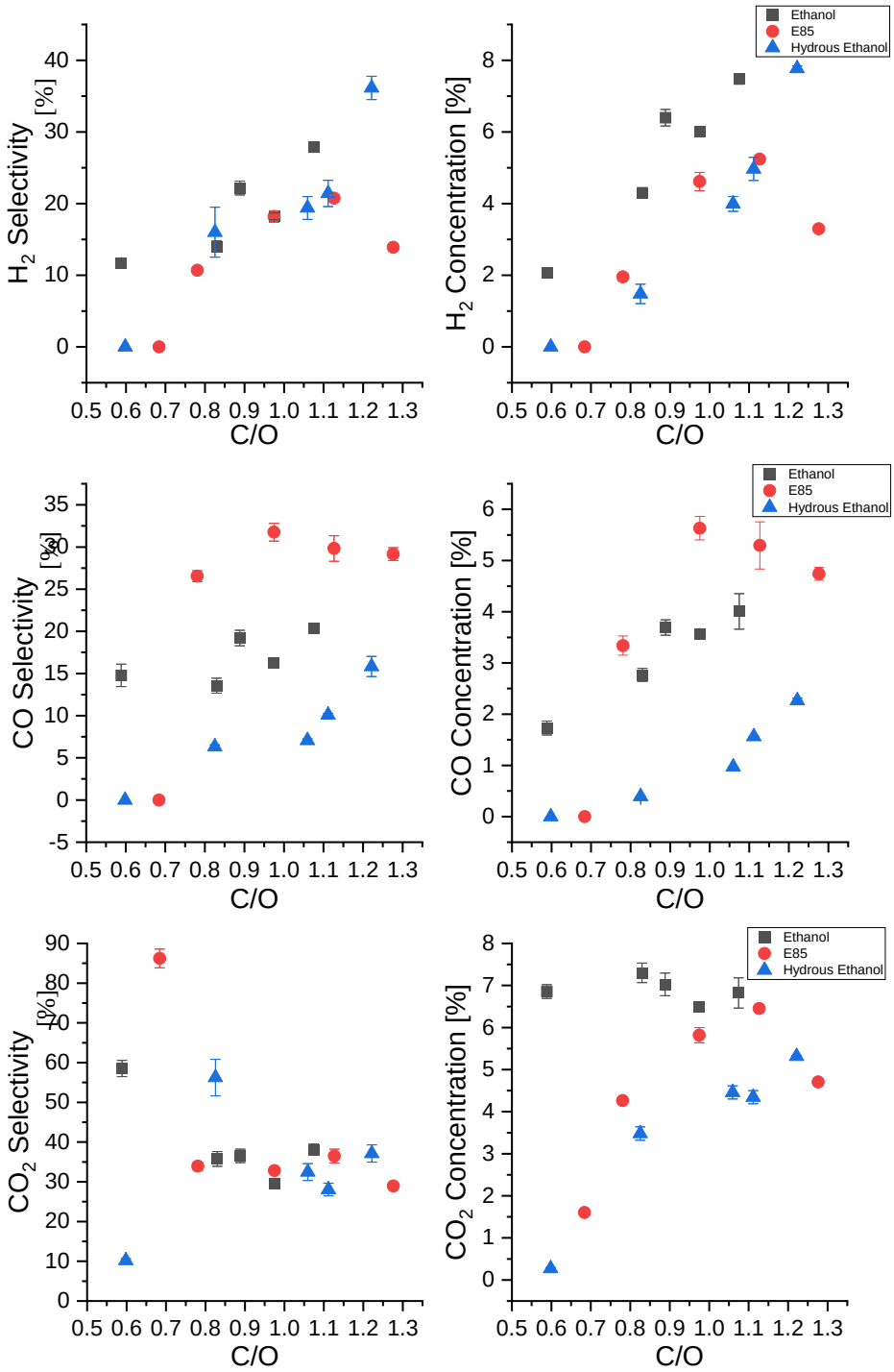

Figure 7.6 Major product selectivity and product concentration for different C/O ratios

In spite of lower H_2 selectivity E85 has a significantly higher CO selectivity and product concentration. Hydrous ethanol CO production is much lower than other fuels as expected. Pure

ethanol has the highest CO_2 production than all other fuels by its lower heat value. Comparing to pure ethanol, E85 has a higher heating value and its heat release relies not only on CO conversion. However, hydrous ethanol has a very low CO_2 production due to the different reaction pathway (Fig. 7.5 and Fig. 7.6). Steam reforming dominates the reaction that limits the CO and CO_2 production. For selectivity, CO_2 almost stays constant at about 35% under high C/O ratios. This is because of the limited amount of the O_2 in the reaction. At C/O above 0.9, the O_2 conversion reaches 100%, that no more O_2 is left over in the reaction. The CO_2 production change for this range could only be caused by the water gas shift which is limited in such low temperature. Again, this agrees with our point that the global C/O ratio is not a good indicator for reaction performance. The local C/O ratio at a given location should reveal more information of the reaction in the case of the non-premixed reactor.

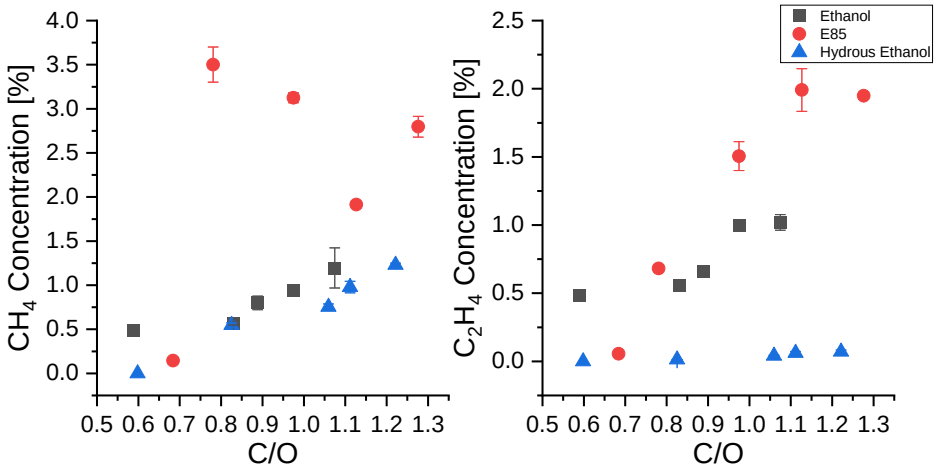

Figure 7.7 Methane and ethylene product concentraiton under different C/O ratio

Methane and ethylene are important intermediate species that can help determine the dominant reaction pathway in the reactor. This could further help figuring out the major source and possible

solutions of soot formation. In our reactor, the methane and ethylene production of E85 is almost always much higher than the other two fuels (except C/O=0.68, due to the very low conversion). In spite of C/O=0.68, methane generation of E85 is about 3% and it decreases when C/O increases while ethylene generation of E85 increases with C/O ratio. In this case, E85 needs to be discussed separately. The higher generation of the intermediate species is caused by the partial oxidation of the iso-octane. Iso-octane tends to generate more lower hydrocarbons during partial oxidation due to its long carbon structure. In general, rich mixture hydrocarbon partial oxidation produces more lower hydrocarbon due to the limited oxygen. However, for the case of E85, methane generation acts in the opposite way, indicating the existence of further reactions of methane. The higher amount of CO as shown in earlier discussion could be produced by such further reactions. Due to the existence of the iso-octane the light hydrocarbon generation lead to some soot/coke formation. As shown in Fig. 7.7, pure ethanol and hydrous ethanol have a different trend; they have very close methane production which increases almost linearly with C/O ratio. However, when considering ethylene, hydrous ethanol almost has no ethylene production while pure ethanol has increasing amount of ethylene along with the C/O ratio. Based on this observation, the major reaction route is ethanol dehydrogenation to acetaldehyde and then the acetaldehyde further goes through decomposition to methane and carbon monoxide. The methane generates carbon dioxide and hydrogen by steam reforming. Additionally, water gas shift and reverse water gas shift reactions further affect the carbon dioxide, carbon monoxide, water and hydrogen concentrations. On the

other hand, there are two hypotheses for the low ethylene concentrations by hydrous ethanol: first, the water portion of the fuel reacts with ethylene for syngas reducing the ethylene concentration and increasing the useful products. Another possibility is that ethylene forms coke by polymerization that deactivates catalyst. However, H_2 and CO production of hydrous ethanol is lower than pure ethanol. In addition, the carbon loss for hydrous ethanol is slightly higher than pure ethanol. However, the deactivation did not happen in the pure ethanol case (Fig. 7.8).

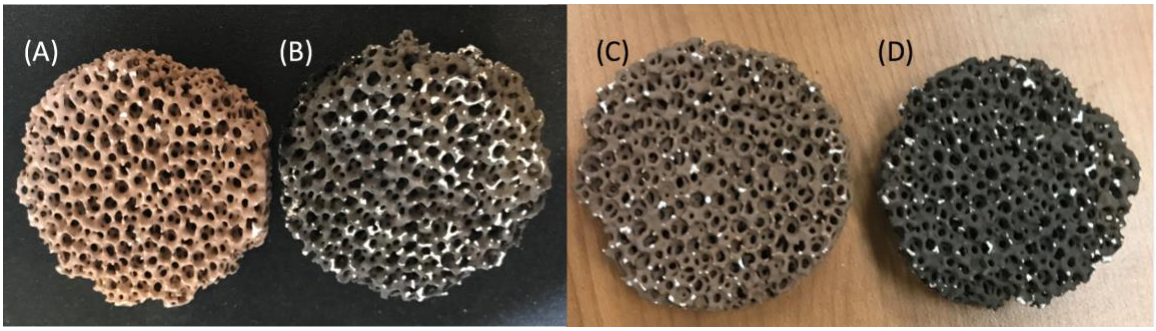

Figure 7.8 Soot formation on catalyst
(A) New catalyst, (B) E85, (C) Ethanol, (D) Hydrous ethanol

While the detailed explanation would be covered in the model discussed later, there is no CPOx at the lower catalyst surface with the hydrous ethanol fuel. Therefore, ethylene is produced on Al_2O_3 that cannot be consumed rapidly and forms coke. Differently, CPOx happens at the whole catalyst for ethanol, so the ethylene is consumed. The amount of coke by E85 is between ethanol and hydrous ethanol (Fig. 7.8(B)) since iso-octane generates light hydrocarbons, which is quite different than the other two fuels. In summary, a thinner catalyst is preferred in the counter-flow reactor.

Reaction model – As discussed previously, residence time plays a more important role in determining conversion than global equivalence ratio in counter-flow reactors. This effect is through variation of the local equivalence ratio at a given location in the catalyst and heat transfer from hot areas of the catalyst to cooler sections. Single species fuel and mixture fuel share some similarity of the model in this reactor. For pure ethanol cases, at the catalyst top surface, local equivalence ratio is close to but slightly richer than the global equivalence ratio; at the bottom surface, local equivalence ratio is always lean of stoichiometric for every experimental condition. (Fig. 7.10) This indicates that the fuel could diffuse to the bottom surface of the catalyst and an axial equivalence ratio distribution was established. As illustrated in the model shown in Fig. 7.9, this distribution is rich to lean from the top to the bottom surface; an axial location with unity equivalence ratio exists in between. In the lean region, the catalytic partial oxidation dominates. Most heat supporting the autothermal reaction is produced in this region and transferred to the top part of the catalyst. Above the stoichiometry surface, steam reforming dominates. In this region, most of the syngas is produced by CPOx and steam reforming where the steam supply is from the fuel in the case of hydrous ethanol or from oxidation in the lower portion of the reactor. Furthermore, some ethanol droplets reflect away from the catalyst top surface (Fig. 7.19), directly decreasing the conversion. This effect explains the high amount unburned ethanol measured in all cases. In the 150-proof ethanol case, the evaporation of the fuel becomes more complicated, due to the latent heat of water (2257 J/g) is much large than ethanol (841 J/g). The ethanol portion of the fuel droplet

evaporates first and goes through surface phase reaction while the water portion continues to move towards the catalyst lower surface for steam reforming. Therefore, there are two stoichiometric planes in such case and the heat generation from the top plane is not enough to maintain the full steaming reforming happening on the lower plane. Without CPOx, ethanol only reacts by Al_2O_3 on the lower plane, generating a large volume of ethylene that cokes the catalyst.

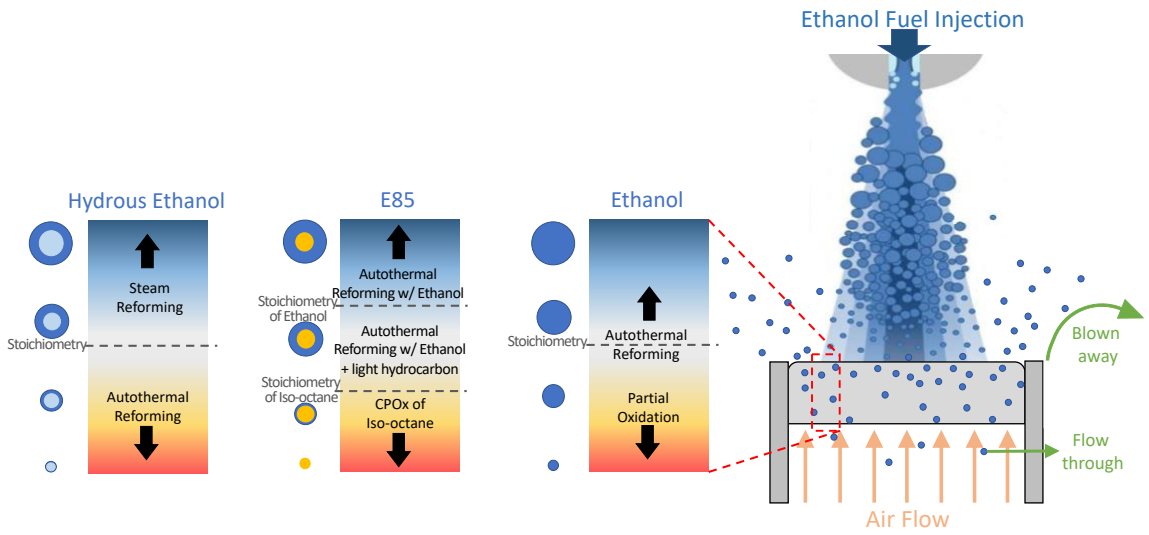

Figure 7.9 Predicted reaction model for non-premixed reactive volatilization reactor

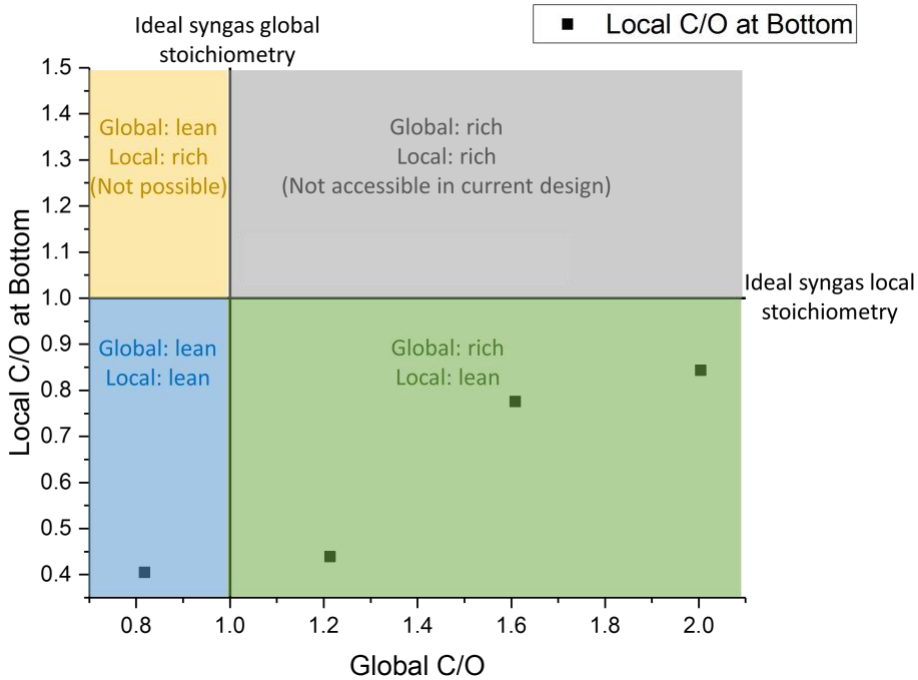

Figure 7.10 Local C/O ratio at bottom of catalyst Vs. Global C/O ratio

Reforming Efficiency

For reforming efficiency (Fig. 7.11), the increasing conversion leads to decreasing reforming efficiency. The calculation for the reforming efficiency includes the ethanol and iso-octane. All calculations are based on the lower heating value. The higher conversion of the fuel, the more heat wasted in the reaction. E85 has a higher reforming efficiency for all C/O ratios. At C/O =0.68 the reforming efficiency is 96.68%. This is because of the minimal reaction in this condition, that only a very small amount of fuel converts to CO_2 and water. Despite this, E85 still has a higher reforming efficiency than the other fuels. The reason could be that the leftover iso-octane might be overestimated by the carbon balance since other unmeasured carbon species are also counted as

iso-octane. However, due to the high carbon number of iso-octane, such approximation is acceptable. The reforming efficiency of hydrous ethanol is between E85 and pure ethanol since the steam reforming shifts the optimal reaction zone to a higher C/O ratio that out of tested range. The pure ethanol has a relative low reforming efficiency because some ethanol converted to CO_2 and water in generation heat to maintain the reaction. The pure ethanol reforming efficiency is between 60%-70%. This makes the pure ethanol an inefficient fuel for on-board reforming application with this reactor, since too much heating value of the fuel is lost that decrease the overall efficiency. However, the E85 had a higher reforming efficiency and could have more practical applicability.

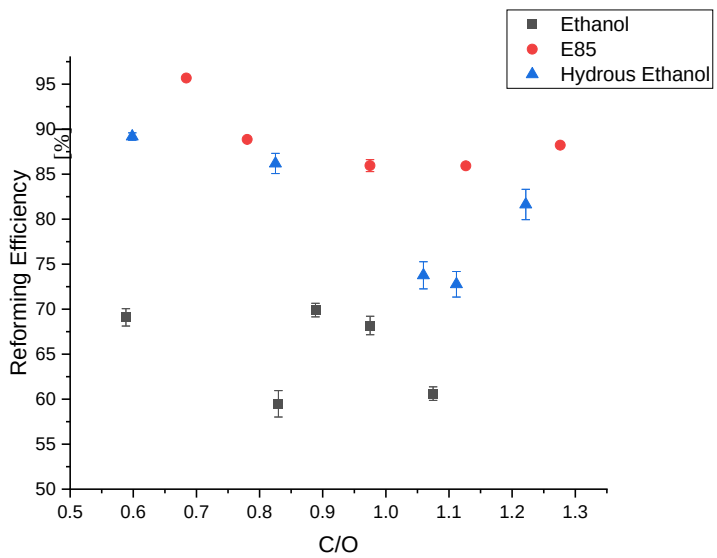

Figure 7.11 Reforming efficiency for different C/O ratio

7.3 Conclusions

In this section a counter-flow reactor specially designed for liquid fuels reforming was presented. This reactor is derived from the gaseous counter-flow reactor in Chapter 4 but has an

atomizer like the intake manifold injector of a spark ignition engine. In this chapter, we studied the effects of spray pressure, reaction C/O ratio, and fuel type to the reforming outcome. E85, pure ethanol and hydrous ethanol were selected as the example fuels.

Specifically, a higher spray pressure will generate smaller fuel droplets that have a shorter residence time on the catalyst by flowing faster. A higher pressure resulted in higher and more stable conversion. In the case of C/O ratio, an optimum condition could be identified for the maximum outcome. In our study it was about C/O=1.1 and the reforming performance would decrease when C/O increase further. Fuel type also plays an important role in reforming performance. E85 gave very similar reforming outcome as pure ethanol but had a slightly higher light hydrocarbon from the iso-octane content, while ethanol generated more syngas. Hydrous ethanol was quite different from them by the huge latent heat intake during water phase change. The case of hydrous ethanol was so complicated that it was not solely a counter-flow condition but inclined to steam reforming. When considering soot/coke formation, pure ethanol had the lowest soot generation, E85 had slightly more soot than pure ethanol, while hydrous ethanol generated some soot/coke that deactivated the catalyst since it no longer followed the counter-flow condition.

Chapter 8 Suggested Future Work

This work has demonstrated that the non-premixed counter-flow reactor has unique benefits derived from decoupling the flow of the fuel and the oxidizer. This additional degree of freedom facilitates the application of our counter-flow reactor in fundamental studies of a variety of fields. In addition, in our study, we have proven the counter-flow reactor is only marginally impacted by gas phase reactions and is dominated by surface chemistry. Based on these findings of this study, the counter-flow reactor is recommended for following future research.

Reaction Rate Study by the Counter-flow Reactor

Our reactor has the potential to be used in global reaction rate studies. The reaction rate of a catalytic surface reaction could be expressed by the Arrhenius equation (Eq. 8.1) and a log form (Eq. 8.2). The reaction rate is a function of (1/T); the slope is a function of the activation energy; and the interception is ln of pre-exponential factor. In our reactor, the reaction rate could be calculated with the heat release at the catalytic mesh. For an exothermic reaction, the catalytic surface release heat to the flow that establishes a unique temperature profile along the reaction zone. The same temperature profile could also be achieved by an electric heating mesh without reaction at the same location as the catalytic mesh when setting the flow conditions the same as reaction cases. By adjusting the current and voltage, the power of the electric heater matches the heat

generation of the surface reaction. Herein, we have the heat generation of a series of temperature that could determine the global reaction rate.

$$k = Ae^{-\frac{E_a}{RT}} \tag{8.1}$$

$$\ln k = \ln A + \frac{-E_a}{RT} = \left(\frac{-E_a}{R}\right)\left(\frac{1}{T}\right) + \ln A \tag{8.2}$$

Additionally, the open design of the reactor gives optical access for laser measurement. Such instantaneous and noninvasive method could provide a more accurate measurement for all concentrations. For example, the Raman laser system could directly measure the reaction zone instead of the used with a sampling system in the downstream. The PLIF could measure the radicals in the reaction zone. With this setup, the elementary reaction for the surface reaction could be study.

A limitation of this study is the water vapor could not be measured with the current configuration. In the experiment, product concentrations were measured on a dry based. This is because of the Raman laser gas analysis system is separated from the reactor. All samples were measured after going through a quench sampling tube. The quench tube could quickly cool down the sample taken during the experiment, which efficiently prevents the gas phase reaction during the sampling process. However, the water vapor in the sample condensed through the quench tube resulting a loss in the speciation measurement.

Surface Reaction Extinction Limit and Estimation of Surface Reaction Rate

As discussed earlier, the counter-flow reactor has a unique velocity profile in the reaction zone. In the earlier study, the catalytic mesh effective region is limited. The mesh blows-off at some locations in the reaction zone. The counter-flow reactor could be used to study the blow-off mechanism with a simple modification. The flow outlet could be replaced by a smaller diameter one for a wider region for the velocity.

In flame studies, the flame blow-off mechanism is either due to the thermal quenching or chemical limitations. By changing the flow rate and mesh location, it is very easy to maintain the local equivalence ratio and change the local velocity. Along with the increasing flow velocity, the surface reaction will approach to the chemical limitation. So that the chemical limitation extinction limited could be measured. Furthermore, observed in the experiment, the for a local equivalence ratio the higher velocity and lower velocity gives different reaction rate. (higher/lower heat release) So that based on the first Damkhler number is defined as Eq. 8.3.

$$D_I = \frac{\text{the characteristic aerodynamic time } t_a}{\text{the characteristic chemical time } t_c} \qquad 8.3$$

The overall reaction rate is a function of the characteristic chemical time τ_c. If a critical D_I value exists for the surface reaction extinction of a certain flow condition. The aerodynamic time τ_a at this extinction limit can be used to estimate the overall reaction rate. Then a reaction rate distribution curve in the reactor is generated that could be further used for studying the interaction between surface reaction and gas phase reaction, such as absorption and desorption rate between

the surface site to the gas phase or the secondary gas phase reaction after the radical leaved the surface site. This mechanism is important for the surface reaction that both gas phase and surface phase reaction are important for the reaction. For example, in the oxidative coupling of methane reaction (OCM), methane generates CH_3 first by the surface reaction and the interested species such as C_2H_6 and C_2H_4 are generate by the recombination in the gas phase reaction.

Bibliography

[1] M.V. Twigg, Catalyst handbook, CRC1989.
[2] J.N. Armor, The multiple roles for catalysis in the production of H-2, Appl Catal a-Gen 176 (1999) 159-176.
[3] K. Aasberg-Petersen, J.H.B. Hansen, T.S. Christensen, I. Dybkjaer, P.S. Christensen, C.S. Nielsen, S.E.L.W. Madsen, J.R. Rostrup-Nielsen, Technologies for large-scale gas conversion, Appl Catal a-Gen 221 (2001) 379-387.
[4] R.C. Samsun, D. Krekel, J. Pasel, M. Prawitz, R. Peters, D. Stolten, A diesel fuel processor for fuel-cell-based auxiliary power unit applications, J Power Sources 355 (2017) 44-52.
[5] A.S. Patil, T.G. Dubois, N. Sifer, E. Bostic, K. Gardner, M. Quah, C. Bolton, Portable fuel cell systems for America's army: technology transition to the field, J Power Sources 136 (2004) 220-225.
[6] X.L. Ma, L. Sun, C.S. Song, A new approach to deep desulfurization of gasoline, diesel fuel and jet fuel by selective adsorption for ultra-clean fuels and for fuel cell applications, Catal Today 77 (2002) 107-116.
[7] B. Lindstrom, J.A.J. Karlsson, P. Ekdunge, L. De Verdier, B. Haggendal, J. Dawody, M. Nilsson, L.J. Pettersson, Diesel fuel reformer for automotive fuel cell applications, Int J Hydrogen Energ 34 (2009) 3367-3381.
[8] I. Kang, J. Bae, Autothermal reforming study of diesel for fuel cell application, J Power Sources 159 (2006) 1283-1290.
[9] P.K. Cheekatamarla, A.M. Lane, Catalytic autothermal reforming of diesel fuel for hydrogen generation in fuel cells - I. Activity tests and sulfur poisoning, J Power Sources 152 (2005) 256-263.
[10] M. Zheng, U. Asad, R. Kumar, G.T. Reader, M.C. Mulenga, W. Bombardier, M. Wang, J. Tjong, An Investigation of EGR Treatment on the Emission and Operating Characteristics of Modern Diesel Engines, Report No. 0148-7191, SAE Technical Paper, 2007.
[11] J. Hwang, X. Li, W. Northrop, Exploration of Dual Fuel Diesel Engine Operation with On-Board Fuel Reforming, Report No. 0148-7191, SAE Technical Paper, 2017.
[12] S.R. Gomes, N. Bion, G. Blanchard, S. Rousseau, V. Belliere-Baca, V. Harle, D. Duprez, F. Epron, Thermodynamic and experimental studies of catalytic reforming of exhaust gas recirculation in gasoline engines, Appl Catal B-Environ 102 (2011) 44-53.
[13] D. Fennell, J.M. Herreros, A. Tsolakis, H. Xu, K. Cockle, P. Millington, GDI engine performance and emissions with reformed exhaust gas recirculation (REGR), Report No. 0148-7191, SAE Technical Paper, 2013.

[14] D. Fennell, J. Herreros, A. Tsolakis, Improving gasoline direct injection (GDI) engine efficiency and emissions with hydrogen from exhaust gas fuel reforming, Int J Hydrogen Energ 39 (2014) 5153-5162.
[15] K. Aasberg-Petersen, J.-H.B. Hansen, T. Christensen, I. Dybkjaer, P.S. Christensen, C.S. Nielsen, S.W. Madsen, J. Rostrup-Nielsen, Technologies for large-scale gas conversion, Applied Catalysis A: General 221 (2001) 379-387.
[16] J.A. Moulijn, A. Van Diepen, F. Kapteijn, Catalyst deactivation: is it predictable?: What to do?, Applied Catalysis A: General 212 (2001) 3-16.
[17] S.M. de Lima, A.M. da Silva, L.O. da Costa, J.M. Assaf, G. Jacobs, B.H. Davis, L.V. Mattos, F.B. Noronha, Evaluation of the performance of Ni/La2O3 catalyst prepared from LaNiO3 perovskite-type oxides for the production of hydrogen through steam reforming and oxidative steam reforming of ethanol, Applied Catalysis A: General 377 (2010) 181-190.
[18] J. De Deken, P. Menon, G. Froment, G. Haemers, On the nature of carbon in Niα-Al2O3 catalyst deactivated by the methane-steam reforming reaction, Journal of Catalysis 70 (1981) 225-229.
[19] W. Durrer, J. Craig Jr, J. Lozano, Surface carbon and its effects on hydrogen adsorption on Rh (100), Applied surface science 45 (1990) 275-277.
[20] Y. Chang, J.P. Szybist, J.A. Pihl, D.W. Brookshear, Catalytic EGR-Loop Reforming for High Efficiency in a Stoichiometric SI Engine through TCR and Dilution Limit Extension. 1. Catalyst Performance and Fuel Effects, Energy & Fuels, (2017).
[21] D.W. Brookshear, J.A. Pihl, J.P. Szybist, Catalytic Steam and Partial Oxidation Reforming of Liquid Fuels for Application in Improving the Efficiency of Internal Combustion Engines, Energy & Fuels, (2017).
[22] A. Abu-Jrai, J. Rodriguez-Fernandez, A. Tsolakis, A. Megaritis, K. Theinnoi, R.F. Cracknell, R.H. Clark, Performance, combustion and emissions of a diesel engine operated with reformed EGR. Comparison of diesel and GTL fuelling, Fuel 88 (2009) 1031-1041.
[23] R. Horn, K. Williams, N. Degenstein, A. Bitsch-Larsen, D. Dalle Nogare, S. Tupy, L. Schmidt, Methane catalytic partial oxidation on autothermal Rh and Pt foam catalysts: oxidation and reforming zones, transport effects, and approach to thermodynamic equilibrium, Journal of Catalysis 249 (2007) 380-393.
[24] D. Dalle Nogare, N. Degenstein, R. Horn, P. Canu, L. Schmidt, Modeling spatially resolved profiles of methane partial oxidation on a Rh foam catalyst with detailed chemistry, Journal of Catalysis 258 (2008) 131-142.
[25] J.J. Krummenacher, K.N. West, L.D. Schmidt, Catalytic partial oxidation of higher hydrocarbons at millisecond contact times: decane, hexadecane, and diesel fuel, Journal of Catalysis 215 (2003) 332-343.

[26] J.R. Rostrup-Nielsen, New aspects of syngas production and use, Catal Today 63 (2000) 159-164.
[27] G. Panuccio, B. Dreyer, L. Schmidt, A comparison of the catalytic partial oxidation of C1 to C16 normal paraffins, AIChE journal 53 (2007) 187-195.
[28] G.J. Panuccio, B.J. Dreyer, L.D. Schmidt, A comparison of the catalytic partial oxidation of C1 to C16 normal paraffins, AIChE journal 53 (2007) 187-195.
[29] D.M. Valiev, M. Zhu, G. Bansal, H. Kolla, C.K. Law, J.H. Chen, Pulsating instability of externally forced premixed counterflow flame, Combustion and Flame 160 (2013) 285-294.
[30] E.L. Belmont, S.M. Solomon, J.L. Ellzey, Syngas production from heptane in a non-catalytic counter-flow reactor, Combustion and Flame 159 (2012) 3624-3631.
[31] Y. Ghermay, J. Mantzaras, R. Bombach, K. Boulouchos, Homogeneous combustion of fuel-lean H2/O2/N2 mixtures over platinum at elevated pressures and preheats, Combustion and Flame 158 (2011) 1491-1506.
[32] X. Zheng, J. Mantzaras, R. Bombach, Kinetic interactions between hydrogen and carbon monoxide oxidation over platinum, Combustion and Flame 161 (2014) 332-346.
[33] M. Reinke, J. Mantzaras, R. Bombach, S. Schenker, N. Tylli, K. Boulouchos, Effects of H2O and CO2 dilution on the catalytic and gas-phase combustion of methane over platinum at elevated pressures, Combustion science and technology 179 (2007) 553-600.
[34] V.M. Janardhanan, S. Appari, S. Jayanti, O. Deutschmann, Numerical study of on-board fuel reforming in a catalytic plate reactor for solid-oxide fuel cells, Chemical engineering science 66 (2011) 490-498.
[35] J.R. Salge, B.J. Dreyer, P.J. Dauenhauer, L.D. Schmidt, Renewable hydrogen from nonvolatile fuels by reactive flash volatilization, Science 314 (2006) 801-804.
[36] J.L. Colby, P.J. Dauenhauer, L.D. Schmidt, Millisecond autothermal steam reforming of cellulose for synthetic biofuels by reactive flash volatilization, Green Chemistry 10 (2008) 773-783.
[37] T. Aicher, L. Griesser, Novel process to evaporate liquid fuels and its application to the catalytic partial oxidation of diesel, J Power Sources 165 (2007) 210-216.
[38] R. Szolak, E.A.M. Wiemer, I. Kraljevic, A. Susdorf, H. Karadeniz, B. Epple, F. Rümmele, A. Schaadt, On-Board Fuel Tailoring with a Novel Catalytic Evaporator for HCCI Combustion, Report No. 0148-7191, SAE Technical Paper, 2016.
[39] J. Hong, P. Kirchen, A.F. Ghoniem, Numerical simulation of ion transport membrane reactors: oxygen permeation and transport and fuel conversion, Journal of membrane science 407 (2012) 71-85.
[40] N.E. McGuire, N.P. Sullivan, O. Deutschmann, H. Zhu, R.J. Kee, Dry reforming of methane in a stagnation-flow reactor using Rh supported on strontium-substituted hexaaluminate, Applied Catalysis A: General 394 (2011) 257-265.

[41] N.E. McGuire, N.P. Sullivan, R.J. Kee, H. Zhu, J.A. Nabity, J.R. Engel, D.T. Wickham, M.J. Kaufman, Catalytic steam reforming of methane using Rh supported on Sr-substituted hexaaluminate, Chemical Engineering Science 64 (2009) 5231-5239.
[42] A.E. Potter, J.N. Butler, A novel combustion measurement based on the extinguishment of diffusion flames, 1959, pp. 54-56.
[43] Y. Otsuka, T. Niioka, On the deviation of the flame from the stagnation point in opposed-jet diffusion flames, Combustion and Flame 19 (1972) 171-179.
[44] H. Tsuji, Counterflow diffusion flames, Progress in energy and combustion science 8 (1982) 93-119.
[45] M.J. Manton, On the extinction of diffusion flames, International Journal of Engineering Science 12 (1974) 507-518.
[46] R. Friedman, J.B. Levy, Inhibition of opposed jet methane-air diffusion flames. The effects of alkali metal vapours and organic halides, Combustion and Flame 7 (1963) 195-201.
[47] T.A. Milne, C.L. Green, D.K. Benson, The use of the counterflow diffusion flame in studies of inhibition effectiveness of gaseous and powdered agents, Combustion and Flame 15 (1970) 255-263.
[48] M.M. Ibiricu, A.G. Gaydon, Spectroscopic studies of the effect of inhibitors on counterflow diffusion flames, Combustion and Flame 8 (1964) 51-62.
[49] R.A. Dodding, R.F. Simmons, A. Stephens, The extinction of methane-air diffusion flames by sodium bicarbonate powders, Combustion and Flame 15 (1970) 313-315.
[50] S. Deng, P. Zhao, D. Zhu, C.K. Law, NTC-affected ignition and low-temperature flames in nonpremixed DME/air counterflow, Combustion and Flame 161 (2014) 1993-1997.
[51] W. Sun, M. Uddi, S.H. Won, T. Ombrello, C. Carter, Y. Ju, Kinetic effects of non-equilibrium plasma-assisted methane oxidation on diffusion flame extinction limits, Combustion and Flame 159 (2012) 221-229.
[52] C.B. Reuter, S.H. Won, Y. Ju, Experimental study of the dynamics and structure of self-sustaining premixed cool flames using a counterflow burner, Combustion and Flame 166 (2016) 125-132.
[53] J.K. Lefkowitz, J.S. Heyne, S.H. Won, S. Dooley, H.H. Kim, F.M. Haas, S. Jahangirian, F.L. Dryer, Y. Ju, A chemical kinetic study of tertiary-butanol in a flow reactor and a counterflow diffusion flame, combustion and flame 159 (2012) 968-978.
[54] Y. Wang, A. Raj, S.H. Chung, Soot modeling of counterflow diffusion flames of ethylene-based binary mixture fuels, Combustion and Flame 162 (2015) 586-596.
[55] Y. Wang, S.H. Chung, Strain rate effect on sooting characteristics in laminar counterflow diffusion flames, Combustion and Flame 165 (2016) 433-444.

[56] S.K. Choi, E.-S. Cho, S.H. Chung, Quantification of extinction mechanism in counterflow premixed flames, Journal of mechanical science and technology 28 (2014) 3863-3871.
[57] A.N. Fatsikostas, D.I. Kondarides, X.E. Verykios, Steam reforming of biomass-derived ethanol for the production of hydrogen for fuel cell applications, Chem Commun, (2001) 851-852.
[58] V. Fierro, V. Klouz, O. Akdim, C. Mirodatos, Oxidative reforming of biomass derived ethanol for hydrogen production in fuel cell applications, Catal Today 75 (2002) 141-144.
[59] M.A. Goula, S.K. Kontou, P.E. Tsiakaras, Hydrogen production by ethanol steam reforming over a commercial Pd/γ-Al2O3 catalyst, Applied Catalysis B: Environmental 49 (2004) 135-144.
[60] M. Dömök, M. Tóth, J. Raskó, A. Erdőhelyi, Adsorption and reactions of ethanol and ethanol–water mixture on alumina-supported Pt catalysts, Applied Catalysis B: Environmental 69 (2007) 262-272.
[61] L.V. Mattos, G. Jacobs, B.H. Davis, F.B. Noronha, Production of hydrogen from ethanol: review of reaction mechanism and catalyst deactivation, Chemical reviews 112 (2012) 4094-4123.
[62] A.M. Karim, Y. Su, J. Sun, C. Yang, J.J. Strohm, D.L. King, Y. Wang, A comparative study between Co and Rh for steam reforming of ethanol, Applied Catalysis B: Environmental 96 (2010) 441-448.
[63] H.-S. Roh, A. Platon, Y. Wang, D.L. King, Catalyst deactivation and regeneration in low temperature ethanol steam reforming with Rh/CeO 2–ZrO 2 catalysts, Catalysis letters 110 (2006) 1-6.
[64] E.B. Pereira, N. Homs, S. Martí, J. Fierro, P.R. de la Piscina, Oxidative steam-reforming of ethanol over Co/SiO2, Co–Rh/SiO2 and Co–Ru/SiO2 catalysts: Catalytic behavior and deactivation/regeneration processes, Journal of catalysis 257 (2008) 206-214.
[65] D. Li, I. Atake, T. Shishido, Y. Oumi, T. Sano, K. Takehira, Self-regenerative activity of Ni/Mg (Al) O catalysts with trace Ru during daily start-up and shut-down operation of CH4 steam reforming, Journal of Catalysis 250 (2007) 299-312.
[66] M. Ashrafi, C. Pfeifer, T. Pröll, H. Hofbauer, Experimental study of model biogas catalytic steam reforming: 2. Impact of sulfur on the deactivation and regeneration of Ni-based catalysts, Energy & fuels 22 (2008) 4190-4195.
[67] M. Virginie, M. Araque, A.-C. Roger, J.C. Vargas, A. Kiennemann, Comparative study of H2 production by ethanol steam reforming on Ce2Zr1. 5Co0. 5O8− δ and Ce2Zr1. 5Co0. 47Rh0. 07O8− δ: evidence of the Rh role on the deactivation process, Catal Today 138 (2008) 21-27.

[68] A.N. Fatsikostas, D.I. Kondarides, X.E. Verykios, Production of hydrogen for fuel cells by reformation of biomass-derived ethanol, Catal Today 75 (2002) 145-155.
[69] S.M. de Lima, A.M. da Silva, L.O. da Costa, U.M. Graham, G. Jacobs, B.H. Davis, L.V. Mattos, F.B. Noronha, Study of catalyst deactivation and reaction mechanism of steam reforming, partial oxidation, and oxidative steam reforming of ethanol over Co/CeO2 catalyst, Journal of Catalysis 268 (2009) 268-281.
[70] L. Costa, A. Silva, L. Borges, L. Mattos, F. Noronha, Partial oxidation of ethanol over Pd/CeO2 and Pd/Y2O3 catalysts, Catal Today 138 (2008) 147-151.
[71] A.M. Silva, A.M.D. De Farias, L.O. Costa, A.P. Barandas, L.V. Mattos, M.A. Fraga, F.B. Noronha, Partial oxidation and water–gas shift reaction in an integrated system for hydrogen production from ethanol, Applied Catalysis A: General 334 (2008) 179-186.
[72] L.V. Mattos, F.B. Noronha, The influence of the nature of the metal on the performance of cerium oxide supported catalysts in the partial oxidation of ethanol, J Power Sources 152 (2005) 50-59.
[73] L. Mattos, F. Noronha, Hydrogen production for fuel cell applications by ethanol partial oxidation on Pt/CeO2 catalysts: the effect of the reaction conditions and reaction mechanism, Journal of Catalysis 233 (2005) 453-463.
[74] G. Deluga, J. Salge, L. Schmidt, X. Verykios, Renewable hydrogen from ethanol by autothermal reforming, Science 303 (2004) 993-997.
[75] W. Fang, J. Fang, D.B. Kittelson, W.F. Northrop, An experimental investigation of reactivity-controlled compression ignition combustion in a single-cylinder diesel engine using hydrous ethanol, Journal of Energy Resources Technology 137 (2015).
[76] V. Klouz, V. Fierro, P. Denton, H. Katz, J. Lisse, S. Bouvot-Mauduit, C. Mirodatos, Ethanol reforming for hydrogen production in a hybrid electric vehicle: process optimisation, J Power Sources 105 (2002) 26-34.
[77] M. Ni, D.Y. Leung, M.K. Leung, A review on reforming bio-ethanol for hydrogen production, Int J Hydrogen Energ 32 (2007) 3238-3247.
[78] T. Hou, S. Zhang, Y. Chen, D. Wang, W. Cai, Hydrogen production from ethanol reforming: catalysts and reaction mechanism, Renewable and Sustainable Energy Reviews 44 (2015) 132-148.
[79] A.C. Basagiannis, P. Panagiotopoulou, X.E. Verykios, Low temperature steam reforming of ethanol over supported noble metal catalysts, Topics in catalysis 51 (2008) 2-12.
[80] F. Aupretre, C. Descorme, D. Duprez, Bio-ethanol catalytic steam reforming over supported metal catalysts, Catalysis Communications 3 (2002) 263-267.
[81] A. Erdőhelyi, J. Raskó, T. Kecskés, M. Tóth, M. Dömök, K. Baán, Hydrogen formation in ethanol reforming on supported noble metal catalysts, Catal Today 116 (2006) 367-376.

[82] A. Yee, S. Morrison, H. Idriss, The reactions of ethanol over M/CeO2 catalysts: Evidence of carbon–carbon bond dissociation at low temperatures over Rh/CeO2, Catal Today 63 (2000) 327-335.
[83] W. Tang, Z. Hu, M. Wang, G.D. Stucky, H. Metiu, E.W. McFarland, Methane complete and partial oxidation catalyzed by Pt-doped CeO2, Journal of Catalysis 273 (2010) 125-137.
[84] J. Bronsted, Acid and Basic Catalysis, Chemical Reviews 5 (1928) 231-338.
[85] A. Ehn, J. Zhu, X. Li, J. Kiefer, Advanced laser-based techniques for gas-phase diagnostics in combustion and aerospace engineering, Applied spectroscopy 71 (2017) 341-366.
[86] C. Kaminski, J. Hult, M. Aldén, High repetition rate planar laser induced fluorescence of OH in a turbulent non-premixed flame, Applied Physics B: Lasers and Optics 68 (1999) 757-760.
[87] Z. Li, J. Kiefer, J. Zetterberg, M. Linvin, A. Leipertz, X.-S. Bai, M. Aldén, Development of improved PLIF CH detection using an Alexandrite laser for single-shot investigation of turbulent and lean flames, Proceedings of the Combustion Institute 31 (2007) 727-735.
[88] B. Zhou, J. Kiefer, J. Zetterberg, Z. Li, M. Aldén, Strategy for PLIF single-shot HCO imaging in turbulent methane/air flames, Combustion and Flame 161 (2014) 1566-1574.
[89] J.B. Michael, P. Venkateswaran, J.D. Miller, M.N. Slipchenko, J.R. Gord, S. Roy, T.R. Meyer, 100 kHz thousand-frame burst-mode planar imaging in turbulent flames, Optics letters 39 (2014) 739-742.
[90] B. Zhou, C. Brackmann, Z. Li, M. Aldén, Development and application of CN PLIF for single-shot imaging in turbulent flames, Combustion and Flame 162 (2015) 368-374.
[91] T. Lee, J.B. Jeffries, R.K. Hanson, Experimental evaluation of strategies for quantitative laser-induced-fluorescence imaging of nitric oxide in high-pressure flames (1–60 bar), Proceedings of the Combustion Institute 31 (2007) 757-764.
[92] W.D. Kulatilaka, B.D. Patterson, J.H. Frank, T.B. Settersten, Comparison of nanosecond and picosecond excitation for interference-free two-photon laser-induced fluorescence detection of atomic hydrogen in flames, Applied optics 47 (2008) 4672-4683.
[93] J.H. Frank, X. Chen, B.D. Patterson, T.B. Settersten, Comparison of nanosecond and picosecond excitation for two-photon laser-induced fluorescence imaging of atomic oxygen in flames, Applied optics 43 (2004) 2588-2597.
[94] O. Lammel, M. Stöhr, P. Kutne, C. Dem, W. Meier, M. Aigner, Experimental analysis of confined jet flames by laser measurement techniques, Journal of Engineering for Gas Turbines and Power 134 (2012) 041506.

[95] M. Linne, P. Petersson, J. Olofsson, C. Brachman, H. Seyfried, J. Zetterberg, M. Richter, M. Alden, R. Cheng, Simultaneous PIV/OH-PLIF Rayleigh thermometry/OHPLIF and stereo PIV measurements in a low-swirl flame, Sandia National Laboratories (SNL-CA), Livermore, CA (United States), 2007.
[96] W. Meier, I. Boxx, M. Stöhr, C. Carter, Laser-based investigations in gas turbine model combustors, Experiments in fluids 49 (2010) 865-882.
[97] A. Lantz, R. Collin, M. Aldén, A. Lindholm, J. Larfeldt, D. Lörstad, Investigation of hydrogen enriched natural gas flames in a SGT-700/800 burner using OH PLIF and chemiluminescence imaging, Journal of Engineering for Gas Turbines and Power 137 (2015) 031505.
[98] R. Reisenhofer, J. Kiefer, E.J. King, Shearlet-based detection of flame fronts, Experiments in Fluids 57 (2016) 41.
[99] C. Carter, J. Donbar, J. Driscoll, Simultaneous CH planar laser-induced fluorescence and particle imaging velocimetry in turbulent nonpremixed flames, Applied Physics B: Lasers and Optics 66 (1998) 129-132.
[100] C.D. Carter, S. Hammack, T. Lee, High-speed flamefront imaging in premixed turbulent flames using planar laser-induced fluorescence of the CH C− X band, Combustion and Flame 168 (2016) 66-74.
[101] J. Kiefer, Z. Li, T. Seeger, A. Leipertz, M. Aldén, Planar laser-induced fluorescence of HCO for instantaneous flame front imaging in hydrocarbon flames, Proceedings of the Combustion Institute 32 (2009) 921-928.
[102] J.D. Miller, S.R. Engel, J.W. Tröger, T.R. Meyer, T. Seeger, A. Leipertz, Characterization of a CH planar laser-induced fluorescence imaging system using a kHz-rate multimode-pumped optical parametric oscillator, Applied optics 51 (2012) 2589-2600.
[103] J.D. Miller, S.R. Engel, T.R. Meyer, T. Seeger, A. Leipertz, High-speed CH planar laser-induced fluorescence imaging using a multimode-pumped optical parametric oscillator, Optics letters 36 (2011) 3927-3929.
[104] E. Friesen, C. Gessenhardt, S.A. Kaiser, T. Dreier, C. Schulz, In-cylinder temperature measurements via time-correlated single-photon counting of toluene laser-induced fluorescence through a fiber-based sensor, Optics letters 37 (2012) 5244-5246.
[105] A. Ehn, M. Jonsson, O. Johansson, M. Aldén, J. Bood, Quantitative oxygen concentration imaging in toluene atmospheres using Dual Imaging with Modeling Evaluation, Experiments in fluids 54 (2013) 1433.
[106] S. Faust, T. Dreier, C. Schulz, Temperature and bath gas composition dependence of effective fluorescence lifetimes of toluene excited at 266 nm, Chemical Physics 383 (2011) 6-11.

[107] J. Yoo, D. Mitchell, D. Davidson, R. Hanson, Planar laser-induced fluorescence imaging in shock tube flows, Experiments in fluids 49 (2010) 751-759.
[108] J. Yoo, D. Mitchell, D. Davidson, R. Hanson, Near-wall imaging using toluene-based planar laser-induced fluorescence in shock tube flow, Shock Waves 21 (2011) 523.
[109] V.A. Miller, M. Gamba, M.G. Mungal, R.K. Hanson, Single-and dual-band collection toluene PLIF thermometry in supersonic flows, Experiments in fluids 54 (2013) 1539.
[110] V.A. Miller, M. Gamba, M.G. Mungal, R.K. Hanson, Single- and dual-band collection toluene PLIF thermometry in supersonic flows, Experiments in Fluids 54 (2013).
[111] J.J. Conti, P.D. Holtberg, J. Beamon, A.M. Schaal, J. Ayoub, J.T. Turnure, Annual energy outlook 2014, US Energy Information Administration, (2014) 1-269.
[112] R. Ma, B. Xu, X. Zhang, Catalytic partial oxidation (CPOX) of natural gas and renewable hydrocarbons/oxygenated hydrocarbons-A review, Catal Today, (2019).
[113] P. Rahnama, A. Paykani, R.D. Reitz, A numerical study of the effects of using hydrogen, reformer gas and nitrogen on combustion, emissions and load limits of a heavy duty natural gas/diesel RCCI engine, Applied energy 193 (2017) 182-198.
[114] P. Rahnama, A. Paykani, V. Bordbar, R.D. Reitz, A numerical study of the effects of reformer gas composition on the combustion and emission characteristics of a natural gas/diesel RCCI engine enriched with reformer gas, Fuel 209 (2017) 742-753.
[115]
J.T. Hwang, W.F. Northrop. Gas and Particle Emissions From a Diesel Engine Operating in a Dual-Fuel Mode Using High Water Content Hydrous Ethanol. In: editor^editors. ASME 2014 Internal Combustion Engine Division Fall Technical Conference; 2014: American Society of Mechanical Engineers Digital Collection. p.
[116] L. Zhu, Z. He, Z. Xu, X. Lu, J. Fang, W. Zhang, Z. Huang, In-cylinder thermochemical fuel reforming (TFR) in a spark-ignition natural gas engine, Proceedings of the Combustion Institute 36 (2017) 3487-3497.
[117] W. Fang, D.B. Kittelson, W.F. Northrop, Optimization of reactivity-controlled compression ignition combustion fueled with diesel and hydrous ethanol using response surface methodology, Fuel 160 (2015) 446-457.
[118]
W. Fang, D.B. Kittelson, W.F. Northrop, J. Fang. An experimental investigation of reactivity-controlled compression ignition combustion in a single-cylinder diesel engine using hydrous ethanol. In: editor^editors. ASME 2013 Internal Combustion Engine Division Fall Technical Conference; 2013: American Society of Mechanical Engineers Digital Collection. p.

[119] S.L. Kokjohn, R.M. Hanson, D. Splitter, R. Reitz, Fuel reactivity controlled compression ignition (RCCI): a pathway to controlled high-efficiency clean combustion, International Journal of Engine Research 12 (2011) 209-226.
[120] A.J. Nord, J.T. Hwang, W.F. Northrop, Emissions From a Diesel Engine Operating in a Dual-Fuel Mode Using Port-Fuel Injection of Heated Hydrous Ethanol, Journal of Energy Resources Technology 139 (2017).
[121] J.T. Hwang, A.J. Nord, W.F. Northrop, Efficacy of Add-On Hydrous Ethanol Dual Fuel Systems to Reduce NOx Emissions From Diesel Engines, Journal of Energy Resources Technology 139 (2017).
[122] X.L. Ying Lin, Martyn V. Twigg, William F. Northrop, Non-Premixed Reactive Volatilization Reactor for Catalytic Partial Oxidation of Low Volatility Fuels at Short Contact Time Reaction Chemistry $ Engineering, (2020).
[123] Quantel, TDL+ INSTRUCTION MANUAL.
[124] J. Sjöholm, J. Rosell, B. Li, M. Richter, Z. Li, X.-S. Bai, M. Aldén, Simultaneous visualization of OH, CH, CH 2 O and toluene PLIF in a methane jet flame with varying degrees of turbulence, Proceedings of the Combustion Institute 34 (2013) 1475-1482.
[125] S. Kaiser, M. Schild, C. Schulz, Thermal stratification in an internal combustion engine due to wall heat transfer measured by laser-induced fluorescence, Proceedings of the combustion institute 34 (2013) 2911-2919.
[126] S.C. Eichmann, J. Trost, T. Seeger, L. Zigan, A. Leipertz, Application of linear Raman spectroscopy for the determination of acetone decomposition, Optics express 19 (2011) 11052-11058.
[127] R.J. Kee, M.E. Coltrin, P. Glarborg, Chemically reacting flow: theory and practice, John Wiley & Sons2005.
[128] A. Bitsch-Larsen, R. Horn, L. Schmidt, Catalytic partial oxidation of methane on rhodium and platinum: Spatial profiles at elevated pressure, Applied Catalysis A: General 348 (2008) 165-172.
[129] R. Horn, K. Williams, N. Degenstein, A. Bitschlarsen, D. Dallenogare, S. Tupy, L. Schmidt, Methane catalytic partial oxidation on autothermal Rh and Pt foam catalysts: Oxidation and reforming zones, transport effects, and approach to thermodynamic equilibrium, Journal of Catalysis 249 (2007) 380-393.
[130] R. Horn, N.J. Degenstein, K.A. Williams, L.D. Schmidt, Spatial and temporal profiles in millisecond partial oxidation processes, Catalysis letters 110 (2006) 169-178.
[131] M.V.T. X. Li, and W. Northrop, Opposed-Flow Reactive Volatilization Reactor for Reforming Low Volatility Fuels 36th International Combustion Symposium, Seoul, South Korea, , (2016.).
[132] C. Robinson, D.B. Smith, The auto-ignition temperature of methane, Journal of hazardous materials 8 (1984) 199-203.

[133] D.A. Hickman, L.D. Schmidt, Synthesis gas formation by direct oxidation of methane over Pt monoliths, Journal of Catalysis 138 (1992) 267-282.
[134] C. Diehm, O. Deutschmann, Hydrogen production by catalytic partial oxidation of methane over staged Pd/Rh coated monoliths: Spatially resolved concentration and temperature profiles, Int J Hydrogen Energ 39 (2014) 17998-18004.
[135] B.S. Rj, M. Loganathan, M.S. Shantha, A review of the water gas shift reaction kinetics, International Journal of Chemical Reactor Engineering 8 (2010).
[136] Mathwork File Exchange. https://www.mathworks.com/matlabcentral/fileexchange/ (accessed 9/15/2020 2020).
[137] F. D'Almeida, Nonlinear Diffusion Toolbox. https://www.mathworks.com/matlabcentral/fileexchange/3710-nonlinear-diffusion-toolbox (accessed 9/15 2020).
[138] R. Buitrago-Sierra, J. Ruiz-Martínez, J. Serrano-Ruiz, F. Rodríguez-Reinoso, A. Sepúlveda-Escribano, Ethanol steam reforming on Ni/Al2O3 catalysts: Effect of the addition of Zn and Pt, Journal of colloid and interface science 383 (2012) 148-154.
[139] G.E. Daniels, Measurement of gas temperature and the radiation compensating thermocouple, Journal of Applied Meteorology 7 (1968) 1026-1035.
[140] V. Sobyanin, S. Cavallaro, S. Freni, Dimethyl ether steam reforming to feed molten carbonate fuel cells (MCFCs), Energy & fuels 14 (2000) 1139-1142.
[141] C. Diehm, T. Kaltschmitt, O. Deutschmann, Hydrogen production by partial oxidation of ethanol/gasoline blends over Rh/Al2O3, Catal Today 197 (2012) 90-100.
[142] C. Houtman, M. Barteau, Divergent pathways of acetaldehyde and ethanol decarbonylation on the Rh (111) surface, Journal of Catalysis 130 (1991) 528-546.
[143] J.N. Wilson, F. Zaera, Alkane Oxidation on Rh (111) Single-Crystal Surfaces under High-Temperature, Short-Contact-Time Conditions: A Molecular Beam Kinetic Study, The Journal of Physical Chemistry C 114 (2010) 16946-16954.
[144] E.C. Wanat, B. Suman, L.D. Schmidt, Partial oxidation of alcohols to produce hydrogen and chemicals in millisecond-contact time reactors, Journal of Catalysis 235 (2005) 18-27.
[145] S. Cavallaro, V. Chiodo, S. Freni, N. Mondello, F. Frusteri, Performance of Rh/Al2O3 catalyst in the steam reforming of ethanol: H2 production for MCFC, Applied Catalysis A: General 249 (2003) 119-128.